DESIGN AND FABRICATION OF TRANSPARENT ULTRASOUND TRANSDUCER FOR PHOTOACOUSTIC IMAGING APPLICATION

ZHANG JIAMING

PhD

The Hong Kong Polytechnic University

2025

The Hong Kong Polytechnic University
Department of Applied Physics

Design and Fabrication of Transparent Ultrasound Transducer for Photoacoustic Imaging Application

ZHANG Jiaming

A thesis submitted in partial fulfillment of the requirements for the degree of Doctor of Philosophy

January 2025

CERTIFICATE OF ORIGINALITY

I hereby declare that this thesis is my own work and that, to the best of my knowledge and belief, it reproduces no material previously published or written, nor material that has been accepted for the award of any other degree or diploma, except where due acknowledgement has been made in the text.

_____ (Signed)

_____ZHANG JIAMING_ (Name of Student)

Abstract

Photoacoustic imaging (PAI) plays a pivotal role within the domain of biomedical engineering, a field that integrates the high contrast and optical imaging capabilities of ultrasound imaging with its profound penetration depth. However, conventional ultrasound transducers are opaque, thereby obstructing the light pathway, so the necessity of complex light components in PAI systems to deliver light results in bulky system designs. Transparent ultrasound transducers (TUTs) are regarded as a viable solution to this challenge, enabling the transmission of light through the transducers and direct illumination of targets. This study aims to enhance the performance of single-element TUTs by investigating both transparent active and passive materials. Additionally, the TUT array is fabricated and characterized for its potential to offer a novel co-axial design for photoacoustic computed tomography (PACT).

Adoption of transparent polymethyl methacrylate (PMMA) for acoustic matching layers in high-frequency TUTs results in a significant improvement of -6 dB bandwidth (*BW*) from 20% to 50%, leading to enhanced axial resolution of PAI. The efficacy of the proposed TUT has been demonstrated through successful phantom and *in vivo* PAI with different frequencies of TUTs, indicating that the novel transparent acoustic matching method is universally applicable.

To increase sensitivity of TUTs *in vivo* ultrasound imaging, transparent piezoelectric

materials are studied to explore ultrasound/photoacoustic dual-modality imaging. Cutting-edge alternating current (AC) poling technology is studied for high-frequency (>20 MHz) TUT applications, with a focus on voltage and cycle number conditions. The [001]-oriented $Pb(Zn_{1/3}Nb_{2/3})O_3$-$PbTiO_3$ (PZN-PT) single crystal is used for TUT due to its high piezoelectric constant and great piezoelectric voltage constant, and the transducer shows insertion loss (IL) of 23.8 dB, achieving successful *in vivo* ultrasound imaging. Additionally, Eu doped PMN-PT ceramic is utilized to develop a TUT with dimensions of 2×2 mm^2 for photoacoustic microscopy. The dual-modality imaging capability of this ceramic has been demonstrated with a high signal-to-noise ratio, and its imaging depth has also been successfully demonstrated. Eu doped PMN-PT ceramic exhibits very large clamped dielectric constant, making it a promising candidate for photoacoustic endoscopy applications.

The TUT array is fabricated using a novel fabrication method. The fabrication process includes initial bonding of the flexible circuit, followed by the separate dicing of the elements based on the alignment of the flexible circuit. The 64-element array exhibits a center frequency of 17 MHz and a -6 dB bandwidth of 35%, demonstrating excellent uniformity. Additionally, the photoacoustic A-line of each element is measured, and the TUT array demonstrates considerable potential for further *in vivo* PACT applications, as evidenced by the measured high performance of each element. The findings of this study indicate a promising future for TUTs and related imaging applications.

Publication List

1. **Zhang, J.**, Bao, G., Hou, S., ... Dai, J.Y. (2024) Transparent Ultrasound Transducers: From Materials to Applications. *Advanced Devices & Instrumentation,* 6, 0083. (**Chapter 1**)

2. **Zhang, J**., Long, X., Zhang, G., Ma, Z., Li, W., Wang, Y., ... & Lam, K. H. (2023). Broadband transparent ultrasound transducer with polymethyl methacrylate as matching layer for *in vivo* photoacoustic microscopy. *Photoacoustics*, *33*, 100548. (**Chapter 2**)

3. **Zhang, J.**, Gao, W., ...& Dai, J. (2024) Transparent Ultrasound Transducer based on PZN-PT Single Crystal for Ultrasound/Photoacousitc Image. *Sensors and Actuators A: Physical,* 384, 116282. (**Chapter 3**)

4. Guo, P., Gao, W., Lin, R., Wang, X., Lan, J., **Zhang, J.**, ... & Zhang, S. (2024). Advancement in PMN-PT transparent piezoelectric ceramic for photoacoustic/ultrasound dual-mode imaging. *Journal of Materiomics*, 100932. (**Chapter 3**)

5. Gao, W., Wang, X., **Zhang, J**., Tian, X., Zheng, F., Guo, P., ... & Zhang, Y. (2024). Achieving coaxial photoacoustic/ultrasound dual-modality imaging by high-performance Sm: 0.72 PMN-0.28 PT transparent piezoelectric ceramic. *Nano Energy*, 132, 110390. (**Chapter 3**)

6. **Zhang, J.**, Gao, W., ... Dai, J.Y. (2024) High-frequency Transparent Ultrasound Transducer Array for Photoacoustic Imaging Application. *Journal of Advanced*

Dielectric (*Accepted*) (**Chapter 4)**

7. **Zhang, J. M**., Bao, G. C., Gao, W., Lin, R. Q., Yang, F., & Lam, K. H. (2024). Miniature Ultrasound Transducer Incorporating Sm-PMN-PT 1-3 Composite. *Journal of Composites Science*, 8(3), 80.

8. Wong, C. M., Chan, S. F., Liu, R., **Zhang, J**., Wu, W. C., Liang, Z., ... & Dai, J. Y. (2022). 20-MHz phased array ultrasound transducer for *in vivo* ultrasound imaging of small animals. *Ultrasonics*, *126*, 106821.

9. Lin, R., Zhang, Q., Lv, S., **Zhang, J.**, Wang, X., Shi, D., ... & Lam, K. H. (2023). Miniature intravascular photoacoustic endoscopy with coaxial excitation and detection. *Journal of Biophotonics*, *16*(4), e202200269.

10. Lin, R., **Zhang, J**., Gao, W., Wang, X., Lv, S., Lam, K. H., & Gong, X. (2023). A miniature multi-functional photoacoustic probe. *Micromachines*, 14(6), 1269.

11. Li, G., Sun, Q., Fu, Y., Hou, S., **Zhang, J**., Xu, K. L., & Dai, J. Y. (2024). A single crystal row–column-array for 3D ultrasound imaging. *Ultrasonics*, *139*, 107289.

12. **Zhang, J.**, Lin, R.. ...& Dai, J. Lithium Niobate based 1-3 Composites for High Frequency Transparent Ultrasound Transducer. *Composites Communications* (*In press*)

13. **Zhang, J.**, Zhang, M.. ...& Dai, J. Studies on Composites based Transparent Ultrasound Transducers for Photoacoustic Imaging Application. *Composites Part B: Engineering* (*In press*)

Acknowledgement

I would like to thank Prof. Dai Jiyan, my chief supervisor, for his guidance and direction. He not only teaches me how to do specific research but also makes me think critically. His patience and guidance warm me during my study period.

I am also grateful to Dr. Lam Kwok-ho for introducing me to the research field. My knowledge and skills of transducer development are broadened with the selfless help and guidance of Dr. Lam.

In addition, I would like to thank Dr. Li Changhui. Without his help, our fruitful research work might not have been completed. He also provides a new perspective for academic thinking and writing.

I also would like to thank Dr. Long Xing, Dr. Yang Fan, Dr. Lin Riqiang, Miss. Gao Wen, Miss. Bao Guocui, Mr. Hou Shilin, and Dr. Terence Wong. They helped me a lot during my study period, brainstorming ideas and practical experiments.

Especially, I would like to thank Dr. Zhang Guangjie. Her selfless love and encouragement push me help me move forward, including both research works and daily life.

Finally, I would like to express my sincere gratitude to my family for their support.

List of Figures

List of Tables

Table of Contents

1.1 Photoacoustic Imaging

Optical imaging technology has emerged as a pivotal element within the domain of biomedical imaging, owing to its ability to provide high contrast, high specificity, and the absence of radiation. However, its application is constrained by the short penetration depth, which is a consequence of significant light scattering within body tissues. Consequently, as depth increases, imaging resolution undergoes a precipitous decline, therefore, the imaging depth of pure optical imaging is currently constrained to the millimeter range [1]. Photoacoustic imaging (PAI) technology has been developed to overcome the limitations of conventional imaging methods by combining the high contrast of optical imaging with the penetrative capabilities and resolution of ultrasound imaging [2]. Furthermore, the use of scattered light in PAI is advantageous because it enables signal generation from all photons [3].

The basic principle of PAI is as follows. Pulsed laser is used to illuminate biological tissues, and after absorbing energy of laser, biological tissues are heated, leading to thermoelastic expansion of tissues and broadband ultrasound signal transmission; subsequently, the generated ultrasound signal can be acquired by ultrasound transducers. Wavelength of laser should be carefully considered for different PAI applications, as different tissues own their specific optical absorption coefficient. For instance, the blood (especially hemoglobin in red blood cells) is the main absorber for visual light and near-infrared light. Due to the high optical absorption coefficient and large weight

ratio to body, blood is one of key targets for PAI. Metabolism can be observed through PAI of concentration of oxygenated hemoglobin, which is a key clinical physiological parameter. Therefore, PAI has been widely used as a functional imaging tool for mapping of resting state brain connectivity, diagnosis of cancers and micro-vessel mapping [4-6].

1.2 Piezoelectric Ultrasound Transducer

As the key parameter of PAI system, characteristics of transducer affect imaging quality mainly. Piezoelectric ultrasound transducer is an instrumentation based on piezoelectric effect, where electrical energy and mechanical energy can be converted.

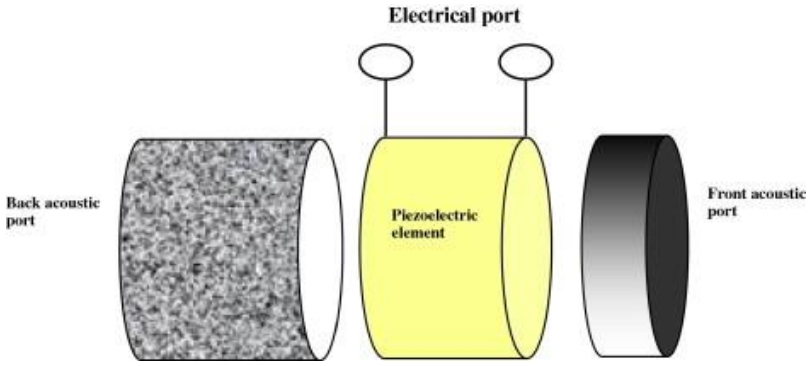

Figure 1.1. Basic structure of a ultrasound transducer [7]

In PAI, when the generated acoustic wave reaches the surface of a transducer, the electrical signal can be obtained for data acquisition. Basic structure of ultrasound transducer is shown as Fig. 1.1, which consists of piezoelectric layer, matching later and backing layer. To achieve high-quality imaging applications, transducers should have characteristics of high frequency, broad bandwidth and appropriate acoustic matching. As the pivotal active layer, the properties of piezoelectric material include piezoelectric coefficient along poling direction (d_{33}), electromechanical coupling

coefficient (k_t), and clamped dielectric constant (ε_s). The d_{33} can be defined as polarization generated per unit of mechanical stress applied to a piezoelectric material, expressed as:

$$d_{33} = \frac{Strain\ development}{Applied\ electric\ field} \tag{1}$$

As d_{33} represents the mechanical displacement performance along the direction of polarization, a high-sensitivity transducer requires the piezoelectric material with high d_{33}.

As a quantitative measurement of electrical and mechanical energy transformation efficiency ranging from 0 to 1, k_t value can be calculated as:

$$k_t = \sqrt{\frac{\pi}{2}\frac{f_r}{f_a}\tan\left(\frac{\pi}{2}\frac{f_a - f_r}{f_a}\right)} \tag{2}$$

where f_r is the resonance frequency and f_a is anti-resonance frequency of the piezoelectric material.

The clamped dielectric constant is highly related to the electrical impedance of a transducer. As the standard electrical impedance of commercial instrumentation is 50 Ω, achieving electrical matching can improve performance of transducer effectively [8]. Electrical impedance of a ultrasound transducer can be estimated as [9]:

$$Z_E = \frac{t}{2\pi f_r A \varepsilon_s \varepsilon_0} \tag{3}$$

where t and A are thickness and aperture size of piezoelectric material, respectively, and ε_0=8.854×10^{-12} F/m is dielectric constant in vacuum. To obtain ε_s of piezoelectric material, clamped series capacitance (C_s) should be measured at the specific frequency (usually two times of anti-resonant frequency), and then calculated as [10]

$$\varepsilon_s = \frac{C_s t}{A\varepsilon_0} \tag{4}$$

Except for the active layer, other passive layers also play important roles in enhancing performance of ultrasound transducers through acoustic matching. Each material owns specific acoustic impedance defined as

$$Z = \rho c \tag{5}$$

where ρ is the density and c is longitude sound velocity of the material. When an ultrasound wave transmits from one material to another, reflection and transmission happen at the boundary. The transmission coefficient (T) depends on differences between acoustic impedance of the two materials as

$$T = \frac{4Z_i Z_t}{(Z_i + Z_t)^2} \tag{6}$$

where Z_i and Z_t are acoustic impedance of incident material and transmitted material, respectively.

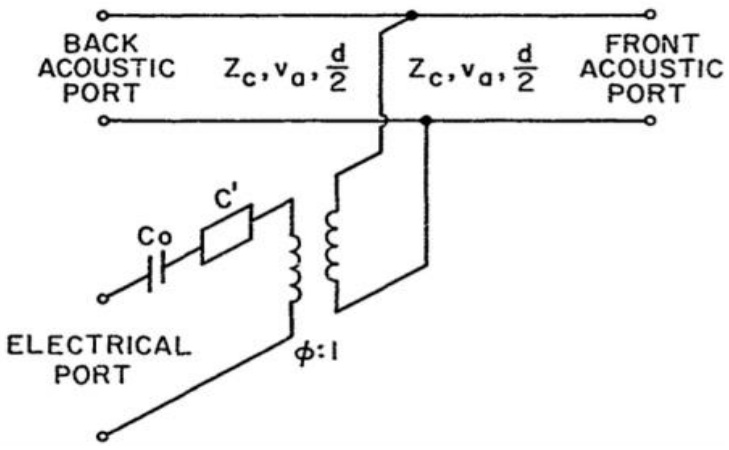

Figure 1.2. Standard KLM model for the ultrasound transducer.

In biomedical ultrasound imaging area, biological tissues are always transmitted targets with low acoustic impedance (1.5 MRayl), while most of piezoelectric materials have relatively high acoustic impedance (> 30 MRayl). Thus only < 20% ultrasound

energy can be transmitted into biological tissues. Therefore, matching layers with appropriate acoustic impedance are employed to improve ultrasound wave propagation. Based on Krimholtz, Leedom and Matthael (KLM) equivalent circuit model, desired acoustic impedance of matching layer can be estimated [11].

For single matching layer scheme, the ideal acoustic impedance of matching layer (Z_s) can be expressed

$$Z_s = Z_p^{\frac{1}{3}} Z_b^{\frac{2}{3}} \tag{7}$$

where Z_p is the acoustic impedance of the piezoelectric material, and Z_b is the acoustic impedance of biological tissues (1.5 MRayl). For the double matching layers scheme, the acoustic impedance of each matching layer is:

$$Z_1 = Z_p^{\frac{4}{7}} Z_b^{\frac{3}{7}} \tag{8}$$

$$Z_2 = Z_p^{\frac{1}{7}} Z_b^{\frac{6}{7}} \tag{9}$$

With quarter-wavelength thickness, matching layers with appropriate acoustic impedance can improve performances of ultrasound transducers.

When electrical field is applied, vibration happens, and ultrasound signals are generated at both surfaces of the piezoelectric material. Different from transmitted signal at matching layer side, the signal at the backside will have strong reflection to affect performance of transducer if there is no backing layer. The back-reflected signal superposes with the front transmitted signal and leads to a long ring-down, which extends the pulse-length of front signal and reduces the axial resolution. Thus, the backing layer is introduced to absorb the backside signal. An ideal backing layer should have high acoustic attenuation and similar acoustic impedance to piezoelectric material.

The performance of ultrasound transducer is mainly determined by its center frequency (f_c), bandwidth (BW) and sensitivity. To measure the f_c and BW, pulse-echo measurement is always conducted, during which, the transducer is connected to a pulser/receiver and immersed in distilled water. A reflector (quartz or polished stainless steel) is placed under the transducer with a certain distance. For a focused transducer, the distance should be equal to the focal length of the transducer. For unfocused transducers with a flat surface, the distance should be larger than near field distance (N) to achieve natural focus of acoustic beams. The distance can be expressed as:

$$N = \frac{kL^2 f_c}{4c} \tag{10}$$

where k is the coefficient that related to shape of transducer, and L is the length of the element aperture. The acquired signal will be further processed by fast Fourier Transform (FFT) to determine f_c and BW as:

$$f_c = \frac{f_1 + f_2}{2} \tag{11}$$

$$BW = \frac{f_2 - f_1}{f_c} \times 100\% \tag{12}$$

where f_1 and f_2 are defined as lower and upper −6 dB frequencies, respectively.

The sensitivity of ultrasound transducer is always defined as the insertion loss (IL). When electrical voltage (V_0) is applied on transducer, an echo signal can be obtained with amplitude V_r. IL can be calculated as

$$IL = 20\log\frac{V_r}{V_0} + \alpha + 2.2 \times 10^{-4} \times 2df_c^2 \tag{13}$$

where α is the energy loss by scattering at the reflector surface, 2.2×10^{-4} (dB/cm×MHz^2) is the acoustic attenuation coefficient in water, and d is the distance between the transducer and the reflector.

In biomedical imaging application, several echo signals are combined to form a B-mode image, where lateral and axial resolutions are used to describe quality of image. The axial resolution is the resolution along the wave propagation direction which can be expressed:

$$R_{axial}^{US} = 0.5\frac{c}{f_2 - f_1} \tag{14}$$

where c is sound velocity in the propagation media. The function shows that BW has an inversely proportional relationship with axial resolution. Also, based on definition of resolution, shorter echo-signal pulse length result in higher axial resolution [12]. In the photoacoustic area, similar concepts are also suitable for its axial resolution. Photoacoustic axial resolution can be express as [13]

$$R_{axial}^{PA} = 0.88\frac{c}{f_2 - f_1} \tag{15}$$

Ultrasound lateral resolution is related to the shaped of a transducer, while photoacoustic lateral resolution is mainly determined by the size of incident laser spot for the optical resolution photoacoustic microscopy [14].

1.3 Transparent Ultrasound Transducer

In photoacoustic imaging (PAI) system, the light delivery pathway and the position of the ultrasound transducer need to be carefully designed. Conventional PAI system can be divided into two different methods, including reflection mode and transmission mode.

Reflection mode PAI achieves light delivery and acoustic acquisition at one side as shown in Fig. 1.3 (a) and (b). The PAI system either employs light illumination from

sides of the transducer or uses complex optical design to co-align laser and acoustic beams, leading to bulky system designs. As the trend of miniaturization and handheld design [15, 16], such bulky system blocks development of PAM. For transmission mode, light delivery and acoustic detection are conducted at opposite sides as shown in Fig. 1.3 (c). However, this configuration is not well-suited for practical biomedical imaging applications, as biological tissues typically possess significant thickness.

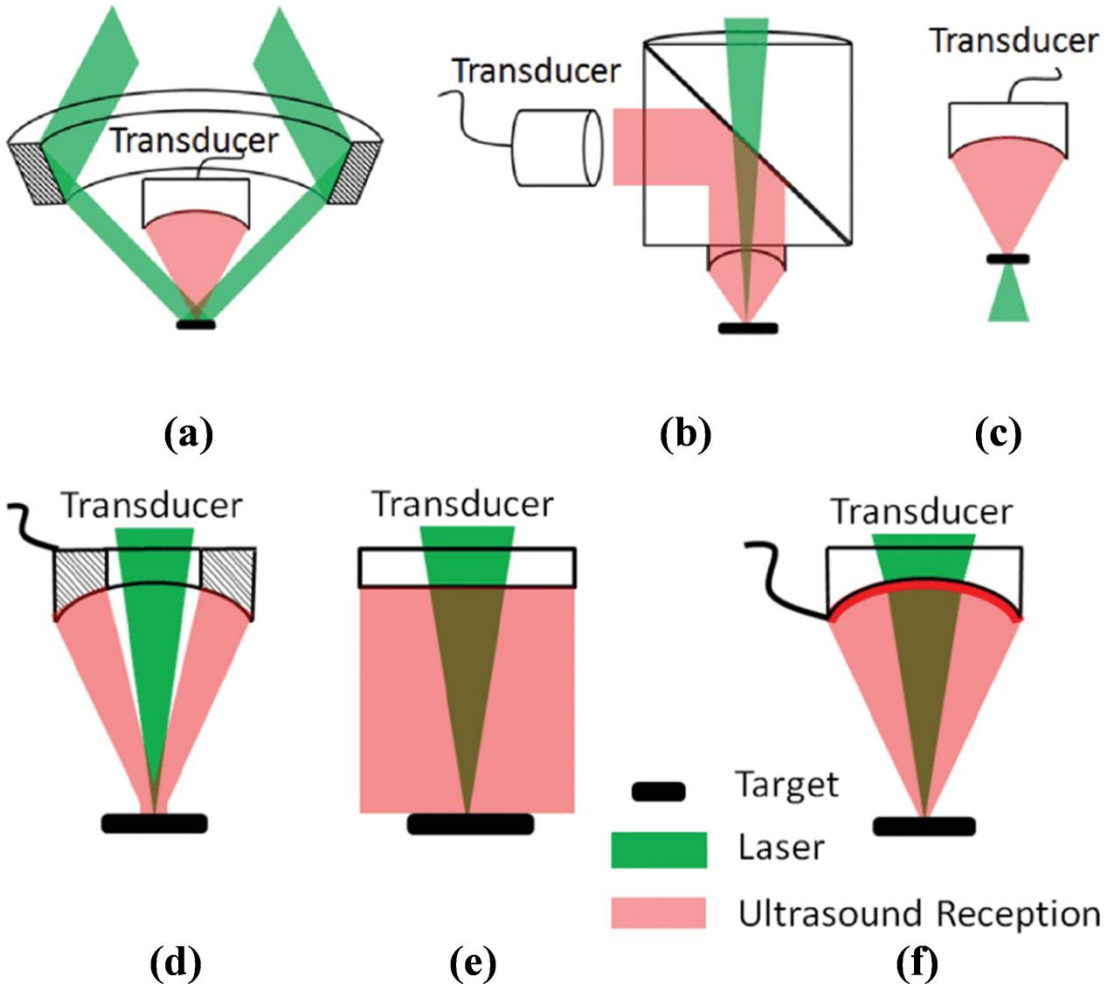

Figure 1.3. **(a)** PAI system with additional optical mirrors, **(b)** PAI system with optical-acoustic combiner; **(c)** PAI system with transmission mode setup. **(d)** PAI system with a hollow structure transducer;PAI system with **(e)** a planar TUT and **(f)** focused TUT [17].

Conventional ultrasound transducers usually consist of Cr/Au electrode and mixture of epoxy with metal/oxide powders as passive layers, which are opaque and

may block the light path. To partially resolve the issue, a ring-shaped or hollow ultrasound transducer is proposed to allow the laser beam to pass through as shown in Fig. 1.3(d). However, the central orifice in the transducer may lead to the adverse effect on electrical properties and acoustic energy [18], and degradation of image quality [19]. Additionally, signals arriving at the place of central orifice may not be acquired, leading to further degraded imaging quality.

Allowing light transmission through the sensor directly may be an alternative way to co-align light and acoustic beam. This approach may achieve a simple system design and more effective signal acquisition (Fig. 1.3(e) and (f)). Transparent pure-optical ultrasound detection sensors, such as Fabry-Pérot sensor, have been investigated a lot in recent years [20, 21]. Although these sensors possess advantages including broadband and sensitive detection, it is still challenging to make a parallel array; this substantially limits their implementation. Moreover, it is difficult to integrate these kinds of sensors into ultrasound/photoacoustic dual-modality imaging system. In this circumstance, transparent transducers were raised which can be divided into three categories: transparent capacitive micromachined ultrasound transducer (CMUT) [22, 23], transparent piezoelectric micromachined ultrasound transducers (PMUT) [24, 25], and piezoelectric transparent ultrasound transducers (TUTs). Among these transducers, TUT can not only be operated at high frequencies (> 20MHz) without any additional components, but also be manufactured at low cost.

1.3.1 Lithium Niobate (LN)-based TUT

The y-cut 36° LN has been studied a lot for transducer applications due to its high electromechanical coupling coefficient, low dielectric loss and dielectric constant. With transparent nature, LN was widely studied for development of TUTs. Dangi *et a*l demonstrated the LN-based TUTs with 14.5 MHz center frequency for photoacoustic endoscopy (PAE) and microscopy (PAM) applications [26]. The transparent indium tin oxide (ITO) electrodes were sputter deposited to supersede conventional Cr/Au electrodes, while transparent epoxy was used as backing layer; this process results in transparency over 80%. Although the bandwidth was limited (< 30%) due to the lack of matching layers, photoacoustic A-line and phantom images were successfully achieved. Further investigation was conducted to apply this type of TUT for *ex vivo* optical resolution PAM, where imaging capability of biological tissues was demonstrated (Fig. 1.4 (a)) [27]. Dual-function TUT device was also investigated with a GRIN lens bonded at the backside of LN for laser coupling (Fig. 1.4 (b)). The compact design achieved PAI with 40 MHz center frequency and photoacoustic flow cytometry [28]. To enhance acoustic signal transmission efficiency, vapor-deposited Parylene C was added in the front layer of TUT as single matching layer. With improved sensitivity and bandwidth (~36%), the TUT could be employed for awake mouse braining PAI. In addition, the TUT may replace the glass window during imaging [29]. Chen *et a*l proposed a high-frequency TUT with similar structure [30] reaching 36.9 MHz center frequency and slightly improved bandwidth (~35%). With an additional layer, the transparency was not degraded. The high frequency was desired for *in vivo* PAI due to

better axial resolution. Similarly, transparent epoxy, which possesses higher acoustic impedance compared to Parylene C, was also considered as a matching layer material to further improve performance of TUT. Liao *et al* developed a large-aperture TUT with epoxy matching layer [31], where the large aperture provides relatively large field of view (FOV), so that laser scanning method may be applied to improve the imaging speed (100 Hz over 1mm). With clearly imaged microvascular network of mouse ear and abdomen, the ability of TUT for fast imaging and large organs imaging were demonstrated. Except for working as a matching layer, the transparent epoxy can also be filled as acoustic lens due to its low viscosity. A lens-focused TUT was developed for acoustic resolution PAM application [32], and the sensitivity of this TUT was increased with two-way insertion loss as high as 17.12 dB at its f_c. With this TUT, simultaneous ultrasound/PAI was then achieved for mouse *in vivo* (Fig. 1.4 (c)).

However, the acoustic impedance of transparent polymer matching layer is still relatively low; this cannot solve the acoustic mismatch problem between LN and biological tissue effectively. As a common transparent material with high acoustic impedance, glass (> 12 MRayl) was considered as the first matching layer for double matching layer scheme, and as reported, the *BW* of the transducer has been increased to over 60% [33]. Except for glass, Parylene C was also deposited as the second matching layer (Figs. 1.4. (d) and (e)). However, the broad *BW* may be led by an additional low frequency waveform, which was introduced by mass-load effect. Two measured center frequencies were reported as 7.2 MHz and 11.8 MHz, while corresponding bandwidths were 36.1% and 62.7%, respectively. Similar phenomenon

was also observed by Park *et al* [34]. In their work, an acoustic lens was lapped down to a desired thickness and bonded as the first matching layer with Parylene C as the second matching layer; this design of transducer results in 7.5 MHz and 31.5 MHz center frequencies with 175% and 25.4% bandwidths, respectively. The measured axial resolution of ultrasound imaging and PAI with this transducer were 890 μm and 91 μm, respectively. Although performances of the TUT were limited, quadruple biomedical imaging system, including ultrasound, PAI, optical coherence and fluorescence, were successfully developed based on TUT. This study verified the ability of TUT implementing with other biomedical optical imaging, where *in vivo* imaging without label was demonstrated. Another study utilizing similar TUT structure with higher frequency was reported with glass acoustic lens and Parylene C for matching layer [35]; the f_c of this TUT was measured as 36.9 MHz with 18.3% bandwidth. With this TUT, a high-speed optical resolution PAM system was established and verified by *in vivo* imaging. To further improve the performance of TUTs, Park *et a*l tried to modify the thickness of the second matching layer, achieving *BW* ~50% without the dual-frequency phenomenon [36, 37].

Moreover, novel transparent composite materials were investigated for proper acoustic matching. Glass beads/epoxy composites with different weight fraction were studied [38]. The acoustic impedance of composites may achieve an ideal value; however, the increased fraction of glass bead may lead to light scattering, which is not desired for PAM. Only 15% glass beads can be applied for practical PAI application with limited bandwidth. Researchers then found that mico-SiO_2/epoxy composites

achieved both high transparency and proper acoustic impedance [39]. Based on SiO_2 bead of 3 μm partial size and epoxy with low viscosity, matching and backing layers were developed to make a TUT whose performance was comparable to conventional opaque transducers (Fig. 1.4 (f)). The ultrasensitive TUT results in high-quality ultrasound/photoacoustic imaging for both *in vivo* animals and human. In addition, the transparent ultrasound array was studied (Fig. 1.4 (g)), for large field of view and high imaging speed [40].

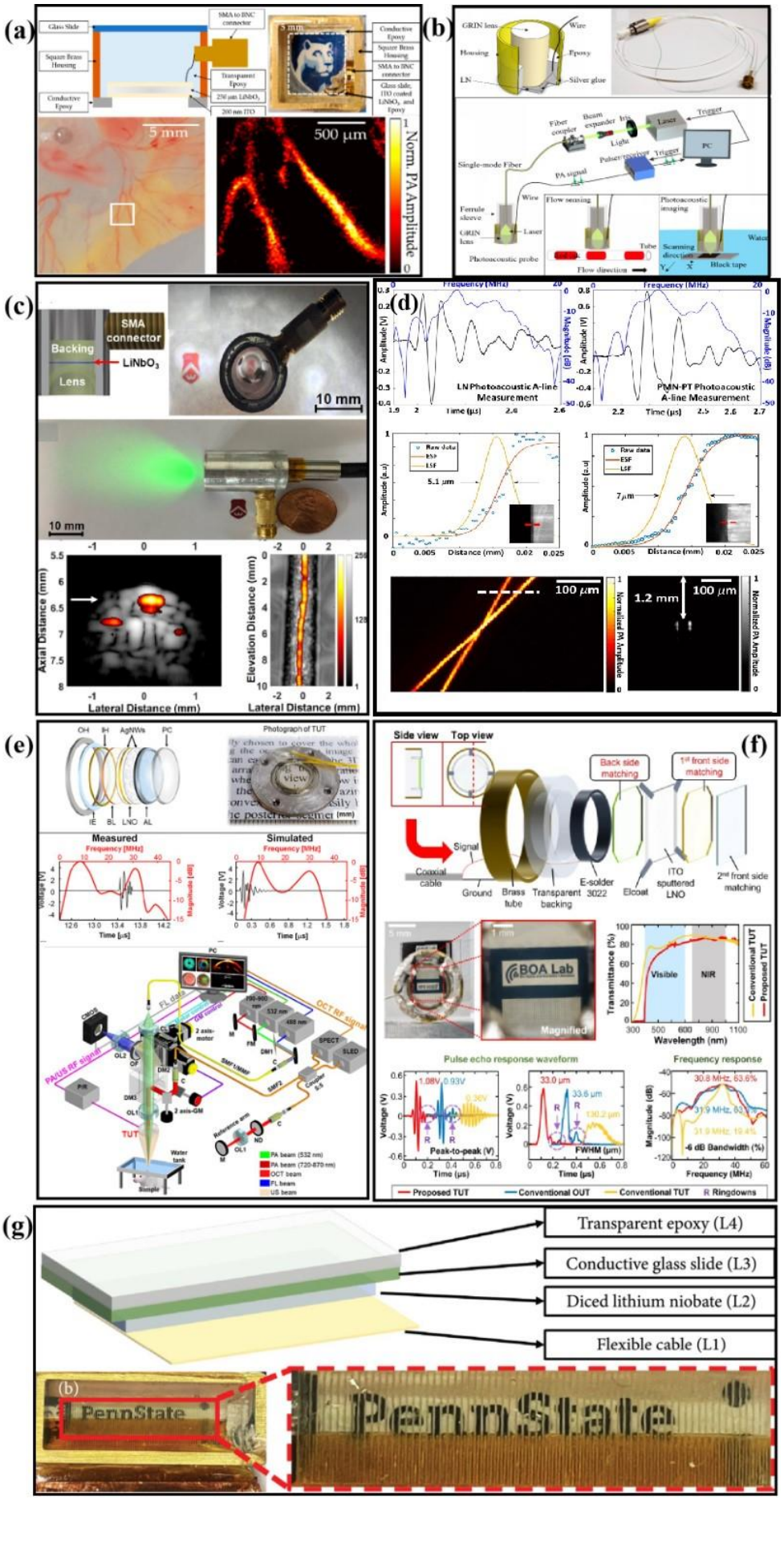
(a)
(b)
(c)
(d)
(e)
(f)
(g)
Backing
SMA connector
Lens
LiNbO3
10 mm
Axial Distance (mm)
Lateral Distance (mm)
Elevation Distance (mm)
LN Photoacoustic A-line Measurement
PMN-PT Photoacoustic A-line Measurement
Measured
Simulated
Side view
Top view
Back side matching
1st front side matching
2nd front side matching
Coaxial cable
Ground
Brass tube
Transparent backing
E-solder 3022
Elcoat
ITO sputtered LNO
Signal
BOA Lab
Magnified
Visible
NIR
Conventional TUT
Proposed TUT
Wavelength (nm)
Transmittance (%)
Pulse echo response waveform
Frequency response
Peak-to-peak (V)
FWHM (μm)
-6 dB Bandwidth (%)
Proposed TUT
Conventional OUT
Conventional TUT
R Ringdowns
Transparent epoxy (L4)
Conductive glass slide (L3)
Diced lithium niobate (L2)
Flexible cable (L1)
PennState

Figure 1.4. (a) Schematic and photograph of the TUT; photograph and PAI of chick-embryo chorioallantois membrane (CAM) [27]. **(b)** Schematic and photograph of developed TUT probe; schematics of system and experimental setup [28]. **(c)** Schematic and photograph of developed TUT and light propagation through the TUT; *in vivo* photoacoustic/ultrasound imaging [32]. **(d)** Photograph of developed TUT; measured phantom PAI imaging [33]. **(e)** Schematic and photograph of developed TUT; schematic diagram of developed quadruple imaging system based on TUT [34]. **(f)** Schematic and photograph of developed TUT; comparison of the TUT with conventional transducer [39]. (**g**) Schematic of the proposed TUT array [40].

1.3.2 Relaxor ferroelectric single crystal-based TUT

With the development of TUTs, investigations on matching and backing layers have gained much progress. To further enhance performance of TUT, attentions on transparent piezoelectric layer should be paid. With careful lapping and polishing, <001> direction lead magnesium niobate-lead titanate (PMN-PT) with conventional DC poling method was studied for a handheld photoacoustic finder, where glass acoustic lens and Parylene C were employed for acoustic matching (Figs. 1.5 (a) and (b)). The TUT achieved transparency over 70% at specific wavelength (Fig. 1.5 (c)) [41]. The TUT possessed 8 MHz f_c and 45% *BW* with pure and clear frequency spectra (Fig. 1.5(d)). Moreover, a high-frequency TUT based on PMN-PT with optimized-thickness double matching layer was developed for endoscopy application. The bandwidth could reach 50%, while high-quality ultrasound/photoacoustic imaging was successfully demonstrated for rectum and vagina of the rat *in vivo* [42]. To further enhance the PMN-PT single crystal based TUT, the carefully designed transparent matching layer was employed [39]. The endoscopy was demonstrated for high-quality photoacoustic/ultrasound in live pigs [43]

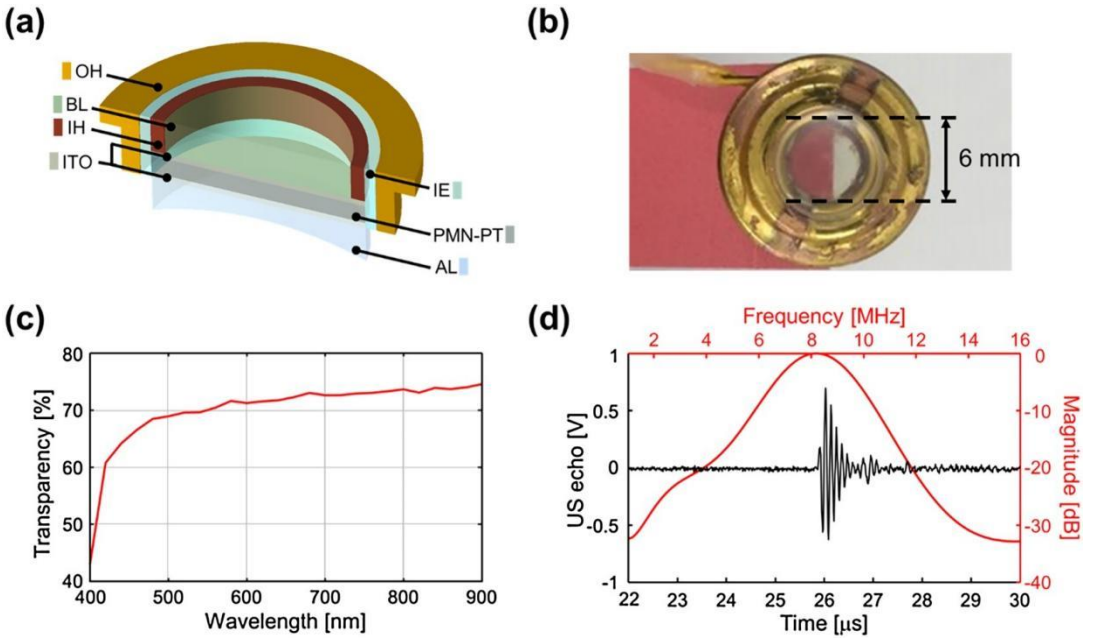

Figure 1.5. (a) Schematic of proposed TUT and **(b)** photograph of the TUT. **(c)** Measured transparency of the TUT. **(d)** Measured pulse-echo response and frequency spectrum of the TUT [41].

With further investigation, researchers found that AC electric field can improve transparency and piezoelectricity simultaneously. With conventional DC electric field poling, the 109° domain wall and the 71° domain wall were observed. For AC poling, the domain size becomes larger, and during the process, 71° domain walls are removed by AC electric field; while by contrast to the 71° domain walls, the density of 109° walls remain unchanged. Because of the elimination of 71° walls, the AC poling process makes crystals more transparent and 30% enhancement of piezoelectricity [44]. A study was conducted to show the advantages of AC-poled PMN-PT compared to LN [33], where the AC-poled PMN-PT-based TUT was demonstrated to have both higher sensitivity and axial resolution compared LN based TUT. Similar work was conducted using AC-poled PIN-PMN-PT single crystal for TUT application [45]. The fabricated TUT shows significantly high receiving sensitivity, which was desired for PAI application.

1.3.3 Ceramic based TUT

As a common piezoelectric material, ceramics play important roles in transducer fabrication. Conventional piezoelectric ceramics, such as PZT, were always opaque due to their polycrystalline nature. Recently developed rare-earth element doped lead titanate (PT)-based ceramics not only show comparable piezoelectric properties to single crystal [46], but also result in decreased domain size from micrometers to nanometers due to the doping; this gives rise to potentials of transparency [47]. In aspect of micro-structure, potential symmetric structure also enables PT-based ceramics to be transparent [48]. However, the grain boundaries and residual pores block the transparency of ceramics. Hot-press sintering method is an effective and unique way to solve the problem [49]. For instance, Eu doped PMN-PT ceramic was sintered under 100 MPa pressure and 1200 °C to achieve nearly 70% light transmittance, while d_{33} and dielectric constant were 1400 pC/N and 13300, respectively [50]. The transparent ceramics with both high d_{33} and dielectric constant possess great potential for miniaturize TUT application, such as endoscopy and intravascular PAI. Similar phenomenon was also investigated for lead-free ceramics; for example, $K_xNa_{1-x}NbO_3$ (KNN) ceramics have achieved satisfied transparency (74%) with La doping [51]. .

Researchers also investigated TUT fabricated by advanced 3D printing method with Er doped $Li_{0.04}[(K_{0.49}Na_{0.51})_{0.96}]NbO_3$ (KNNLN) ceramic powder. Through stereolithography technique, the transparent piezoelectric stack was printed, and then transparent epoxy was cast as the matching layer. The such made TUT presents 10.5

MHz center frequency and 18% bandwidth, and the photoacoustic signal can be successfully detected [52].

1.3.4 Polymer based TUT

Compared to single crystals and ceramics, piezoelectric polymers possess relatively lower acoustic impedance (< 4MRayl) for better acoustic matching, which was desired for TUT due to limited transparent matching layer materials. Polyvinylidene fluoride (PVDF) was a common piezoelectric polymer with transparent nature and good flexibility and has been widely accepted as an acoustic receiver due to its high receiving ability. With sputtered ITO electrode, PVDF was employed to fabricate a focused TUT with ~60% optical transmittance for PAM application. The PVDF film was compressed and stretched onto a convex glass lens of the TUT for focusing and backing layer as well. Over 100% bandwidth was obtained for the 24 MHz TUT without any matching layer, and the axial resolution could be improved to 14.81 μm [17]. Further optimization of TUT was conducted for higher numerical aperture and higher center frequency to improve imaging qualities [53]. Ultrasound/photoacoustic imaging was achieved for a mouse tail to evaluate performance of the compact TUT. Ultraviolet-transparent TUT was also demonstrated for resolving densely distributed cell nuclei that are indistinguishable otherwise (Fig.1.6 (a)). Compared to conventional opaque transducer based ultraviolet PAM system, TUT provides better lateral solution [54].

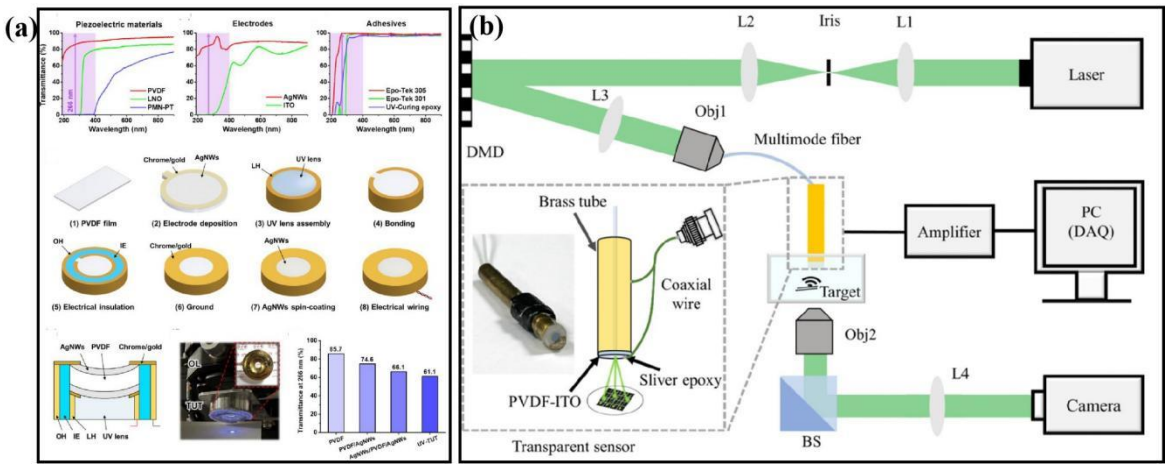

Figure 1.6. (a) Properties of the developed TUT; schematic and photograph of the TUT [54] . **(b)** Schematic of the imaging system; schematic and photograph of the developed endoscopy based on TUT [55].

Integrated with a pre-amplifier, an ultrasensitive PVDF-based TUT was developed for PAI detection [56]. The receiving sensitivity of the TUT shows significant advantage compared to a commercial hydrophone. Application on photoacoustic endoscopy of PVDF-based TUT was also investigated (Fig. 1.6(b)). It shows that, with a small aperture size, PAI signal can be acquired and phantom imaging has been demonstrated with wave front shaping functions [55, 57]. Due to the relatively lower dielectric constant of PVDF, researchers have tried to develop TUT with large aperture size for optimized electrical matching. A 6.7 MHz TUT has been successfully fabricated with 20x20 mm^2 FOV, and a 3D phantom was imaged to evaluate its capability for PAI [58]. Except for PVDF, the co-polymer piezoelectric poly(vinylidene fluorideco-trifluoroethylene) [P(VDF-TrFE)] material, possessing better piezoelectric properties compared with PVDF, was also implemented in TUT fabrication [59]. One can see that the P(VDF-TrFE)-based TUT presented higher transparency and much better sensitivity compared to PVDF-based TUT with similar transducer structure. The transparent array was also investigated with a fiber array bundled [60]. The 4.3 MHz

array was designed as the concave structure for focused light illumination and acoustic detection. Phantom PAI evaluated the performance of the compact and miniaturized array design and great imaging depth.

1.4 Research Objective

TUTs help to minimize conventional PAI system as additional room for light path is not required. However, there is no effective transparent acoustic matching method, resulting in limited sensitivity and *BW* of TUTs. While double matching schemes have been examined, they may be only suitable for specific frequencies. Moreover, certain methods are intricate and challenging to implement. Consequently, there is a clear need to study the development of an effective and simple acoustic matching technology.

Also, studies on transparent piezoelectric materials for TUTs could also help to improve performance. The research gap between advanced piezoelectric material, such as the AC-poled single crystal, and high-performance TUT needs to be bridged. In addition, it is necessary to investigate different transparent piezoelectric materials as the active layer for TUTs, offering some specific advantages.

Except for single element TUTs, TUT arrays have the potential to enhance imaging speed and expand the FOV. Additionally, the utilization of arrays enables the acquisition of 2D imaging without the necessity of scanning. These properties render

TUTs array particularly well-suited for wearable and compact PAI applications. It is expected that the applications of TUTs will bring significant improvements to all aspects of biomedical imaging area.

1.5 Overview

The thesis is comprised of five chapters. Chapter 1 introduces fundamental knowledge and related research background. A review of extant research is conducted, highlighting the research gaps that have yet to be addressed.

Chapter 2 presents research on transparent matching layers. Based on the bonding fabrication method, the thickness of the transparent matching layer is carefully studied to improve BW of TUTs. Imaging performance is conducted to evaluate the effectiveness of the broad BW.

Chapter 3 studies different piezoelectric materials for TUT applications, including AC-poled PMN-PT single crystal, conventional DC-poled relaxor-ferroelectric PZN-PT single crystal, and transparent PMN-PT ceramics with large dielectric property. Performance of each TUT is studied, mainly for the dual-modality ultrasound/PAI application.

Chapter 4 investigates the design and fabrication of the high-frequency TUT array. With a novel fabrication method, the high-frequency TUT array is proposed. Elements

performances are evaluated, including measured pulse-echo response, impedance spectra and PAI signal A-lines. The results indicate the potential of the TUT array for PACT application.

Finally, conclusions and future plans are outlined in Chapter 6.

Chapter 2. Investigation on Transparent Matching Layer

Transparent matching layer with proper design is emerging to enhance performance of TUTs. As a common transparent polymer material, polymethyl methacrylate (PMMA) owns relatively high acoustic impedance (3.2 MRayl) and low density [61, 62], which is close to the desired value of the LN-based TUT with a single matching layer and may alleviate the mass-load effect. Therefore, we investigate PMMA as the matching layer for the TUT in this study. As a thick layer attached to the transducer surface may lead to the dual-frequency phenomenon [63, 64], the study on the thickness of PMMA is very critical. In addition, PAI of both phantom and *in vivo* animal model was conducted to evaluate the performance of LN-based TUT with the PMMA matching layer.

2.1. Transducer Design and Fabrication

Table 2.1. Properties of active and passive materials.

	Sound velocity (m/s)	Density (kg/m^3)	Acoustic impedance (MRayl)
LN	7340	4600	34.0
Epotek-301	2650	1132	3.0
PMMA	2750	1175	3.2

The fabrication process was conducted as follows:

1. A double-side polished 36° rotated Y-cut LN was purchased from Shanghai Institute of Optics and Fine Mechanics. Transparent epoxy (Epotek 301, Epoxy Technology Inc., USA) was used as a backing layer as well as the bonding agent. The acoustic properties of transparent PMMA layer were measured, including longitudinal sound velocity, density, and acoustic impedance. All material parameters are listed in Table 2.1.

2. ITO was sputtered by an ITO target (In_2O_3/SnO_2 90/10 wt%, Kurt J. Lesker Company, USA) on one side of LN. The optimized sputtering conditions, as determined through rigorous experiments, include a DC power of 45 watts, accompanied by an Ar gas flow of 30 sccm for a duration of 80 minutes based on Explorer 14 system (Explorer 14, Denton Vacuum, USA). The thickness of the ITO electrode is approximately 280 nm, exhibiting a sheet resistance of ~40 Ω/sq.

3. The LN wafer was then diced into the desired size with square shape. The LN wafer was then attached to a glass substrate by the double-side tape with the electrode side up, and a 10 mm-diameter brass housing was placed surrounding the LN wafer. The ITO electrode and the brass housing were then connected using a co-axial cable, which was affixed with a conductive silver epoxy. (E-Solder 3022, Von Roll Isola Inc., USA).

4. After curing at 60 ˚C for 3 hours, the degassed transparent epoxy was filled into the brass housing as the backing layer. The degassing process needs to be carefully controlled to avoid any violent reactions. The transducer was removed from the glass substrate after curing at 65 ˚C for 2 hours.

5. The aforementioned sputtering process was conducted to sputter the transparent ITO

electrode on the front surface of transducer for ground connection.

6. The PMMA layer was lapped and polished to the desired thickness and then bonded to the transducer surface using the degassed transparent epoxy. External pressure was applied to make the bonding layer thin and uniform.

Figs. 2.1(a) and (b) show the photograph and the cross-sectional schematic view of the proposed TUT. A 20-MHz TUT was fabricated using a 150 μm-thick LN with an aperture size of 9×9 mm^2. To study the acoustic matching effect on the TUT performance, the PMMA layers with different thicknesses, including 34 μm (= $\lambda/4$), 24 μm and 17 μm, were attached as the matching layer of TUT. The optimized matching layer design was also applied on a 30-MHz TUT to further verify the validity of the proposed scheme.

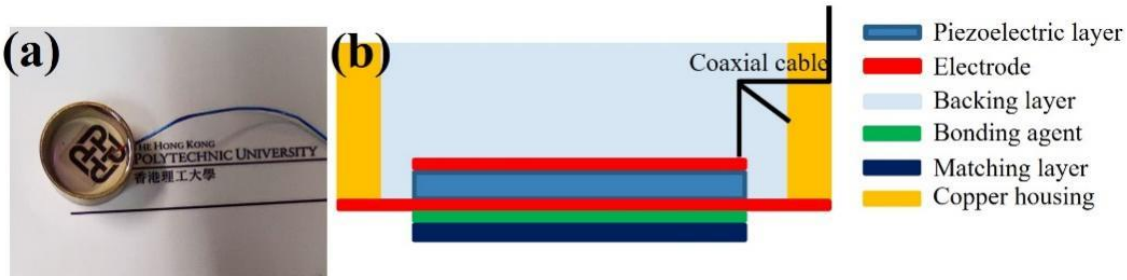

Figure 2.1. (a) Photograph and **(b)** cross-sectional schematic view of the prototype of TUT.

To measure the pulse-echo response, the fabricated TUT was mounted on a holder and immersed in distilled water. The TUT was excited by a pulser-receiver (DPR500, JSR Ultrasonics, USA) with an energy of 12.4 μJ and a pulse repetition frequency of 200 Hz. Echo signal was acquired by a data acquisition (DAQ) card and analysed by FFT to determine the f_c and BW. The TUT was then connected to an impedance analyzer (Agilent 4294A, Agilent Technologies, USA) for electrical impedance analysis, where

f_r and f_a were obtained. The effective electromechanical coupling coefficient (k_{eff}) was calculated as:

$$k_{eff} = \sqrt{1 - \frac{f_r^2}{f_a^2}} \tag{16}$$

The optical transmission efficiency of TUT was measured by a spectrometer (USB4000, Ocean optics Inc.). The transmission efficiency was obtained by calculating the ratio of light intensity before and after passing through the TUT.

2.2 PAI System

To demonstrate the PAI application of the 20-MHz TUT with the optimized PMMA matching layer, a refection-mode PAM system was customized for evaluating the performance of TUT via imaging both phantoms and *in vivo* rodents. The PAM system is shown in Fig. 2.2, which employed a pulsed laser (AO-S-532, Changchun New Industries Optoelectronics Technology Co., Ltd.; 532 nm wavelength; 4 ns pulse duration) to excite PA signal. A beam sampler (glass slide) was used to reflect small part of the laser beam to a photodiode (DET10A/M, Thorlabs Inc.) to synchronize the signal acquisition. The laser beam passed through a beam expander system consisting of two convex lenses before focusing by a convex lens with a focal length of 30 mm. The focused beam passed through the TUT and then emitted onto the target sample. The two-axis motor stage (MS-2000, Applied Scientific Instrumentation) was used to scan the sample along the *x*-y plane. The acquired PA signal was amplified by a home-made low-noise pre-amplifier (Gain: 40dB, Bandwidth: 35MHz, Noise level: 5nV/Hz$^{1/2}$), which was directly connected to the TUT without using any external cable

and recorded by a DAQ card with a sampling rate of 200 MHz (CompuScope 14200, Gage, Canada, 14 bit). The gap between the TUT and imaging sample was filled by a drop of distilled water as an ultrasound coupling medium.

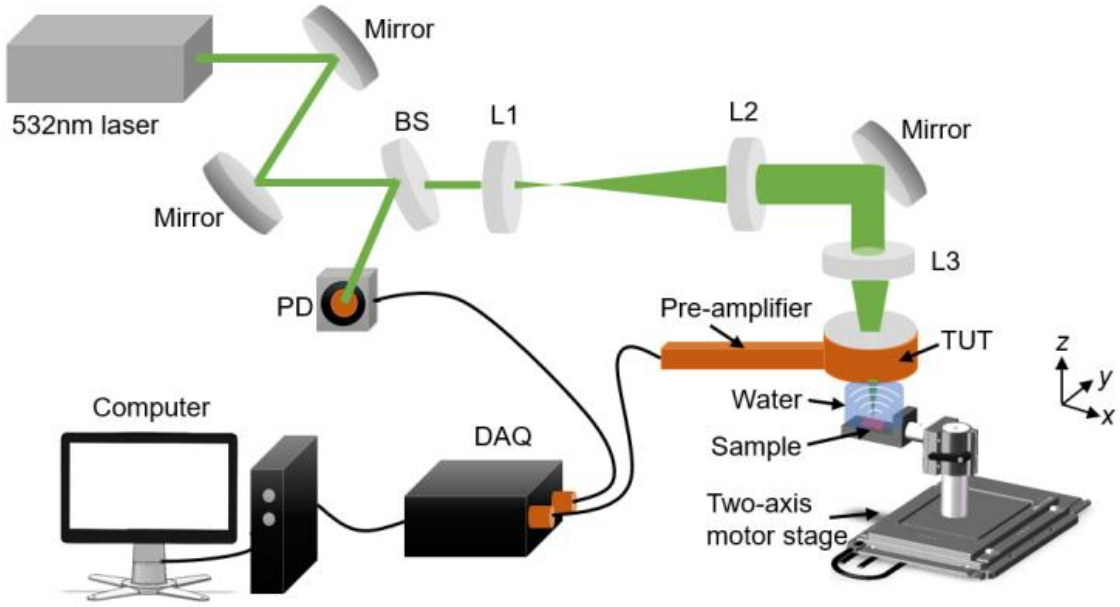

Figure 2.2. Schematic of optical-resolution photoacoustic microscopy (OR-PAM) system based on the developed TUTs. BS: beam sampler; PD: photodiode; L1, L2, and L3: plane convex lenses with focal lengths of 25.4, 150, and 30 mm, respectively.

2.3 Performance of Proposed TUTs

2.3.1 Simulation Study

PiezoCAD software (Sonic Concepts, WA, USA) based on the KLM model was employed to simulate the transducer performance. The LN-based TUTs with the thickness of 150 μm and the aperture size of 9 mm × 9 mm were modeled to simulate the pulse-echo performance in terms of matching layer configuration. Figs. 2.3(a)–(c) show the simulated pulse-echo response of TUTs without matching layer, with λ/4-thick Parylene, and λ/4-thick PMMA as matching layers, respectively. Compared to the TUT

with the Parylene matching layer, the one with the PMMA matching layer exhibits wider bandwidth as well as higher sensitivity. The simulated results indicate that PMMA as the matching layer can improve the performance of TUT much effectively when compared to Parylene.

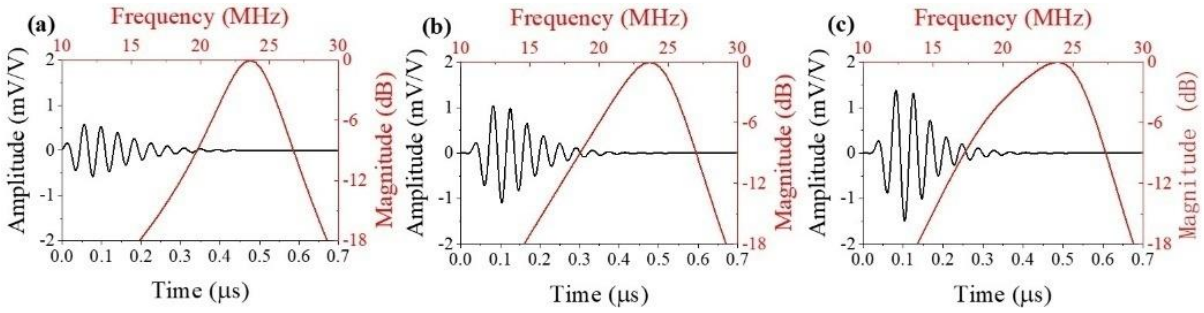

Figure 2.3. Simulated pulse-echo responses of LN-based TUTs **(a)** without matching layer, **(b)** with λ/4-thickParylene matching layer, and **(c)** λ/4-thick PMMA matching layer.

2.3.2 Acoustic Response of TUTs

Fig. 2.4(a) shows the experimental results of pulse-echo response of a TUT with the aperture size of 9mm × 9mm and without matching layer, showing a *BW* of ~17% and a peak-to-peak received voltage of 0.8 V. Figs. 2.4(b)–(d) show the measured pulse-echo responses of TUTs with the 34, 24 and 17 μm-thick PMMA matching layers, respectively.

As shown in Fig 2.4(b), the TUT with the theoretical λ/4-thick PMMA matching layer exhibits the most enhanced pulse-echo sensitivity among the TUTs when compared to other thicknesses of PMMA layer. However, an additional peak is introduced into the frequency spectra at ~13 MHz, indicating that the TUT with the λ/4-thick matching layer is a dual-frequency transducer.

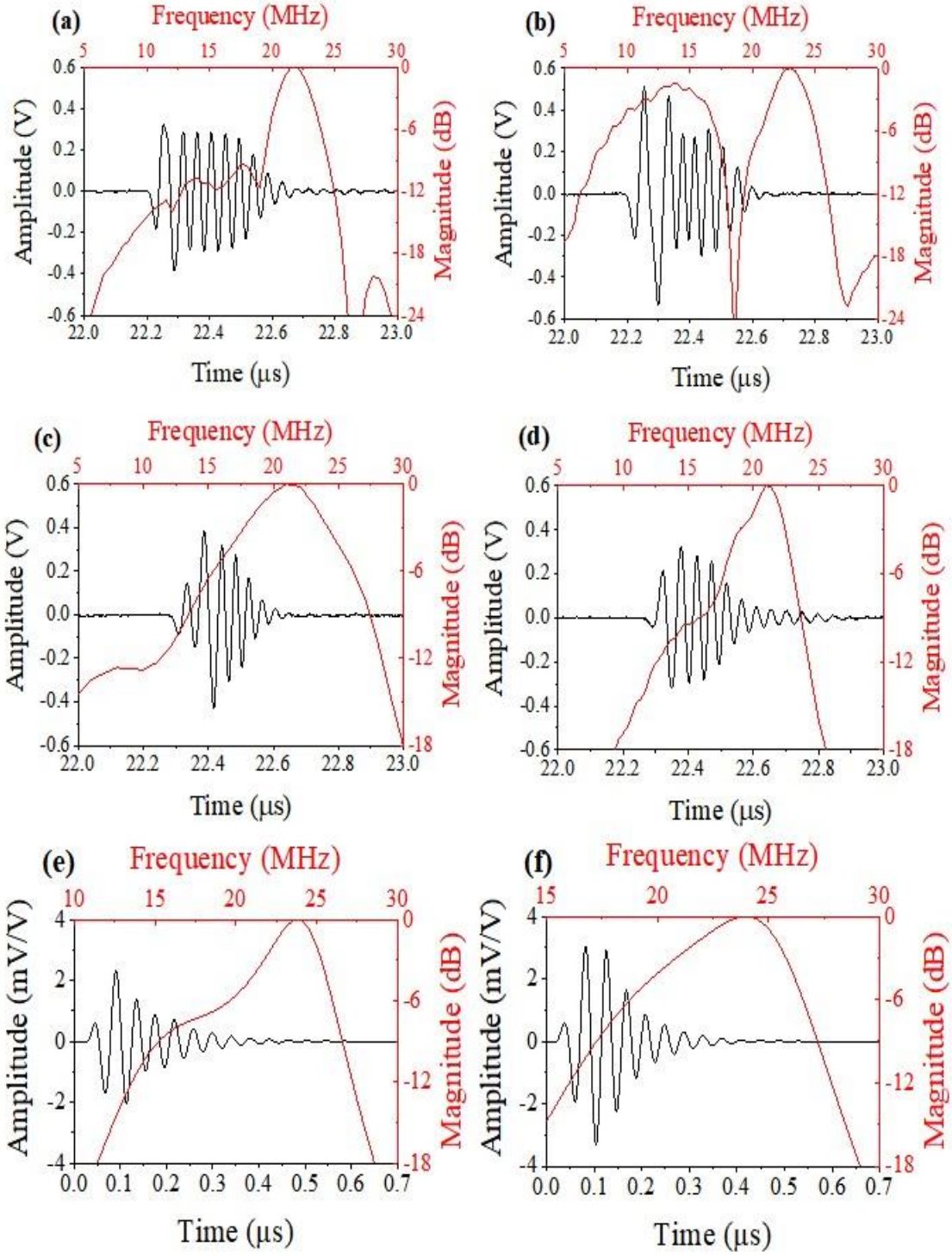

Figure 2.4. Measured pulse-echo responses of 20-MHz TUTs **(a)** without matching layer and with the **(b)** 34 μm (= $\lambda/4$), **(c)** 24 μm, and **(d)** 17 μm-thick PMMA matching layers, respectively. Simulated pulse-echo response of 20-MHz TUT with **(e)** 34 μm (= $\lambda/4$) and **(f)** 24 μm-thick PMMA matching layers.

This phenomenon is considered to be the mass-load effect of a bonded front matching layer, which has also been reported in other literature [33, 34]. Although the

BW at the lower frequency reached 71.4%, the *BW* at the designed center frequency is still limited to 19.2%. For the TUT with the 24 μm-thick PMMA matching layer (Fig. 2.4(c)), the *BW* is significantly improved to 50.4% with the f_c of 20.9 MHz, while the sensitivity of TUT is almost the same as that of TUT without matching layer.

Taking similar acoustic impedances of PMMA and degassed transparent epoxy into account, both matching and bonding layers are likely to contribute together to form a $\lambda/4$ matching layer. Further reduction of the PMMA thickness (17 μm) leads to the lower sensitivity (Fig. 2.4(d)) when compared to the TUT with the 24 μm-thick PMMA layer, though the *BW* is still better than that of the TUT without matching layer. Consequently, the difference in the thickness between the $\lambda/4$-thick matching layer and the optimized PMMA matching layer is considered as the thickness of bonding layer.

Table 2.2. Acoustic performance of TUTs with different thicknesses of PMMA matching layer.

Aperture size (mm × mm)	PMMA thickness (μm)	f_c (MHz)	*BW* (%)	Echo amplitude (V)
9.0 × 9.0	34	12.75/22.9	71.4/19.2	1.04
9.0 × 9.0	24	20.8	50.2	0.80
9.0 × 9.0	17	20.4	27.2	0.64
6.3× 6.3	13	27.8	56.1	0.55

Figs. 2.4(e) and (f) show the simulated pulse-echo responses of TUTs with 34 μm and 24 μm-thick PMMA matching layers, respectively, where the thickness of bonding layer is set as 10 μm. The simulation results indicate that the TUT with the 24 μm-thick PMMA layer exhibits the optimized performance on both *BW* and sensitivity. Similar

to Fig 2.4(b), an additional peak presents at 15 MHz in the simulated FFT waveform of TUT with the 34 μm-thick PMMA layer, leading to the lower sensitivity due to the energy allocation to vibrations at two different frequencies. Table 2.2 summarizes the measured results.

To explore the potential of PMMA matching on the development of TUTs, the study was further performed on the TUTs with the higher frequency. Based on the investigations of the 20-MHz TUTs, the difference in the thickness between the $\lambda/4$-thick matching layer and the optimized PMMA matching layer was considered as the thickness of bonding layer. Thus, a 13 μm-thick PMMA matching layer was applied on a 30-MHz LN-based TUT. Figs. 2.5(a) and (b) show the measured pulse-echo responses of 30-MHz TUTs without and with the PMMA matching layer, respectively.

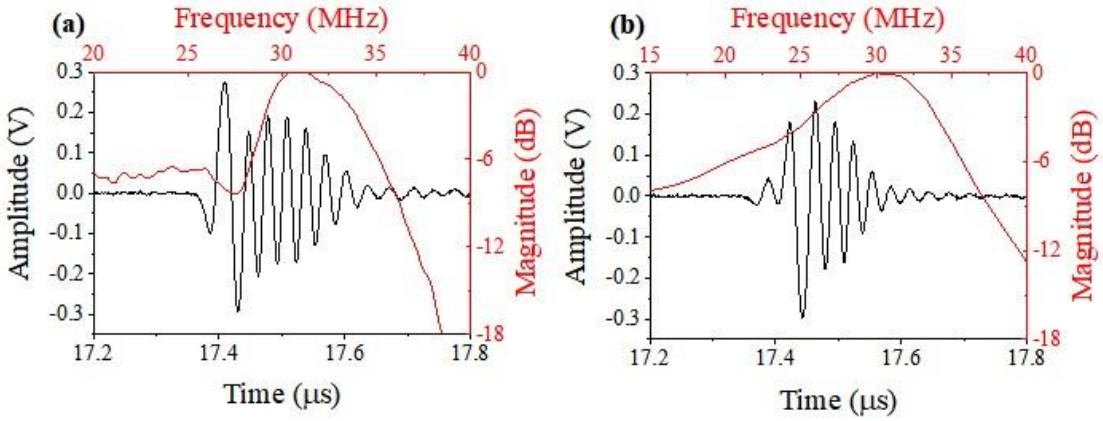

Figure 2.5.**(a)** Measured pulse-echo responses of 30-MHz TUTs without matching layer and **(b)** with the 13 μm-thick PMMA matching layer.

The results demonstrate a substantial enhancement in the *BW* of TUTs, from 21.4% to 56.1%, upon attachment of a 13-μm-thick PMMA layer. Concurrently, the center frequency exhibited a modest decline, from 31.8 MHz to 27.8 MHz. The bandwidth of the TUT is notably broad, exhibiting a ~65% increase compared to the maximum

bandwidth of high-frequency TUTs with a single matching layer reported in the literature [30]. The results demonstrate the validity of the proposed scheme even for developing TUTs with higher center frequencies.

The *IL* of the 20-MHz TUT with a 24 μm-thick PMMA matching layer was measured as 28.4 dB. The acoustic receiving sensitivity was also measured, in which a calibrated commercial 20-MHz US transducer (V317-SM, Olympus NDT Inc.) was driven by a pulser-receiver (5072PR, Olympus) to generate the acoustic wave while the signal was detected by the TUT. The signal-to-noise (SNR) ratio was determined to be approximately 30 dB without the application of averaging, and the noise equivalent pressure (NEP) was calculated to be approximately 66 Pa at the frequency of 20 MHz.

2.3.3 Electrical properties

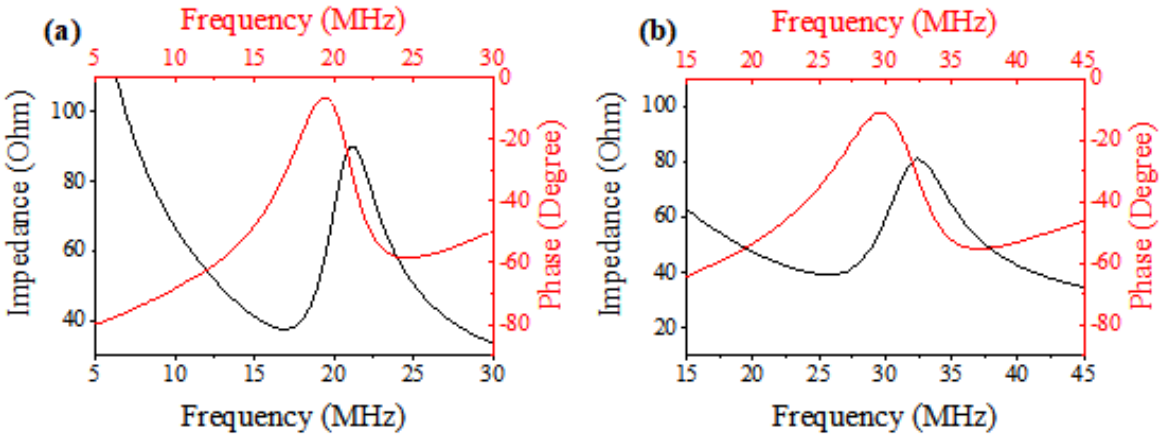

Figure 2.6. Measured impedance spectra of **(a)** a 20-MHz TUT with the 24 μm-thick PMMA matching layer, and **(b)** a 30-MHz TUT with the 13 μm-thick PMMA matching layer.

Figs. 2.6(a) and (b) show the electrical impedance spectra of the 20-MHz TUT with the 24μm-thick PMMA matching layer and that of the 30-MHz TUT with the 13μm-thick PMMA matching layer, respectively. All transducers exhibit pure impedance

spectra without any minor peak, indicating TUTs vibrate with strong resonance peak, and without any spurious mode. The electrical impedances are close to the optimized value (~50 Ω) at f_c. Besides, their k_{eff} are calculated as 0.60 and 0.59, respectively. These values are significantly high compared to other reported TUTs with single matching layer, due to the broad *BW*.

2.3.4 Optical property and PAI performance

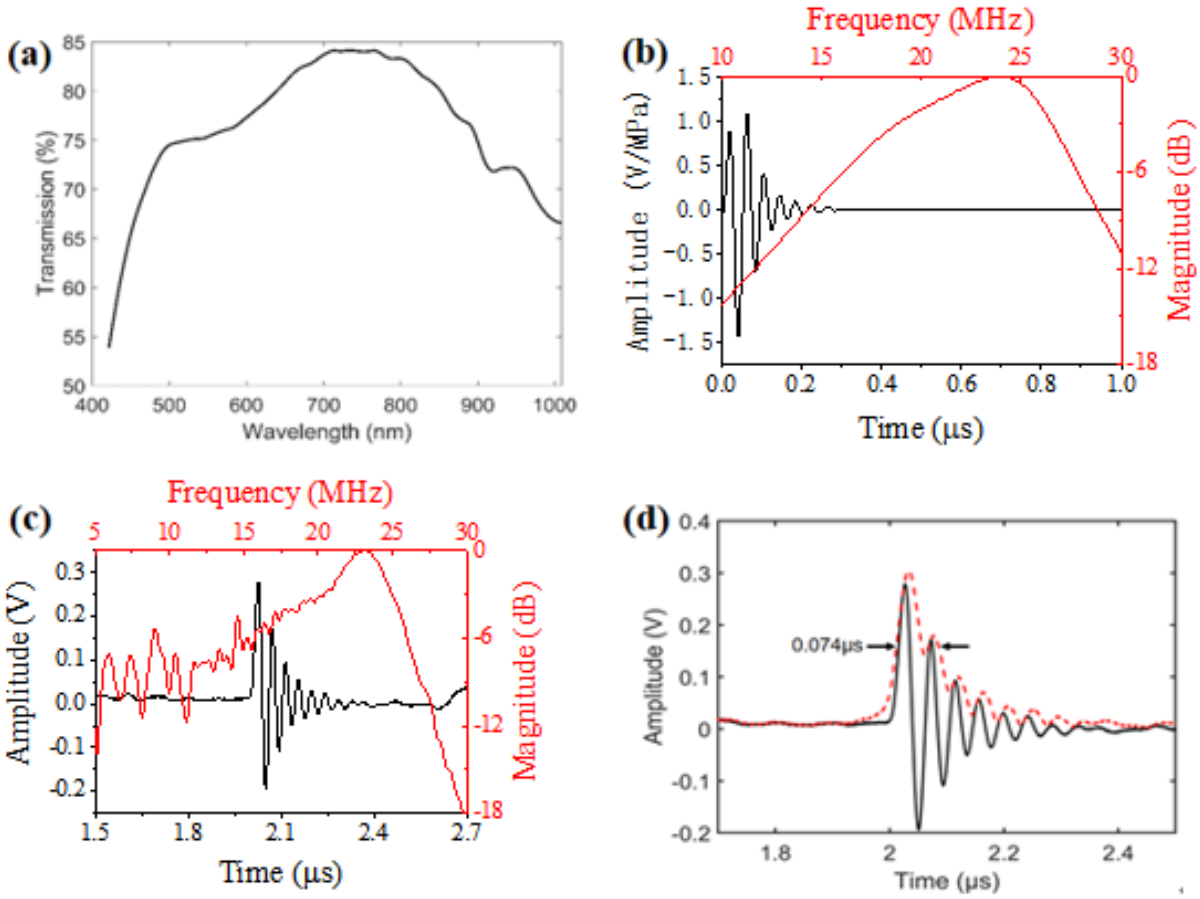

Figure 2.7. (a) Measured optical transmission efficiency of the TUT. **(b)** Simulated one-way receive response of the TUT. **(c)** Time-domain response of TUT to PA signal and corresponding frequency-domain response of a 20-MHz TUT with 24μm-thick PMMA matching layer. **(d)** Axial resolution of an OR-PAM system with TUT, where the black line is the time-domain signal and the red dashed line is the Hilbert enveloped curve

The broadband 20-MHz TUT with 24μm-thick PMMA matching layer was employed to conduct optical measurement due to its large aperture size. Fig. 2.7(a) shows the measured optical transmission efficiency of TUT with the PMMA matching layer to be larger than 70% in the wavelength range of 500 – 900 nm. Although the optical transmission efficiency at 532 nm reduces to ~75% due to the attached PMMA layer, the laser beam may reach the target with enough energy for imaging [37]. Moreover, the peak transmittance can reach close to 85% between 700 nm and 800 nm, which is optimal for deep tissue PAI applications.

To assess the performance of the TUT system, a short-pulse laser was utilized to generate a broadband PA signal by exciting a thin layer of oil-marker paint on a thick glass block. As illustrated in Fig. 2.7(c), the detected time-domain PA signal was obtained without averaging, and the corresponding frequency spectrum was subsequently normalized at the peak value at 20 MHz. This analysis yields a f_c of 20.8 MHz and a BW of 49.3%, which closely corresponds to the simulated one-way receive response of the TUT (Fig. 2.7(b)). The theoretical value of axial resolution was calculated from $0.88v/BW$, which depends on the bandwidth of the TUT (BW) and the acoustic speed (v) [65]. Although the reported work also achieved a similar PA bandwidth with the TUT employing a transparent matching layer consisting of epoxy and glass beads (40% volume fraction), the TUT with the PMMA layer owns higher optical transmission efficiency without light scattering. As OR-PAM requires tight light focusing, the TUT with the PMMA layer is more suitable for this application. Fig. 2.7(d) shows the absolute value after performing the Hilbert transform on the time-domain

response of TUT to the PA signal. The axial resolution of the system is 111 μm obtained from the full-width half-maximum (FWHW) of the envelope curve, which is close to the theoretical value (126 μm). The broadband TUT leads to the improved axial resolution when compared to the reported TUT-based work even operated at higher center frequency.

The imaging capability of the 20-MHz TUT with the 24μm-thick PMMA matching layer was evaluated using the OR-PAM system as shown in Fig. 2.8. The lateral resolution of the system was measured by imaging the cutting edge of a razor blade at a scanning step size of 0.5 μm. The maximum amplitude projection (MAP) image of blade is shown in Fig.2.8(a), which is averaged 10 times. The edge spread function (ESF) is shown in Fig. 2.8(b), and the line spread function (LSF) is the first derivative of ESF. Then, the lateral resolution of the system is calculated to be 8 μm based on the FWHW of the LSF.

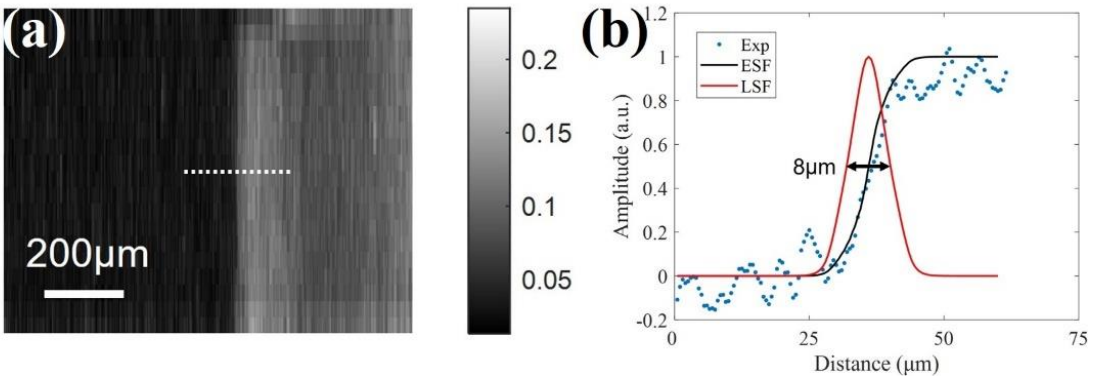

Figure 2.8 (a) PA MAP image of a sharp razor blade. **(b)** Lateral resolution of an OR-PAM system with TUT, where blue dots are the experimental data, a black line is the fitted ESF, and a red line is the derived LSF.

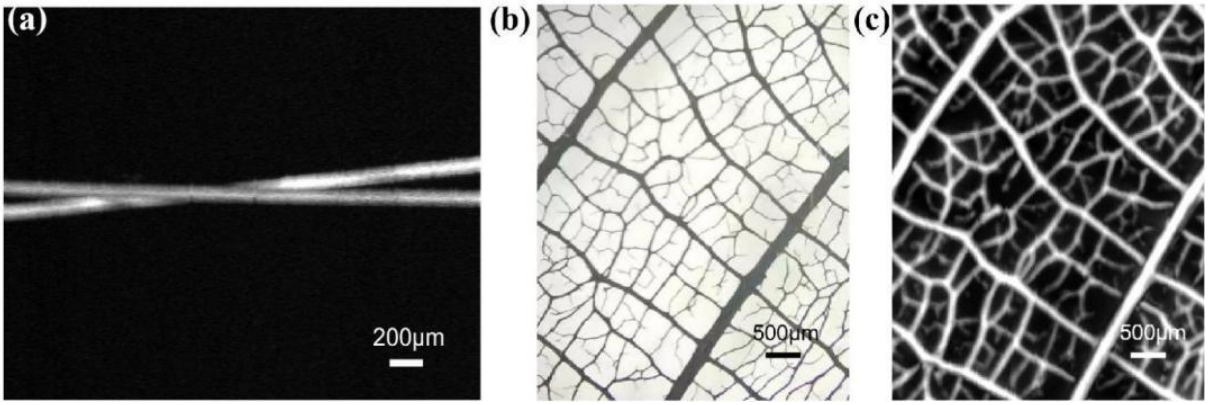

Figure 2.9. (a) PA imaging of a cross of human hairs. **(b)** Light field microscope photograph and **(c)** PA imaging of the ink-stained leaf skeleton phantom.

The PAI performance of the 20-MHz TUT with the 24μm-thick PMMA matching layer was evaluated via phantom and *in vivo* small animal models. A cross of hairs and leaf veins were employed as the phantom models. To image a cross-section of hairs, a step size of 2 μm in X direction and 5 μm in Y direction was used to perform a 2×3 mm^2 scanning area. The repetition rate of the 532-nm pulsed laser was 1 kHz, and the sampling rate of the acquisition card was set to 200 MHz. The reconstructed MAP PA image without averaging is shown in Fig. 2.9(a). To image the ink-stained leaf skeleton phantom, a step size of 5 μm was adopted in both X and Y directions. Even with a more complex structure, the OR-PAM imaging result of the leaf vein network corresponds well with the photograph taken by the light field microscope, as shown in Figs. 2.9(b) and (c). All phantom images show high contrast and resolution of the system using the developed TUT.

A BALB/c nude mouse was used for the *in vivo* imaging experiment as shown in Figs. 2.10(a) and (b). The mouse was first anesthetized by inhaling isoflurane gas and then fixed on the translation stage. The distance between the mouse ear and TUT was ~1.2 mm, and a drop of distilled water was used as the ultrasound coupling medium.

The PA signal was acquired by a step size of 1 μm in x direction and a step size of 5 μm in y direction with data averaging 10 times. The scanning area is 1.5 mm × 4.2 mm, and the laser energy on the surface of mouse ear skin was measured to be ~1 μJ, which slightly exceeds the maximum recommended value of ANSI for safe use of lasers [66]. An infrared lamp was used to maintain the body temperature of the mouse during the experiment. All research works performed in the laboratory followed the protocols that were approved by the Institutional Animal Care and the Use Committee of Peking University. The PA MAP image of mouse ear is shown in Fig. 2.10(c), in which both capillaries and the two large accompanying arteries and veins are clearly reconstructed.

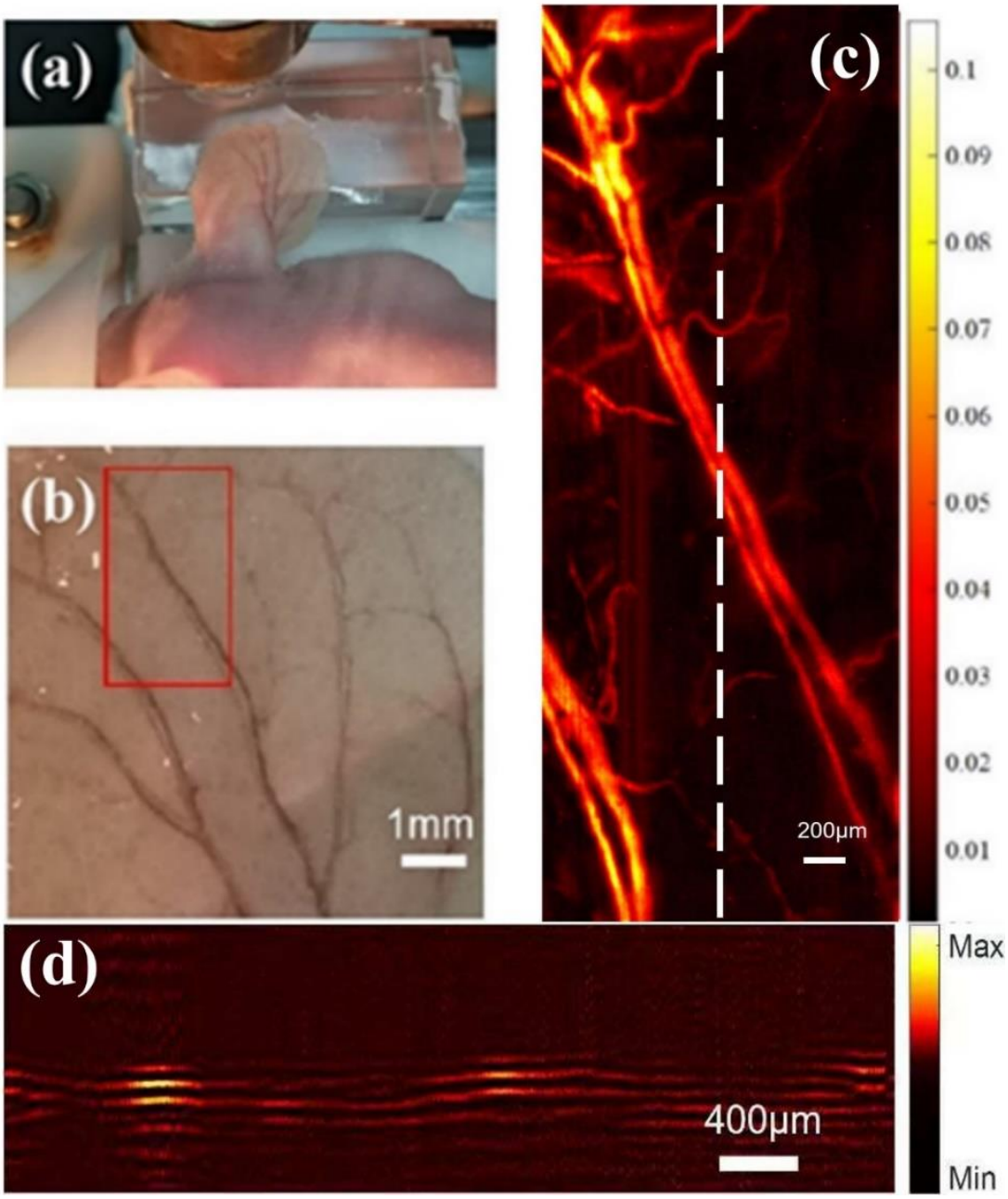

Figure 2.10. Photographs of **(a)** the setup of mouse ear, and **(b)** *in vivo* imaging area. **(c)** MAP image of *in vivo* vascular networks in the area indicated by the box in (b). **(d)** Reconstructed depth-resolved slides at the location marked with a white dash line of (c).

Although the optimal thickness design of the matching layer improves the -6 dB bandwidth and enhances the full-width half maximum (FWHM) resolution, the design introduces a prolonged ringing tail in the temporal echo response that can constrain the effective resolution of the imaging system. In situations where a weak blood vessel

signal is positioned beneath a strong blood vessel signal in terms of depth, the weak signal may be overwhelmed by the long ringing tail of the strong blood signal. Consequently, this may lead to the inability to distinguish between the two blood vessels, thereby causing a reduction in the actual resolution. Besides exploring other matching materials, another potential future approach to mitigate this effect involves advanced signal processing such as deconvolution or machine learning. Fig. 2.10(d) shows one of the reconstructed depth-resolved slides at the location marked with a white dash line of Fig. 2.10(c). The locations of main vasculature are in good agreement with MAP images of vascular networks in the area. Some reflected signals are mainly caused by the light backing layer of TUT.

2.4 Discussion

In terms of TUT design, piezoelectric single crystals and ceramics have high acoustic impedance (> 30 MRayl), therefore, carefully acoustic matching design is essential. Although PAI has been successfully demonstrated employing TUT without matching layer, the photoacoustic axial resolution of reported TUT is always low due to narrow bandwidth and low sensitivity. Table 2.3 summarizes the bandwidth of reported TUT without or with single matching layer. Although polymer materials are transparent, their acoustic impedances are improper, therefore, the bandwidths of the TUTs with these materials are not significantly improved due to their low acoustic impedance.

Table 2.3. Bandwidth of reported transparent ultrasound transducers without or with a single matching layer

f_c (MHz)	BW (%)	Matching layer	Theoretical PAI Axial Resolution (μm)	Measured PAI Axial Resolution (μm)	Reference
13	25	/	169	150	[27]
36.9	33.9	Parylene C	105.9	105	[30]
10	16.46	EPO-TEK 301-2	782.5	/	[31]
13	36	Parylene C	282.1	202.5	[29]
11.93	22.43	15% volume fraction glass beads/epoxy	316	149.3	[38]
20	50	PMMA	126	111	This work

Double matching layer scheme results in better acoustic matching performance compared to that of single matching layer, and considering the acoustic impedance, glass may be a potential choice as the first matching layer. However, the heavy load of bonded glass may dampen the vibration of piezoelectric materials such that the actual (measured) frequency derives from the designated (theoretical) one. There have been studies of TUTs using glass as the quarter-wavelength-thick first matching layer and quarter-wavelength-thick Parylene C as the second matching layer, but the bonded glass matching layer severely decreases the designated center frequency of transducers as indicated in Table 2.4. By theory, a matching layer with a thickness deviate from quarter-wavelength cannot effectively improve a transducer's bandwidth. The quarter-wavelength thickness design is suitable for the matching layer fabricated by vapor-deposition or casting in which the matching layer can be attached onto the piezoelectric layer directly. However, due to the physical characteristics of glass, another alternative

approach should be employed involving lapping glass to the desired thickness and then bonding onto the surface of piezoelectric layer using a bonding agent. Nevertheless, different from the casting method, the thickness of bonding agent cannot be ignored, since it may influence the propagation of ultrasonic signal. Some studies even showed that the resonance mode was suppressed and changed into a dual frequency resonance, which was undesired from the viewpoint of working principle of transducer technology. The phenomenon also hinders the development of high-frequency transparent ultrasound transducers. For the dual-frequency transducers due to the bonding of quarter-wavelength thick heavy matching layer, the heavy load may not only decrease the vibration frequency of piezoelectric material but also introduce the low-frequency signal because of the mass-load effect. Although the low-frequency signal introduced may improve the bandwidth of pulse-echo signal, it may not contribute to the practical imaging applications as the superposition of two signals extend the pulse length. In theory, the axial resolution of ultrasound imaging is highly related to the bandwidth of transducer. However, the axial resolution measured from imaging cannot match well with the theoretical value calculated from the broad bandwidth. As indicated by researchers, although both the pulse-echo response and photoacoustic A-line showed the improved bandwidth, the axial resolution was reduced when compared to the previous work based on a TUT with no matching layer [27, 33]. Thus, such a design may not be applicable to the development of transparent ultrasound transducers for high-frequency or high-resolution applications. Noted that the reduction in the weight of the attached layer may improve the issue [38], the thickness of bonded matching

layer needs to be optimized instead of the traditional quarter-wavelength design. Researchers tried to adjust the thicknesses of matching layer materials such as glass (the first matching layer) and Parylene (the second matching layer) as summarized in Table 2.4.

Table 2.4. Performance of reported TUTs with double matching layers

Piezoelectric Material	f_{c}((MHz)	BW (%)	First matching layer	Second matching layer	Theoretical PAI Axial Resolution (μm)	Measured PAI Axial Resolution (μm)	Ref.
LN (250 μm)	7.2/11.8	36.1/62.7	Glass (100 μm)	Parylene C (40 μm)	/	375.9	[33]
AC-poled PMN-PT (200 μm)	7.8/13.2	28.2/66.67	Glass (100 μm)	Parylene C (40 μm)	/	285.6	[33]
LN (130 μm)	7.5/31.5	200/ 25.4	Glass lens	Parylene C (21 μm)	/	91	[34]
DC-poled PMN-PT (400 μm)	8	45	Glass lens	Parylene C (5 μm)	/	/	[41]
LN (250 μm)	6	50	Glass (100 μm)	Parylene C	/	/	[37]
LN (250 μm)	13	60	Glass (100 μm)	Parylene C (10 μm)	/	/	[36]
LN (100 μm)	34	18..3	Glass lens	Parylene C (10 μm)	215	208	[35]
PMN-PT	28.1	51.5	Glass	Parylene C		45	[42]

Though the thickness of Parylene was adjusted to avoid the drop of center frequency, the same strategy did not work to achieve higher frequency in the subsequent work. Later on, the thickness of glass was carefully adjusted instead of quarter-wavelength thick. However, the approach may only work for developing transducers with a specific frequency. Transparent matching layer with low viscosity was

investigated to solve the problem by casting it onto piezoelectric layer before curing. Although the broad-bandwidth and high-sensitivity TUT based high-resolution PAI system has been successfully developed, the fabrication process is complex. For TUT with high frequency, it may bring extra risk of thin acoustic stacks cracking. In this study, the PMMA layer with optimized thickness could improve the bandwidth to 50%. As an simple and universal acoustic matching method, this work protect the TUT from dual-frequency phenomenon.

There is one limitation in this study is the limited sensitivity of the developed TUT. During the in *vivo* PAI experiment, the laser energy density exceeds the safety range to enhance the generated acoustic waves. Common transparent sensors for PAI detection include optics-based sensors, MEMS-based sensors, and piezoelectric-based sensors in this study. Some representative sensors are concluded in Table 2.5.

The CMUT-based TUT exhibits advantageous properties, including a broad bandwidth and relatively high sensitivity. However, its operational mechanism is contingent on the application of a high bias voltage. The high voltage may introduce additional risks for practical biomedical imaging applications. Furthermore, the current CMUTs possess relatively low fc (lower than 20 MHz), which are not considered optimal for PAI ranging of 20-50 MHz. Optical sensors, exemplified by the Fabry-Perot sensor, offer distinct advantages, including a wide bandwidth and high sensitivity. Furthermore, these nanostructures exhibit a high degree of compatibility with fibers employed for laser delivery. However, the utilization of optics-based sensors is impeded under optimal conditions due to the absence of natural focus points.

Table 2.5. Performance of different types of TUTs

Sensor Type	Sensor Structure	Size	Transparency	Performance	Ref
Optics based sensor (FP sensor)	Material: Parylene C Matching layer: CNT-PDMS; Backing layer: N/A	64 μm	N/A	f_c: N/A *BW*: 22 MHz NEP: N/A	[20]
Optics based sensor (FP sensor)	Material: Parylene C Matching layer: PMMA Backing layer: N/A	50 μm	N/A	f_c: N/A *BW*: 22 MHz NEP (estimated): 47 mPa/Hz $^{1/2}$	[20]
Optics based sensor (FP sensor)	Material: SU-8 photoresist Matching layer: N/A Backing layer: Polymer	10 μm	N/A	f_c: 50 MHz *BW*: 100 MHz NEP (estimated): 200 mPa/Hz $^{1/2}$	[20]
Optics based sensor (MRR sensor)	Material: SU-8 Matching layer: N/A Backing layer: N/A	250 μm	N/A	f_c: N/A *BW*: 140 MHz NEP (estimated): 0.57 mPa/Hz $^{1/2}$	[20]
Piezoelectric based TUT	Material: LN Matching layer: N/A Backing layer: Epoxy	3×3 mm^2	90% at 532 nm	f_c: 12.4 MHz *BW*: 3 MHz NEP (measured): 15.7 mPa/Hz $^{1/2}$	[67]
CMUT	Material: Silicon Matching layer: N/A Backing layer: N/A	~19 μm radius	~ 90% in the visible and NIR range	f_c: 8 MHz *BW*: 6 MHz (75%) NEP (measured): 10.4 mPa/Hz $^{1/2}$ (250 V bias)	[68]
Piezoelectric based TUT	Material: LN Matching layer: PMMA Backing layer: Epoxy	9×9 mm^2	75% at 532 nm	f_c: 20 MHz *BW*: 10 MHz NEP (measured): 14.8 mPa/Hz $^{1/2}$	This thesis

Of particular significance is the challenge of utilizing optics-based sensors to transmit ultrasound waves for ultrasound imaging, a process that is frequently desired in conjunction with PAI for dual-modality imaging applications. In summary, it is imperative to enhance the sensitivity of piezoelectric-based TUTs for ultrasound/photoacoustic imaging in forthcoming studies.

2.5 Conclusion

In this chapter, bonded PMMA with optimized thickness was used as a matching layer to enhance bandwidth of transparent ultrasound transducer up to over 50%. Improved photoacoustic axial resolution was obtained, which shows effectiveness of the broad bandwidth. Also, phantom and *in vivo* imaging was conducted, showing good capabilities for optical-resolution photoacoustic microscopy. Advantages of using bonded PMMA with optimized thickness as matching layer can be concluded as

1. The major advantage is the great improvement of bandwidth, which is ~65% increment even when compared to the maximum bandwidth of high-frequency TUTs reported in literature with a single matching layer.

2. The proposed bonded PMMA matching layer with optimized thickness is universal to TUTs with different center frequency, which has been validated by a 30 MHz transducer in this study.

Chapter 3. Study on Transparent Piezoelectric Materials for Single Element TUT Application

Nowadays, limited by transparency, only a few kinds of piezoelectric materials have been investigated for TUT design and fabrication. Properties of these transparent piezoelectric materials are summarized in Table 3.1.

Table 3.1 Properties of transparent piezoelectric materials for TUTs.

Piezoelectric Material	d_{33} (pC/N)	Dielectric constant	k_t
PVDF	20	20	0.2
P(VDF-TrFE)	36	16	0.3
LN	39	65	0.5
DC-poled PMN-PT Single Crystal	1400	5800	0.58
AC-poled PMN-PT Single Crystal	2200	7800	0.58
3D Printed Er doped KNNLN	97	/	0.36

Piezoelectric polymers, including PVDF and P(VDF-TrFE), possess high receiving sensitivity and high flexibility to form a focused transducer. Moreover, the low acoustic impedance of these polymers (< 4MRayl) can match well with biological issues, leading to high acoustic transmission coefficient and broad bandwidth. However, their k_t and d_{33} are low, limiting their capability for ultrasound imaging with high signal-noise-ratio (SNR). They may only be applicable to specific applications where receiving-only is required. Nowadays, more efforts have been spent on simultaneously ultrasound/photoacoustic imaging [69]; this leads to more requirements for high-

performance TUTs. Most reported TUT may only perform PAI, instead of combining with ultrasound imaging to provide structural information; mainly limited by poor performance of TUT under pulse-echo model.

In this situation, the novel AC-poled relaxor-PT single crystals provide great opportunities for further development of TUT. From the aspect of piezoelectric material, the technology may not only improve the piezoelectric properties, but also increase light transparency efficiency [44]. Except for PMN-PT, other similar AC-poled single crystal, such as $Pb(In_{1/2}Nb_{1/2})O_3$-$Pb(Mg_{1/3}Nb_{2/3})O_3$-$PbTiO_3$ (PIN-PMN-PT), may also be employed. As a cutting-edge technology, conditions of AC-poling are under debate [33, 70, 71], where key factors of AC-poling, including numbers of cycles, amplitude of electric field, and frequency of AC field, should be carefully studied to find out the most optimized poling conditions. Also, the piezoelectric layer suffers from high-voltage and high-frequency pulses, whose amplitude is always larger than that of AC-poling voltage. It is totally different from the research focusing on materials only; in addition, to avoid de-poling, the single crystal was always poled after fabrication. For transparent electrode, although ITO and silver nanowire can reach relatively low sheet resistance, the sheet resistance of electrode layer may need to be considered during poling process.

Among all relaxor-PT single crystals, PZN-PT, possessing relatively high transparency, is considered a good candidate as transparent piezoelectric materials for TUT applications. Rare-earth element doped PT-based ceramics by hot-pressing

fabrication method, which possess high dielectric constant, also hold potential for TUT with miniaturized aperture size for ultrasound/photoacoustic endoscopy imaging.

3.1 AC-poled PMN-28PT Single Crystal based TUT

There have been large number of studies on AC-poling conditions of relaxor-PT single crystals. By changing domain structure, the single crystal not only shows enhanced piezoelectric properties, but also higher transparency. This technology has been employed for low-frequency opaque ultrasound transducers to improve their performance. However, very few studies have applied AC-poling technology on high-frequency TUTs. Although this technology has been widely accepted in the field of material science, the capability for practical TUT application is still challenging. Chen *et al* showed significance of AC-poled PMN-PT for the TUT application compared to the LN single crystal [33]. However, the latest study employing PIN-PMN-PT single crystal for TUT applications indicates that the TUT based on novel material performs worse compared to LN-based TUT under pulse-echo mode. Thus, the AC-poling condition focusing on TUT application needs to be intensively studied.

3.1.1 Preparation of PMN-PT based TUT

PMN-28PT single crystal was selected as the piezoelectric material. The TUTs were prepared by following fabrication process:

1. The PMN-PT was lapped and polished to 95 μm thickness, and ITO electrode was sputtered on one surface of the piezoelectric stack.

2. The crystal was diced into desired aperture size.

3. Each well-diced acoustic stack was stabled on flat glass substrate by double-sided tape with the electroded surface facing up.

4. A brass housing was placed around the stack, and a co-axial cable was connected to the ITO electrode and housing using E-solder sliver-epoxy.

5. Transparent EPO-TEK 301 was degassed and filled into the housing as the backing layer.

6. Curing at room temperature overnight, the TUT was removed from the glass substrate, and ITO sputtering process was conducted to achieve ground connection. Finally, the distal end of the co-axial cable was connected to a SMA connector

7. Ferroelectric analyzer was employed for AC-poling, where continuous triangle wave was applied on the developed TUT.

Similar to previous work, to enhance the transparency of PMN-PT, low frequency 1 Hz AC poling was used, and the effect of different poling voltages and numbers of cycles was studied.

3.1.2 Investigations on AC-poled TUT

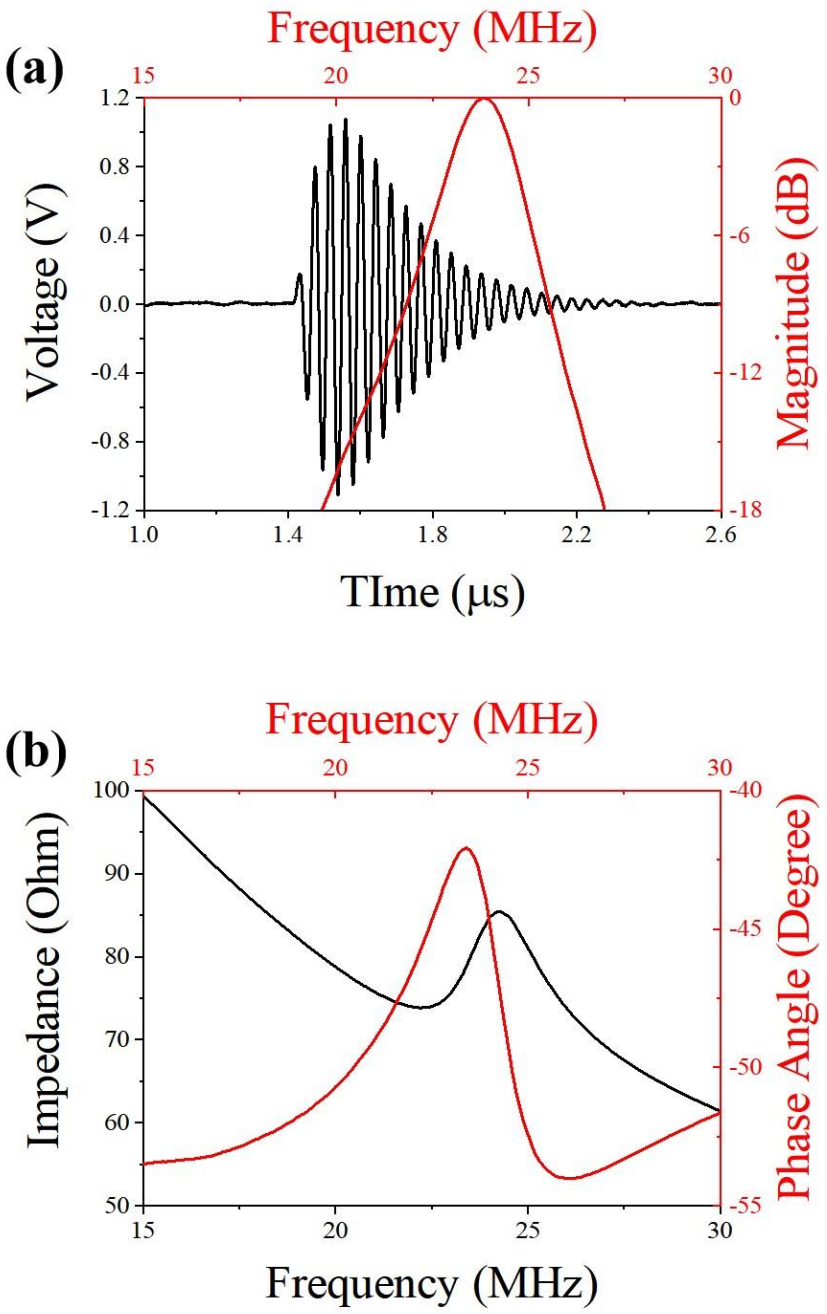

Figure 3.1. Measured **(a)** pulse-echo response, and **(b)** impedance spectra of the DC-poled PMN-PT based TUT

A PMN-PT based TUT with the same scheme and poled by conventional DC electrical field was measured as the reference. The TUT was poled under 1V/μm for 15 minutes, and measured pulse-echo response (1μJ energy, 40dB gain) and impedance spectra are

shown in Figs. 3.1(a) and (b). One can see that the peak-to-peak amplitude of the echo signal is over 2.0 V.

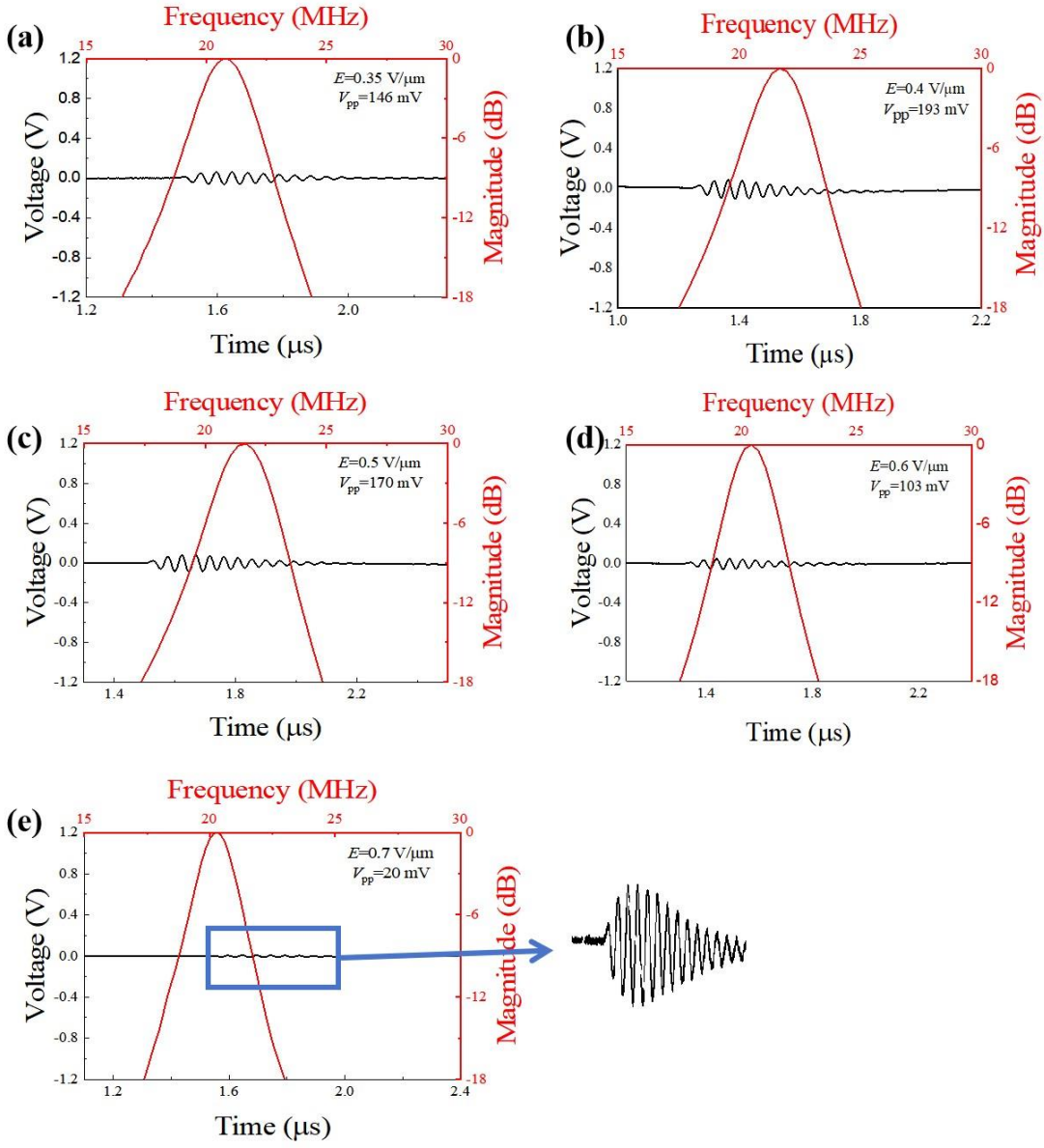

Figure 3.2 Measured pulse-echo response of the TUTs that poled by 10-cycle, 1Hz AC electrical field of **(a)** 0.35V/μm, **(b)** 0.4V/μm, **(c)** 0.5V/μm, **(d)** 0.6V/μm, and **(e)** 0.7V/μm.

First, 10-cycle triangle waves were investigated for AC-poling. Electrical fields with different peak-to-peak amplitudes were applied ranging from around 0.4 times of coercive field (E_c) to over $2E_c$. Fig. 3.2 shows some measured pulse-echo responses for different TUTs. When the electrical field is lower than 0.35V/μm, there is no detected

signal, but when the electrical field is increased and equals to *Ec*, the best signal can be obtained. Further increase in the electric field leads to degraded signal intensity. Corresponding impedance spectra of these 10-cycle AC poled TUTs were also measured, and the results are shown in Fig. 3.3. Correspondingly, when the electrical field is lower than 0.35V/μm, there is no obvious f_r and f_a of the TUT, while the f_r and f_a of TUTs become stronger with the increase of electrical field reaching 0.5 V/μm. Further increasing the electrical field leads to degraded waveform.

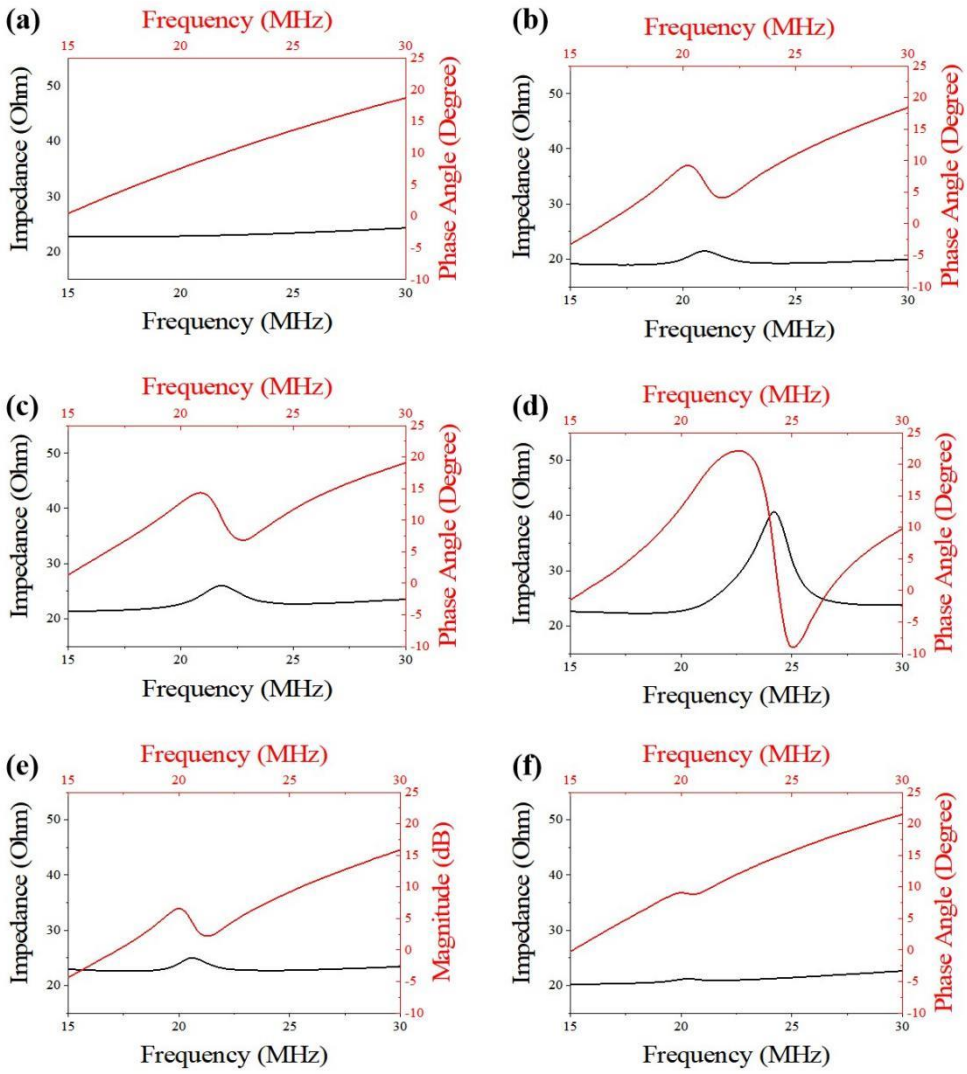

Figure 3.3 Measured impedance spectra of the TUTs that poled by 10-cycle, 1Hz AC electrical field with **(a)** 0.3V/μm, **(b)** 0.35V/μm, **(c)** 0.4V/μm, **(d)** 0.5V/μm, **(e)** 0.6V/μm, and **(f)** 0.7V/μm

The number of cycles was then increased to 30, and different AC electrical fields

were applied. Based on results of 10-cycle AC poling, the lowest electrical field was set as 0.35V/μm and increased to the value over $2E_c$. Fig. 3.4 shows some measured pulse-echo responses of TUTs poled by different electrical fields. Corresponding impedance spectra were also measured for these successful AC-poled TUTs, as shown in Fig. 3.5. Also, the impedances shown in Figs. 3.5 (a) and (b) are slightly higher than other TUTs. This indicates that the ε_s is closer to that PMN-PT poled by conventional DC electrical field.

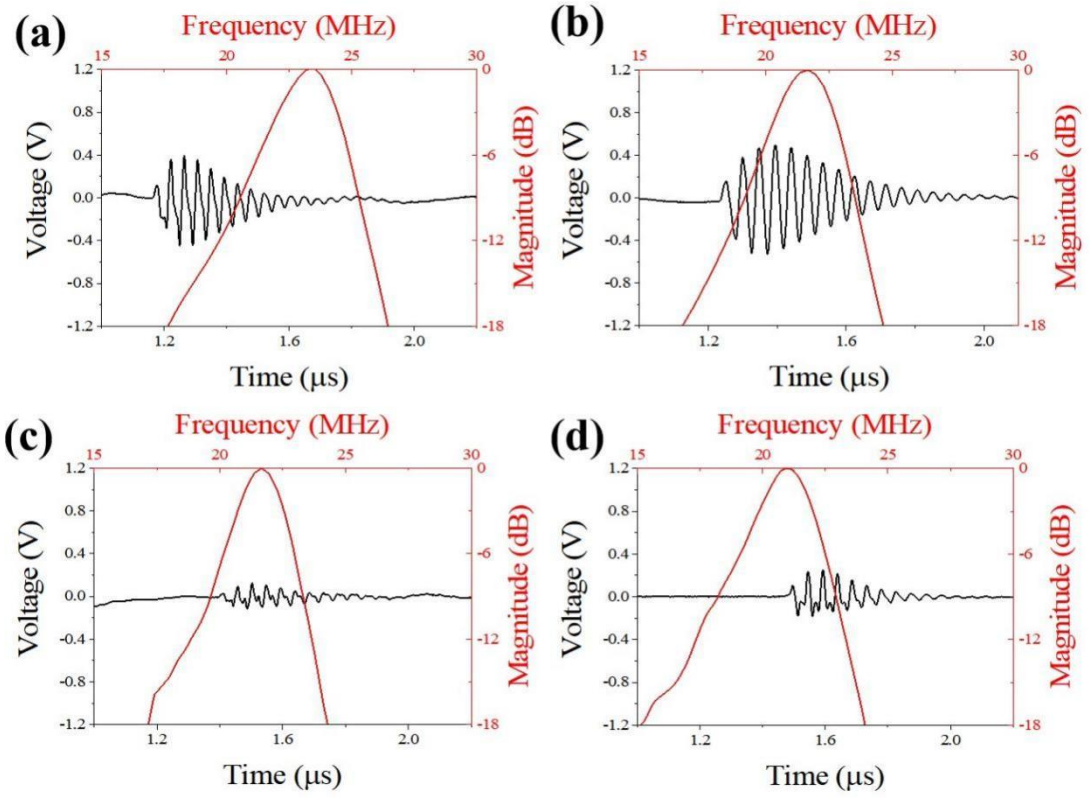

Figure 3.4 Measured pulse-echo response of the TUTs that poled by 30-cycle, 1Hz AC electrical field with **(a)** 0.35V/μm, **(b)** 0.5V/μm, **(c)** 1V/μm and **(d)** 1.4V/μm

It can be found that the most optimized TUT performance always occurs when the electrical field equals to E_c, while further increasing the electrical field may degrade the TUT performance. As the AC electrical field consists of positive and negative parts, the

peak-to-peak amplitude of the applied AC electric field may be two times of the designed value. Thus, the equivalent poling electrical field can be considered as the same value as DC poling.

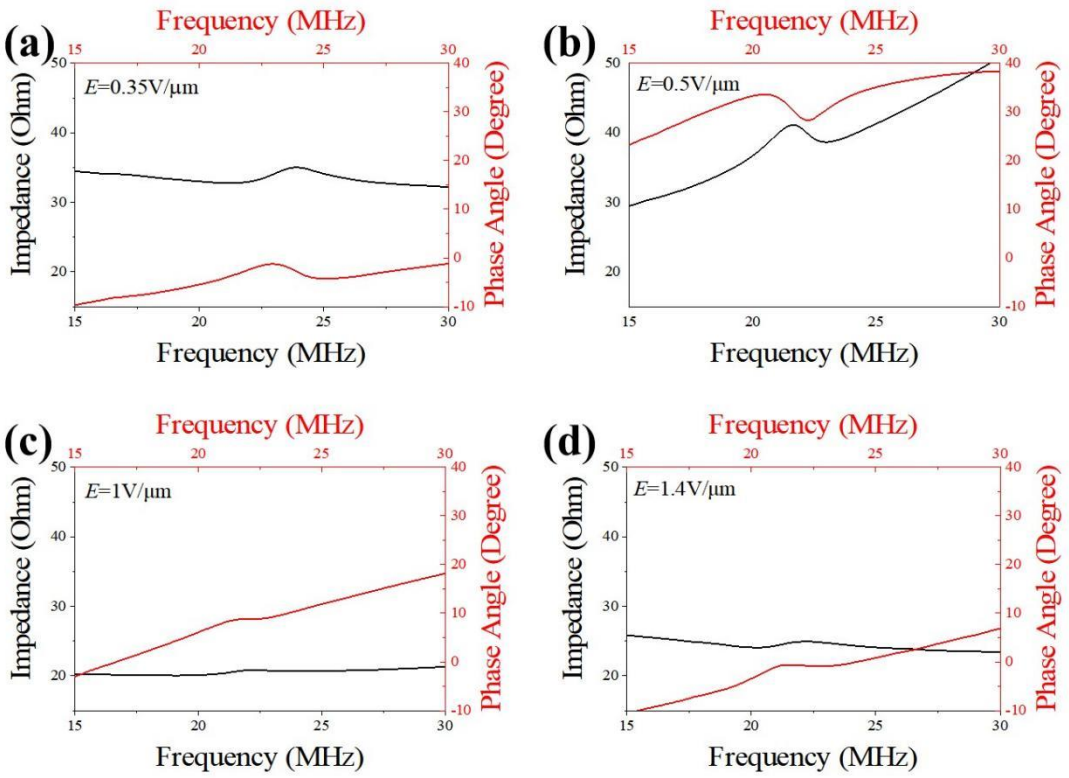

Figure 3.5 Measured impedance spectra of the TUTs that poled by 30-cycle, 1Hz AC electrical field with **(a)** 0.35V/μm, **(b)** 0.5V/μm, **(c)** 1V/μm and **(d)** 1.4V/μm

With proper AC electrical field, increasing the number of cycles can enhance the performance of TUTs. TUTs remain inferior to those poled TUTs under DC electrical fields. The increased number of cycles may offer a viable solution, but it should be noted that the PMN-PT stack may undergo cracking if the number of cycles is increased to a substantial value.

In conclusion, it is challenging to apply the AC-poled technology for practical high-frequency TUT applications. Except for PMN-PT based TUT, PIN-PMN-PT based TUT also suffers from similar challenges, where its *IL* is significantly lower than the

LN based TUT [45]. More attention should be paid to study the gap between advanced materials and high-performance instrumentation.

3.2 PZN-PT Single Crystal based TUT

Conventional DC-poled single crystal has been demonstrated to achieve satisfactory transparency for the TUT application. The DC-poled PMN-PT has been shown to exhibit over 70% transparency at specific wavelengths through careful lapping and polishing [41], and it has been studied for ultrasound/photoacoustic endoscopy applications [42]. Among all kinds of relaxor ferroelectric single crystals, [001]-oriented $Pb(Zn_{1/3}Nb_{2/3})O_3$-$PbTiO_3$ (PZN-PT) single crystal has been widely employed for ultrasound transducer applications due to its great piezoelectric properties [72, 73]. Compared to commonly used PMN-28%PT, PZN-PT possesses similar dielectric constant but much higher d_{33}, leading to higher g_{33} value for better receiving sensitivity [74, 75]. It has been proved that the majority of the domain walls in DC-poled PZN-PT is the 109° neutral domain walls [76], which leads to higher transparency. In aspect of optical property, the widely distributed 71° charged walls blocks transparency of DC-poled PMN-PT [77]. Therefore, we investigate DC-poled PZN-PT as active layer for TUT in this study. Piezoelectric properties of the PZN-PT single crystal were studied, and optimized design of TUT based on the DC-poled PZN-PT was conducted. Ultrasound imaging and PAI were conducted to evaluate the performance of the TUT.

3.2.1 TUT Design and Fabrication

The unpoled [001]-oriented PZN-5.5%PT was purchased from BEIJING SUPERSONIC TECHNOLOGY CO., LTD., Beijing, China. With sputtered Cr/Au electrode, the ferroelectric properties of the single crystal were first measured by the ferroelectric tester system (Precision Premier II, Radiant Technologies, USA), to indicate the coercive field (E_c). After poling the PZN-PT according to E_c, the d_{33} was then measured by the piezoelectric constant meter. Meanwhile, the electromechanical coupling coefficient (k_t), free dielectric constant (ε_r) and clamped dielectric constant (ε_s) were measured by the impedance analyzer (4294A, Hewlett-Packard, USA)

PiezoCAD software was employed for simulation of optimized TUT design based on the KLM model. In this study, TUT was designed as 20 MHz for high-frequency applications. Optically transparent epoxy (EPO-TEK 301, Epoxy Tech., USA) was employed as backing layer, and optimized-thick PMMA was set as matching layer. Considering sheet resistance of ITO electrode, the electrical impedance of PZN-PT based TUT was simulated as around 10 Ohm to determine its aperture size. Parameters of active and passive materials are listed in Table 3.1.

Table 3.1 Properties of active and passive materials for PZN-PT based TUT

	Sound Velocity (m/s)	Density (g/cm^3)	Acoustic Impedance (MRayl)
PZN-PT	4060	8350	33.9
PMMA	2750	1175	3.2
EPO-TEK 301	2650	1132	3.0

The fabrication process of the PZN-PT based TUT was along with the conventional transducer technology. The well poled PZN-PT single crystal stack was first lapped and polished to desired thickness. ITO electrode was sputtered on the surface with 45 W DC power under 30 sccm Ar flow. Then the single crystal stack was cut into the desired square size. With the electroded surface up, the PZN-PT was attached to the glass substrate and placed in brass housing. A co-axial wire was connected to the ITO electrode and brass housing using silver-loaded epoxy (E-solder 3022, Von Roll Isola Inc., USA). After being cured overnight, degassed transparent epoxy was filled into the housing. A plastic plate was covered on top of the housing to make the filled epoxy flat. The TUT was then removed from glass substrate with cured at 45 ℃ for 4 hours. The ITO sputtering process was then conducted on the surface of TUT for ground connection. The PMMA matching layer was lapped and polished to a desired thickness and bonded onto front surface of the TUT using the degassed epoxy. Eternal pressure was applied during the bonding process to make the bonding agent uniform and thin. Fig.3.6 shows the photograph of the PZN-PT based TUT.

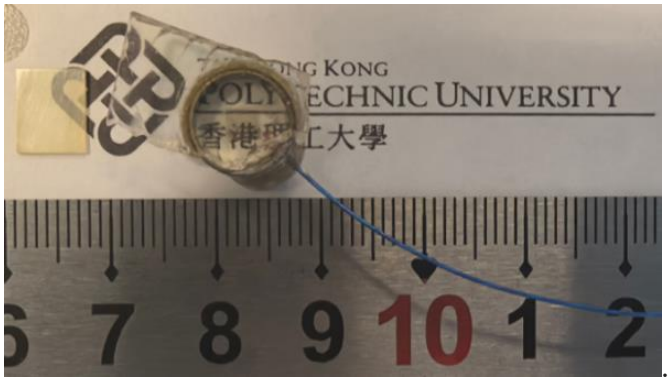

Figure 3.6 DC-poled PZN-PT single crystal and photograph of developed TUT.

To measure characterizations of developed TUT, it was connected to a

pulser/receiver and immersed into distilled water. The distance between TUT and acoustic reflector was set as the near field distance. The echo signal was acquired by a digital oscilloscope with 50 Ω electrical coupling and analyzed by fast Fourier transform (FFT). The f_c and BW were determined. Then the TUT was connected to an impedance analyzer for analysis of the electrical impedance. To indicate sensitivity of the TUT, two-way IL was also measured by connecting the TUT to a function generator with 50 Ω electrical coupling. The optical transmission efficiency of the TUT at 532 nm wavelength was measured by calculating the light intensity before and after transmitting through the TUT.

To evaluate ultrasound imaging performance of the TUT, i*n vivo* B-mode imaging was performed using a fisheye. A fish was immersed in distilled water and TUT was mounted on the step motor with step size of 10 μm, which was triggered by pulser/receiver. The dynamic range was set as 39 dB during the imaging process, and received signal was acquired by a data acquisition card for processing.

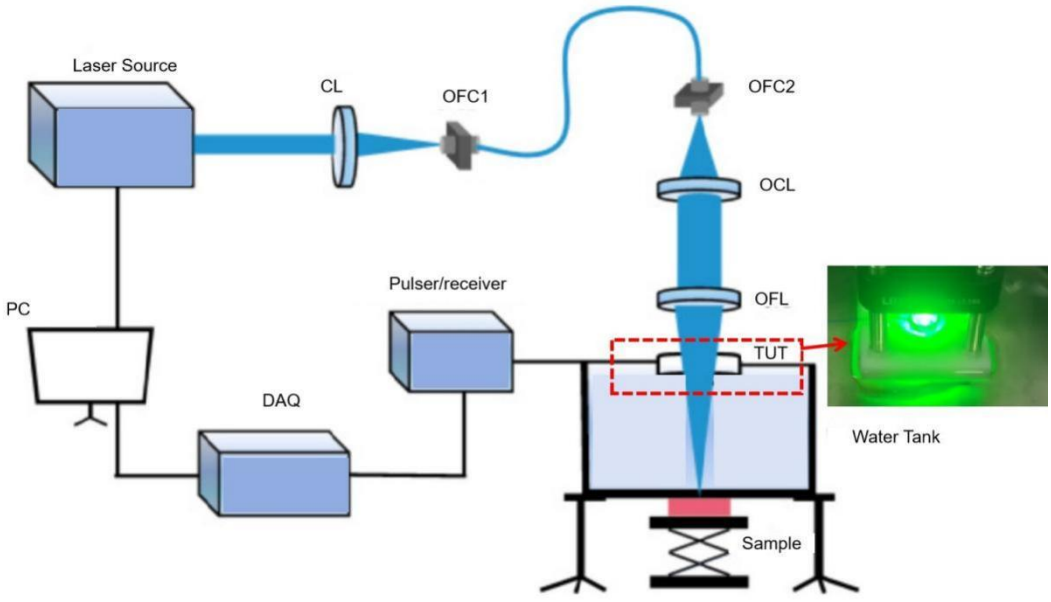

Figure 3.7 Schematic of PAI system based on developed TUT.

The *ex vivo* sample was prepared with biological tissues (chicken breast) and metal, for combined ultrasound/photoacoustic imaging application [78, 79]. The pulsed laser source with 532 nm wavelength was employed for emitting laser beam and coupled into a 105-μm optical fiber, and an optical lens was employed for laser focusing. Detailed PAI system setup was shown in Fig. 3.7. To capture PA image, the chicken breast was placed below a single plastic wrap, and gaps were filled by ultrasound coupling gel. Dual-modality imaging was used by acquiring ultrasound image and PAI of the same target.

3.2.2 TUT Performance

The ferroelectric properties of the PZN-5.5%PT single crystal are shown in Fig. 3.8, where one can see symmetric P-E loops with E_c =0.3 V/μm at 80 V sweeping voltage. Based on the E_c value, the electric field for poling was set as 0.9 V/μm at room temperature.

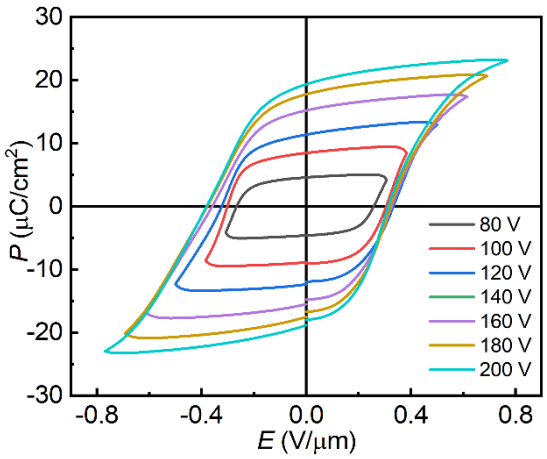

Figure 3.8 P-E hysteresis loop of PZN-5.5%PT single crystal

Piezoelectric and dielectric properties of the PZN-PT crystal are summarized in

Table 3.2. Compared to reported piezoelectric material for TUT applications, the values of d_{33} and g_{33} of the PZN-PT sample in this study are significantly high, therefore, the PZN-PT based TUT should possess great potential to develop TUT for ultrasound/photoacoustic imaging.

Table 3.2 Properties of piezoelectric materials for TUT.

Piezoelectric Material	d_{33} (pC/N)	Free dielectric constant	Clamped dielectric constant	g_{33} (V/Pa)
LN [75]	39	65	39	0.056
DC-poled PMN-PT [20]	1400	5800	621	0.027
AC-poled PMN-PT [75]	2200	7800	850	0.032
DC-poled PZN-PT (this work)	2250	5109	792	0.055

Figs. 3.9 (a) and (b) show simulated pulse-echo response and impedance spectra of the PZN-PT based TUT, while the measured pulse-echo response and impedance spectra are shown in Figs 3.9(c) and (d). The electrical impedance of the fabricated TUT is close to 50 Ω. The 20 MHz of f_c matches well with simulated result, and the measured *BW* is around 50%, which is broader than simulated value. This phenomenon is attributed to the bonding process of matching layer. The sensitivity of TUT can be calculated through *IL* value as -23.9 dB, indicating that the TUT exhibits relatively high sensitivity due to its high d_{33} value.

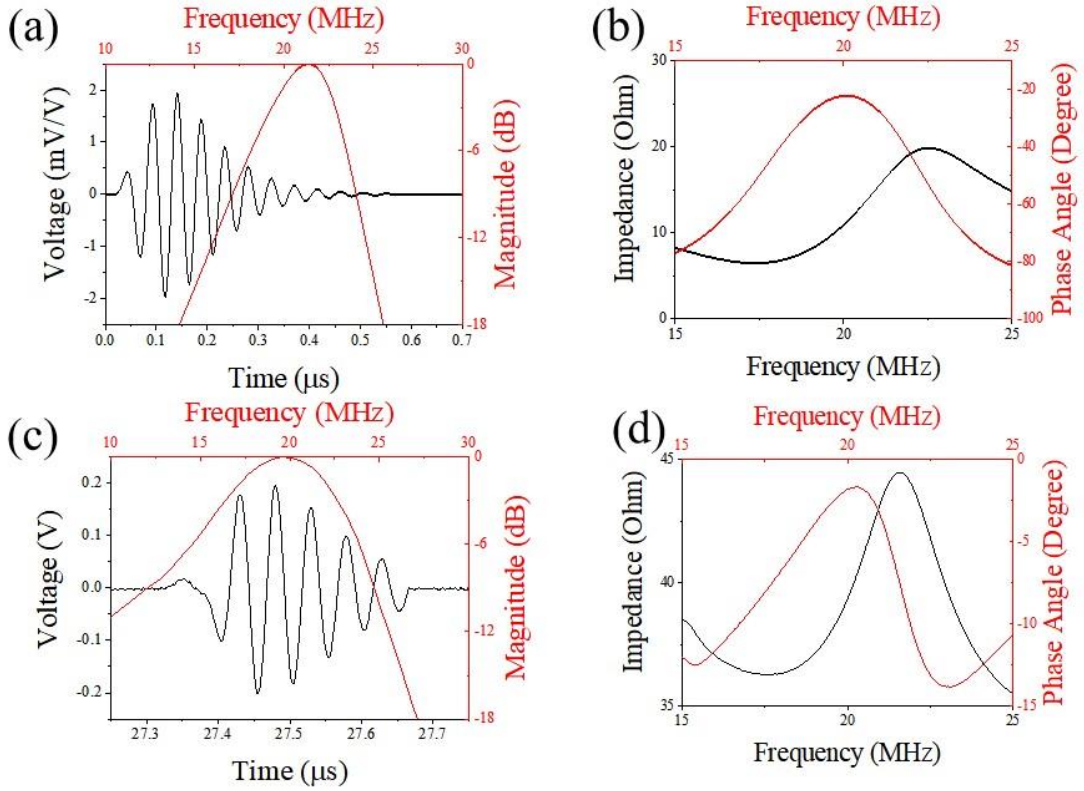

Figure 3.9 Simulated (a) pulse-echo response and impedance spectra (b) of the PZN-PT based TUT, and measured (c) pulse-echo response and (d) impedance of the developed TUT.

Table 3.3 shows characteristics of the PZN-PT based TUT and other reported planar transducers with single polymer-based matching layer. The high sensitivity and broad *BW* under pulse-echo mode demonstrates its capability for practical ultrasound imaging applications.

Table 3.3 Properties of planar transducers with single polymer-based matching layer.

Piezoelectric Material	Aperture Size (mm^2)	f_c (MHz)	*BW*	*IL* (dB)
LN [80]	9 × 9	20	~50%	-28.4
PMN-28%PT [81]	2 × 2	5.09	38.9%	-28.7
PZN-PT (this work)	3 × 3	20	~50%	-23.9

3.2.3 Imaging Performance

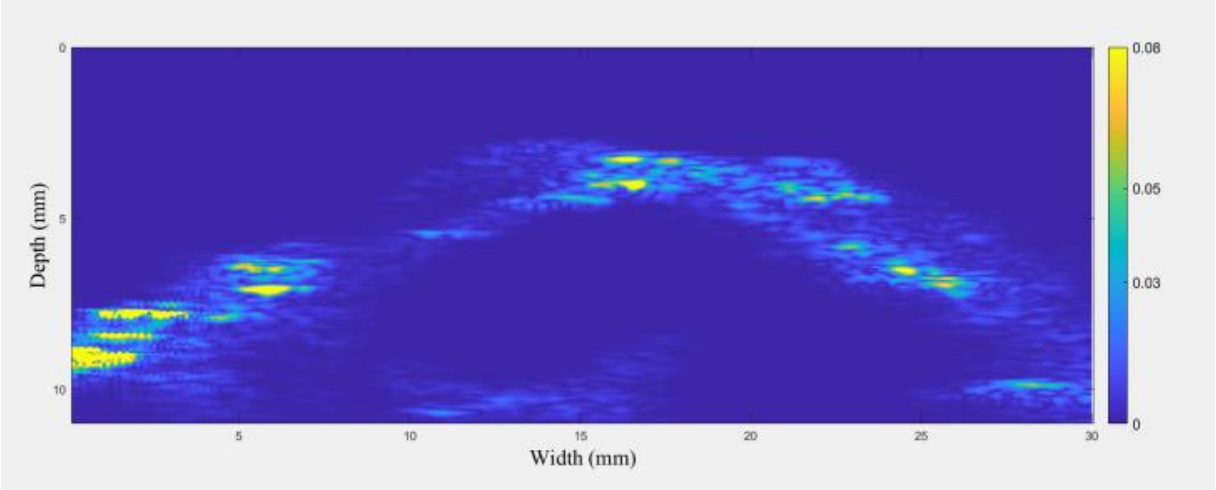

Figure 3.10 B-mode ultrasound image of fish-eye by the PZN-PT based TUT.

Fig. 3.10 shows *in vivo* B-mode ultrasound imaging of a fisheye, where the structure of cornea and iris can be identified, while the signal-to-noise ratio (SNR) of the image at 10 mm depth can achieve 48 dB. With a planar TUT with conventional polymer-based single matching layer, *in vivo* ultrasound imaging can be demonstrated. The transparency of the PZN-PT based TUT can be measured as ~69% at 532 nm wavelength, which is similar to LN-based TUT with the same structure. The transparency is considered satisfactory to allow enough laser energy reaching the target for imaging [78].

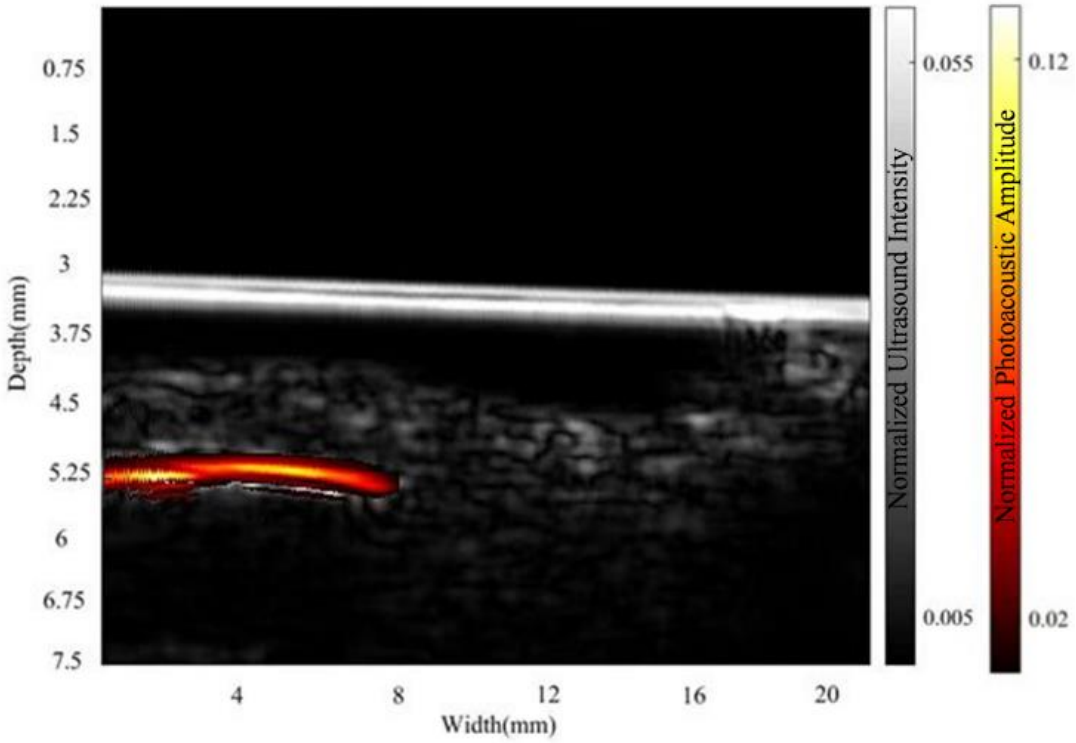

Figure 3.11 Fused dual-modality ultrasound/photoacoustic image of metal wire inserted chicken breast.

Fig. 3.11 shows the fused ultrasound/photoacoustic imaging results of *ex vivo* phantom image. The laser energy keeps in the safety standard during experiment. The plastic wrap, ultrasound coupling gel, and chicken breast tissue could be clearly distinguished, providing structural information. Due to different laser energy absorption coefficients between chicken breast tissue and metal wire, the metal bar can be labeled with 46 dB SNR. We concluded that the g_{33} is the dominant factor of transparent piezoelectric materials for high-performance TUTs. Different from conventional ultrasound transducers for ultrasound imaging application, TUTs for PAI works under receiving-only mode. The TUT for PAI mainly transfers the acoustic energy to electrical energy, where the g_{33} value should be considered as the key parameter. The high SNR here is contributed by the high g33 value of the PZN-PT single crystal.

In summary, a PZN-5.5%PT based TUT has been developed with the piezoelectric single crystal poled using conventional DC electric field. Reported TUT with similar structure was always limited for ultrasound imaging due to relatively low sensitivity. In aspect of active layer of TUT, the PZN-PT single crystal possesses excellent piezoelectric properties for dual-modality ultrasound/photoacoustic image. Based on single polymer-based acoustic matching layer, a 20 MHz TUT with ~50 *BW* and -23.9 dB *IL* was successfully developed. *In vivo* ultrasound B-mode image was successfully demonstrated using TUT. With 68% transparency at 532 nm wavelength, dual-modality *ex vivo* image was also demonstrated. This work highlights the potential of DC-poled relaxor ferroelectric PZN-PT single crystal for TUT application, which is considered as a substitution for LN single crystal and AC-poled single crystals.

3.3 Eu-PMN-PT Ceramic-based TUT

Compared to relaxor-ferroelectric single crystal, piezoelectric ceramic is easy to be synthesized with low cost and can be doped with other elements to achieve different properties. In recent years, much effort has been paid to investigate highly transparent piezoelectric ceramics including (K,Na)NbO_3 (KNN), $BaTiO_3$ (BT), and PMN-PT based ceramics. Although KNN-based ceramics show light transmission efficiency as high as 70%, their d_{33} property is always limited to smaller than 200 pC/N. The poor piezoelectric property limits their practical applications for ultrasound transducers. With the hot-pressing technology during sintering, the BT ceramics can achieve high d_{33} as 420 pC/N. However, the light transmission efficiency is degraded to only 40% at

900 nm wavelength. Recently, the 2.5%Eu doped PMN-28PT transparent ceramic was found to exhibit both high piezoelectric properties and transparency, with d_{33} as 1400 pC/N and light transmission efficiency as 68% at 900 nm. Its excellent performance surpasses other transparent piezoelectric ceramics, indicating great potential for the TUT application.

In this part, a 2% (in mole) Eu^{3+} doped PMN-28PT (abbreviated as 2%Eu-PMN-28PT) transparent ceramics (transparency as 68% at 900nm) with piezoelectric coefficient d_{33} up to 1500 pC/N was prepared. Firstly, a high-sensitivity TUT with f_c of 16 MHz was fabricated. To maintain sensitivity, Parylene was employed here as the single acoustic matching layer. The capability of both PA and US imaging modalities was validated, where successful dual-modality images of the phantoms were acquired. To evaluate the sensitivity of the TUT by signal-to-noise ratio (SNR), the image depth was also studied. Additionally, a high-frequency TUT with the same structure was developed for *in vivo* photoacoustic imaging of subcutaneous micro-vasculature in a mouse ear has.

3.3.1 Characteristics of the PMN-28PT Ceramic

The 2%Eu-PMN-28PT ceramic was prepared using a two-step sintering process, including oxygen sintering and hot-press sintering. The high-purity Nb_2O_5 (99.99%, Aladdin), MgO (99.99%, Aladdin), PbO (99.99%, Aladdin), TiO_2 (99.99%, Aladdin), and Eu_2O_3 (99.99%, Aladdin) powders were used as raw materials. The sintering

procedures are not the key point in this study and will not be illustrated in detail here, but this procedure can refer to previous studies. To test electrical properties of the Eu-PMN-PT ceramic, the ceramic cylinder was cut into 1.0 mm-thick samples, and conventional metal electrode was sputter deposited onto the sample surfaces.

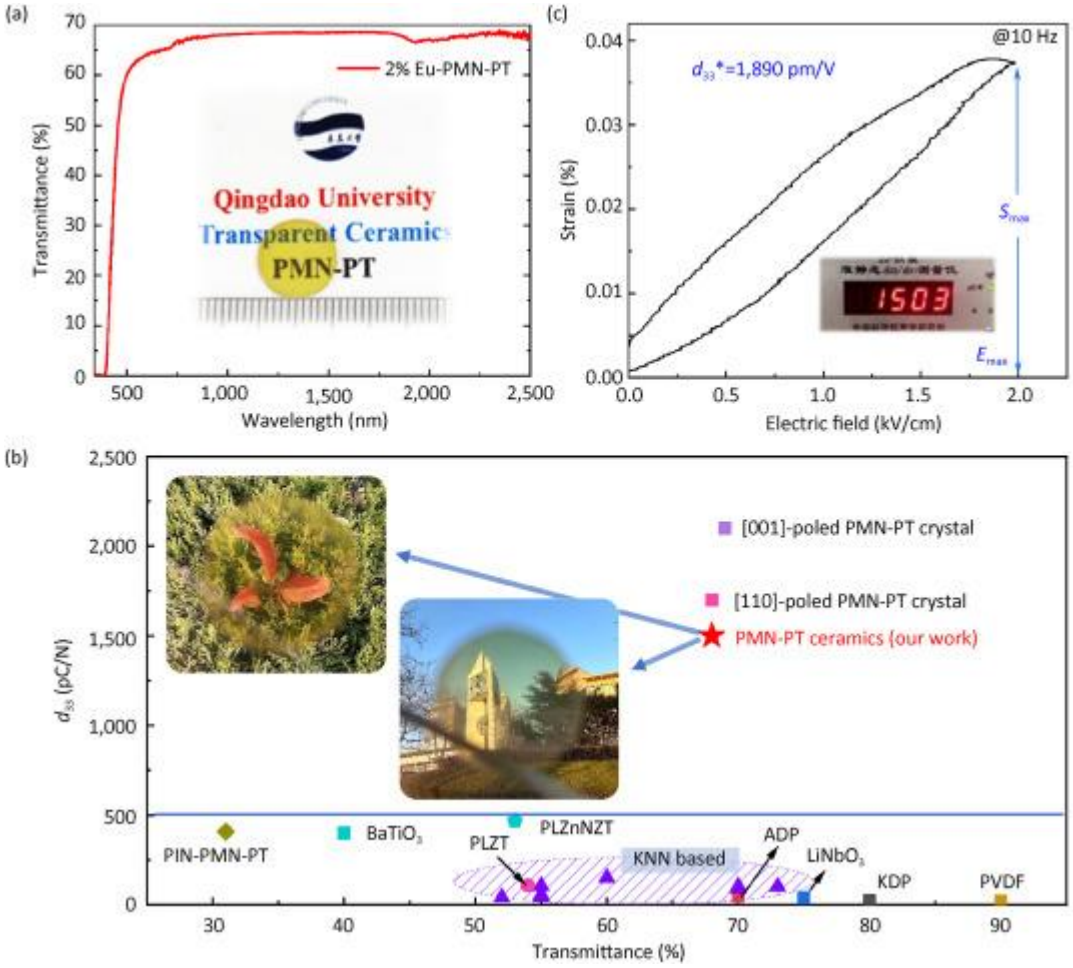

Figure 3.12 (a) Photograph of a transparent Eu-PMN-PT ceramic and optical transmittance at various wavelengths; **(b)** Comparison of the proposed ceramic to other related piezoelectric materials, including optical properties and piezoelectric properties; **(c)** The measured d_{33} value and electrical field-induced strain of the ceramic.

Poling was conducted by applying an electric field (9 kV/cm) to the sample which was immersed into silicone oil for 20 minutes at room temperature. The d_{33} was measured with the d_{33} meter (ZJ-4AN, Institute of acoustic, Chinese Academic Society, China), and a ferroelectric testing system (Precision LC, Radiant Technologies, USA)

was employed to obtain the P-E loops and strain (S-E) curves. The optical transmitting coefficient was measured with a double-side polished ceramic. The scanning electron microscope (JSM-6390LV, JEOL, Tokyo, Japan) was also conducted to observe the micro-structure. The k_t and dielectric constants were measured by an impedance analyzer.

As shown in Fig. 3.12(a), the 2%Eu-PMN-PT ceramic shows transparency at the wavelength over 400 nm, and the light transmission efficiency was measured over 68% in these regions. Fig. 3.12(c) shows the great d_{33} that measured by the d_{33} meter, as high as 1500 pC/N. Comparison with other transparent materials is shown in Fig. 3.12(b), where one can see that the transparency and the d_{33} of the Eu-PMN-PT transparent ceramics show great advantages to other ceramics, even can be comparable to single crystals.

The f_r and f_a of a thick ceramic wafer were measured as shown in Fig. 3.13(a). The energy conversion efficiency k_t is calculated as 0.65. The P-E loop is shown in Fig. 3.13 (b), where the E_c is ~3V/μm, indicating the poling electrical field for further TUT application.

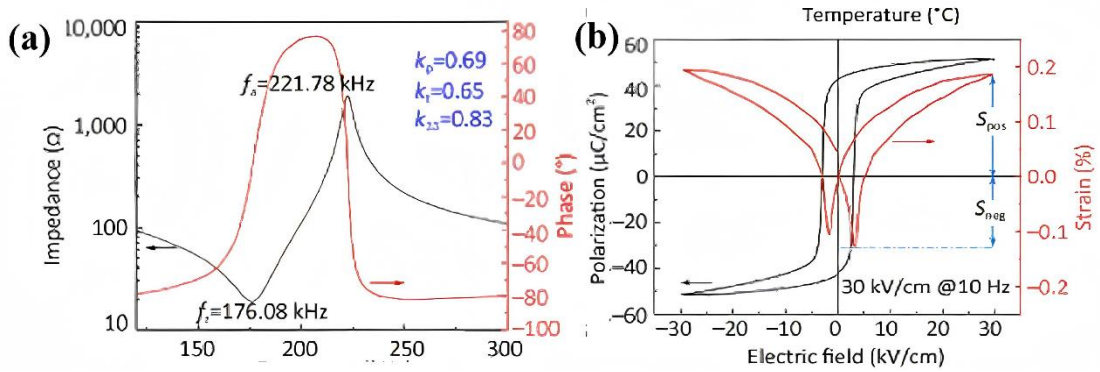

Figure 3.13 (a) Measured impedance spectra of a Eu-PMN-PT ceramic plate, **(b)** Measured P-E loop and electrical field induced strain curve.

3.3.2 Performance of TUT

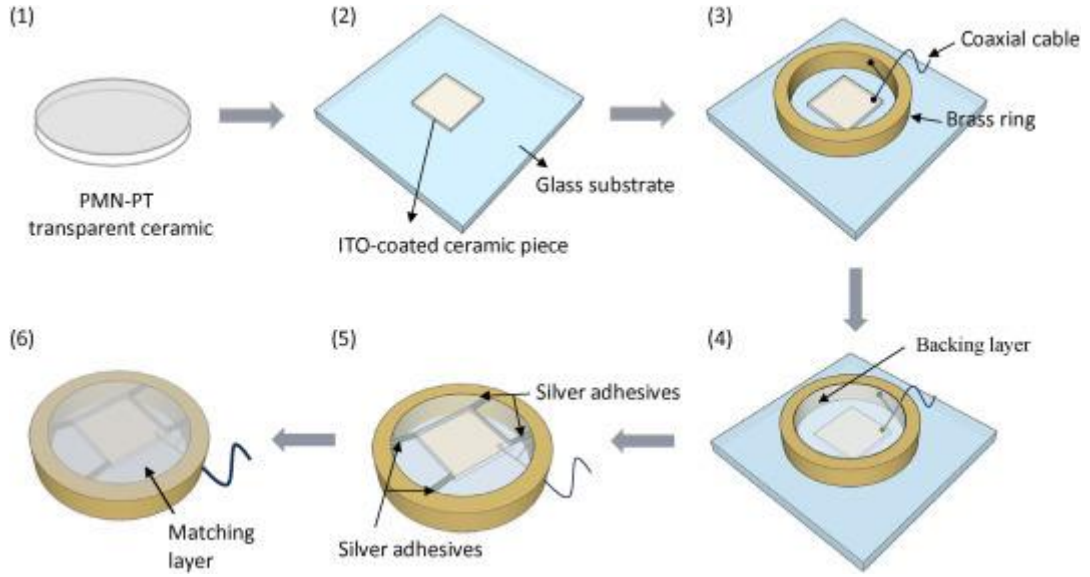

Figure 3.14 Fabrication procedures of TUT.

Fig. 3.14 shows the manufacturing steps of TUT:

(1) A transparent Eu doped PMN-PT ceramic with a diameter of 10 mm and thickness of 150 μm and 80 μm was prepared.

(2) 280 nm transparent ITO electrode was sputtered on both surfaces of the PMN-PT ceramic. Then the ceramic was cut into 4 mm×4 mm square pieces by dicing saw and placed on a glass substrate by double sided tape.

(3) A brass housing was placed around the ceramic, and make sure the square ceramic piece is at the center of the brass ring. Then, connect the ITO layer and the outer housing by a con-axial cable with conductive silver-loaded epoxy.

(4) Filling transparent epoxy (EPO-TEK 301) as a backing layer into the brass ring. The ceramic wafer and the brass housing can be formed as a whole part after epoxy curing.

(5) Remove the TUT from the glass substrate. In order to achieve ground connection,

the ITO electrode on the front surface of the TUT was connected with the brass housing using conductive silver loaded epoxy.

(6) Finally, Parylene films with a thickness of 34 μm and 20 μm were vapor-deposited on the front surface of TUT for both acoustic matching and protective layer.

The measured pulse-echo response was used to determine f_c and BW of the TUT which was connected to the commercial pulser/receive (5073PR, Olympus, Japan) under P/R model. The pulse repetition frequency was set as 1 kHz, and no gain was used, while the echo signal received was analyzed by FFT. Then, the electrical impedance and k_{eff} of TUT was tested by connecting to an impedance analyzer (4294A, Agilent Tech, Santa Clara, CA, USA).

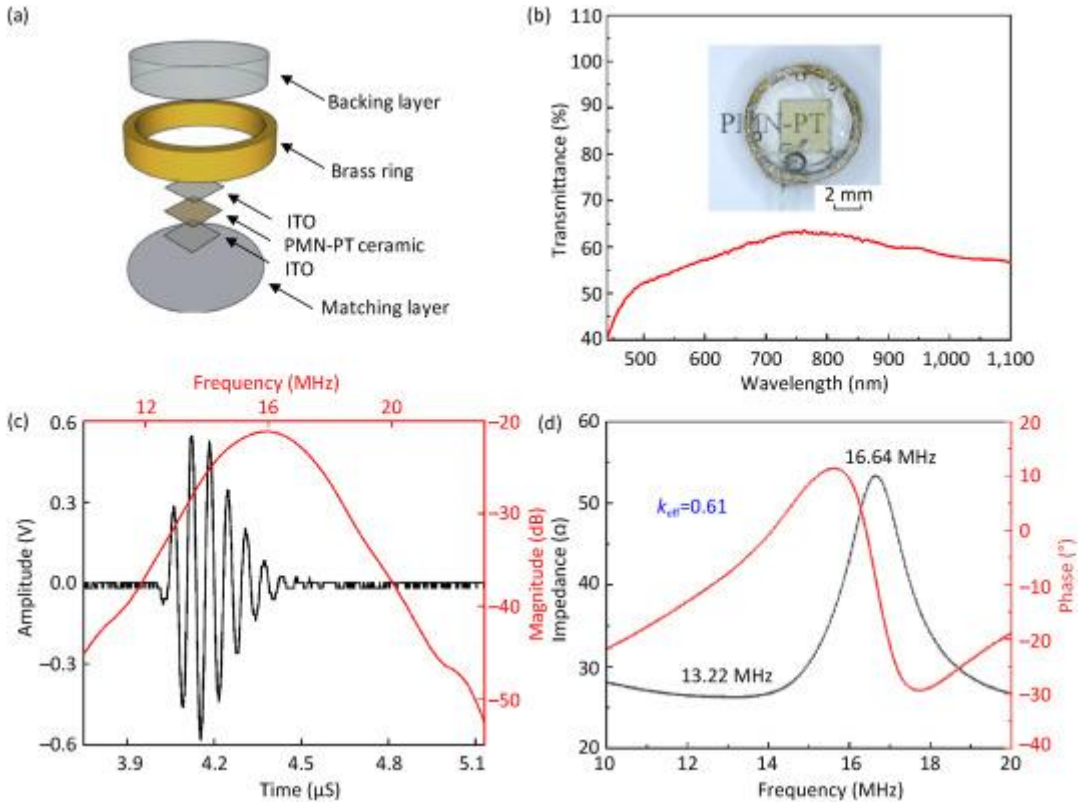

Figure 3.15 (a) Schematic diagram of the proposed TUT. **(b)** Photograph and optical transmittance of the TUT. Measured **(c)** pulse-echo response and **(d)** impedance spectra of the TUT.

The structure of TUT based on Eu-PMN-PT transparent ceramic is shown in Fig.

3.15(a), and a photograph of the proposed TUT is shown in Fig. 3.15(b). The light transmittance of the TUT for various wavelengths were also measured, showing >50% transmittance for all wavelengths. For the transmittance at 1064 nm wavelength, the corresponding transmittance is obtained as ~57%, which is considered high enough for TUT-based PAI applications. The Eu-PMN-PT has a relatively high longitudinal acoustic velocity due to the hot-pressing ceramic fabrication process. A 16 MHz TUT was designed and fabricated using 150 μm-thick ceramic. The measured pulse-echo response of the TUT is shown in Fig. 3.15(c), and corresponding impedance spectra can be obtained as shown in Fig. 3.15(d). The BW is measured as ~30%, while the insertion loss is measured as ~25 dB. The k_{eff} is calculated as 0.61, which is as high as the LN-based TUT with 50% *BW*. The high k_t value of the ceramic contributes to the advantage, indicating the great potential of transparent PMN-PT ceramics for TUT applications.

3.3.3 Imaging Performance

The photoacoustic/ultrasound imaging system setup is shown in Fig. 3.16. During PAI process, the pulsed laser beam (EKSPLA, NT242, 1064 nm, 1 kHz) emitted from the laser source is first coupled into an optical fiber (core diameter: 105 μm) through a coupled lens, and then the laser beam is focused by optical focusing lens. The laser beam can pass through the TUT and illuminate the imaging target directly.

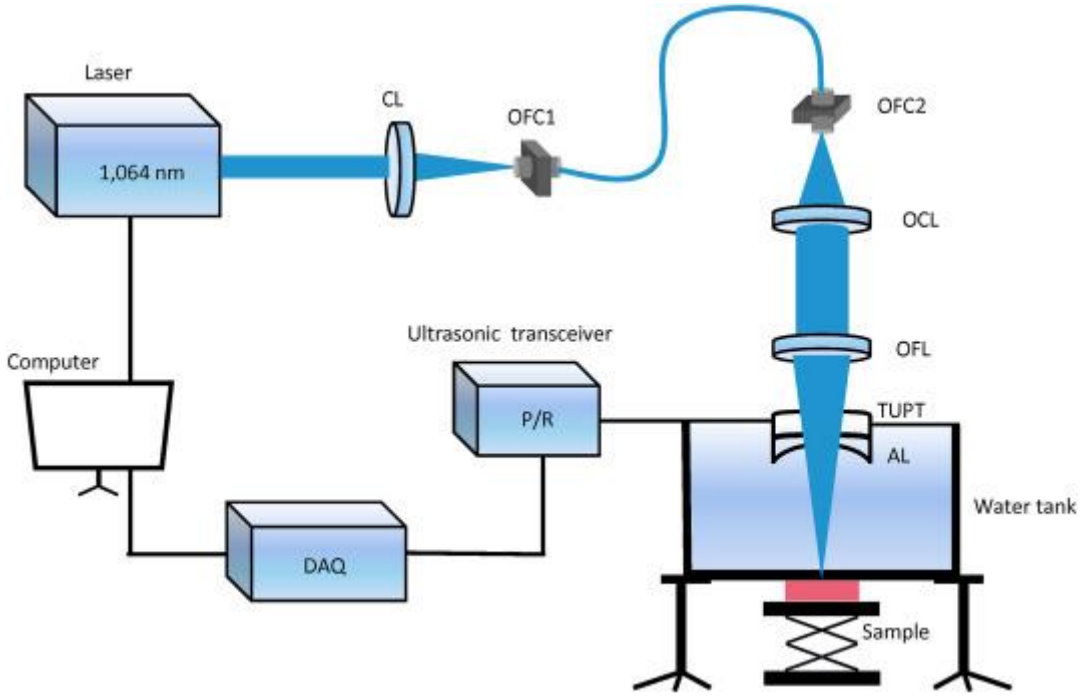

Figure 3.16 A PA/US dual-modal imaging system integrated with TUPT. CL, coupled lens; OFC, Optical fiber connector; OCL, Optical collimating lens; OFL, Optical focusing lens; AL, Acoustic lens

The generated PA signal is detected by the TUT and then is amplified by a commercial pulser/receiver (5073PR, Olympus, Tokyo, Japan). The signals are then acquired by a data acquisition card (ATS9371, Alazar Tech, Pointe-Claire, QC, Canada). The laser focusing parts and TUT are mounted on a custom-made holder which is connected to a two-dimensional linear stage for laser scanning and imaging purposes.

The lateral resolution of the photoacoustic/ultrasound imaging system was measured by scanning a sharp edge. A piece of black tape was bonded on a quartz plate, where the edge between black tape and quartz was considered sharp enough for resolution measurement. The TUT was scanned over the range at the edge, which was driven by the linear stage with 50 μm step size. With the acquired image, the detailed procedure to calculate the spatial resolution is as follows.

1. The envelop of the ultrasound/photoacoustic signal was obtained by the Hilbert transform.

2. The corresponding peaks of the envelopes were normalized.

3. The edge spread function (ESF) was obtained by fitting the curve with the cumulative distribution function (CDF).

4. The ESF curve was differentiated to obtain the curve of line spread function (LSF); and the full width at half maximum (FWHM) of the LSF curve can be calculated as the lateral resolution.

The measured lateral resolutions for ultrasound and PAI are 320 μm and 225 μm, respectively (see Figs. 3.17(a) and (b)). The PAI lateral resolution is relatively poor, because the focused laser spot may be scattered after transmission through the acoustic lens; while for lateral resolution of ultrasound imaging, it agrees well with the theoretical value.

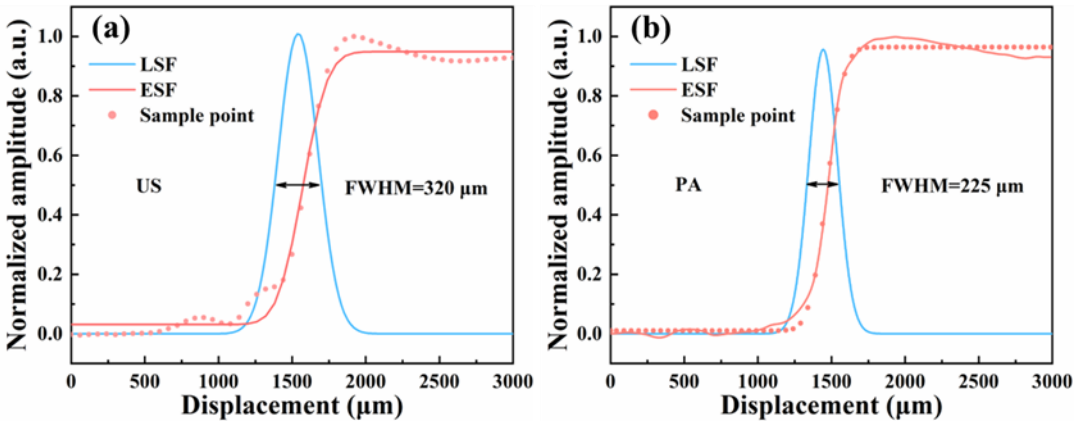

Figure 3.17 (a) Ultrasound and (b) PAI lateral resolution of the Eu-PMN-PT based TUT.

To validate the ultrasound/PAI capability of the TUT, a simple phantom was prepared based on different concepts of ultrasound imaging and PAI. The phantom was consisted of a metal ring with the shape of "O", and a shape of "K" formed by the black tape (Fig. 3.18(a)). For ultrasound imaging, the signal reflection coefficient is mainly dependent on the differences of acoustic impedance, while the PAI signal generation

relies on the absorption of laser beam. Since metal phantoms possess larger acoustic impedance (> 35 MRayl) compared to the black tape (~ 3 MRayl), the ultrasound imaging of these two parts presents high contrast, as shown in Fig. 3.18(b). While for PAI, the black tape absorbs the laser energy and generate photoacoustic signals more effectively, therefore, as shown in Fig. 3.18(c), the "K" shows stronger signal intensity compared to metal. Fig. 3.18(d) shows the fused ultrasound/PAI dual-modality image, demonstrating the dual-modality image with structural and functional information of the two letters. The phantom experiments illustrate that the TUT has potential for biomedical imaging applications

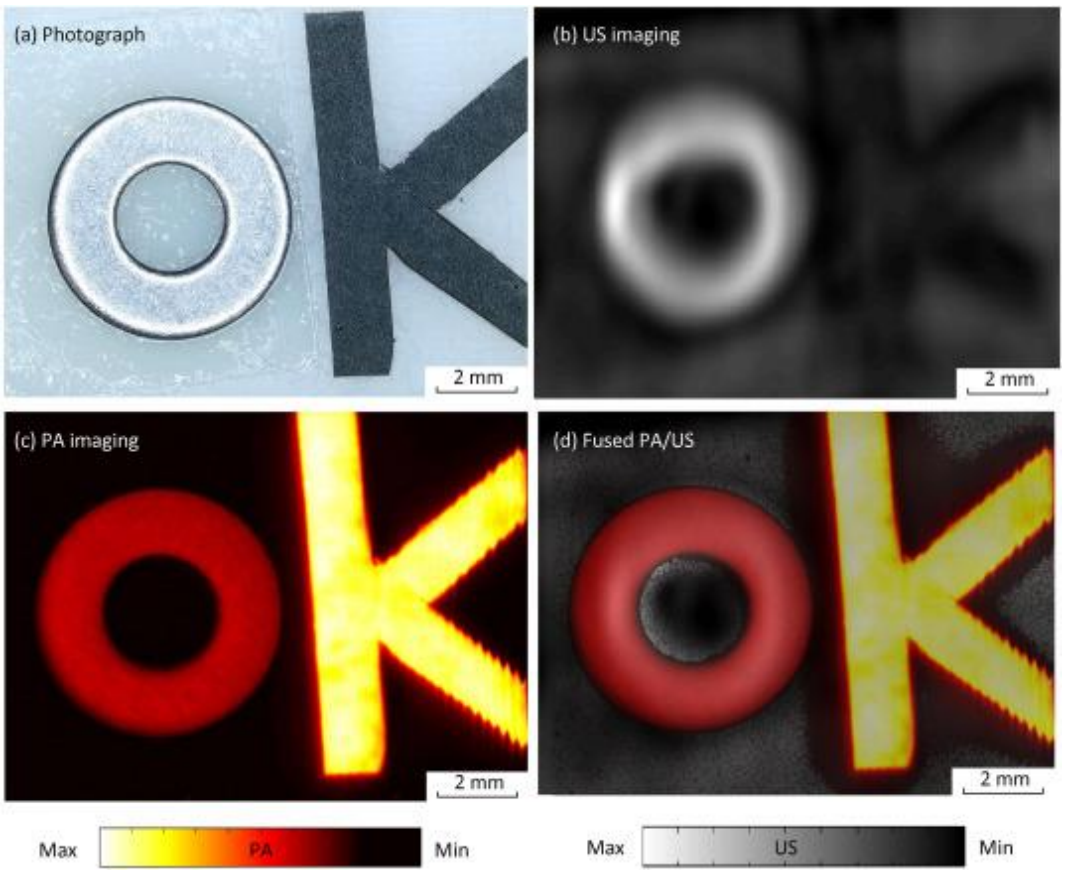

Figure 3.18 (a) Photograph of the phantom**, (b)** Ultrasound B-scan image of the phantom, **(c)** PAI of the phantom, and **(d)** Fused dual-modality image of the phantom.

Ultrasound/photoacoustic imaging capability was then evaluated by *ex vivo*

experiments. Biological samples were prepared with chicken breast meat, into which a metal rod was inserted, as shown in Fig 3.19(a). For ultrasound imaging, there is large differences between acoustics impedances of chicken breast and metal rod. Thus, the structure of the phantom can be clearly imaged. In aspect of PAI, the metal bar absorbs the laser energy while the chicken breast meat almost absorbs none. The 1064 nm wavelength laser was used with the energy of 45 μJ, which is in the safety range. To study the image depth of the TUT, the thickness of chicken breast meat samples were selected in ranges from 1.5 mm to 7.5 mm. The fused ultrasound/photoacoustic imaging of the *ex vivo* samples were shown in Fig. 3.19(c).

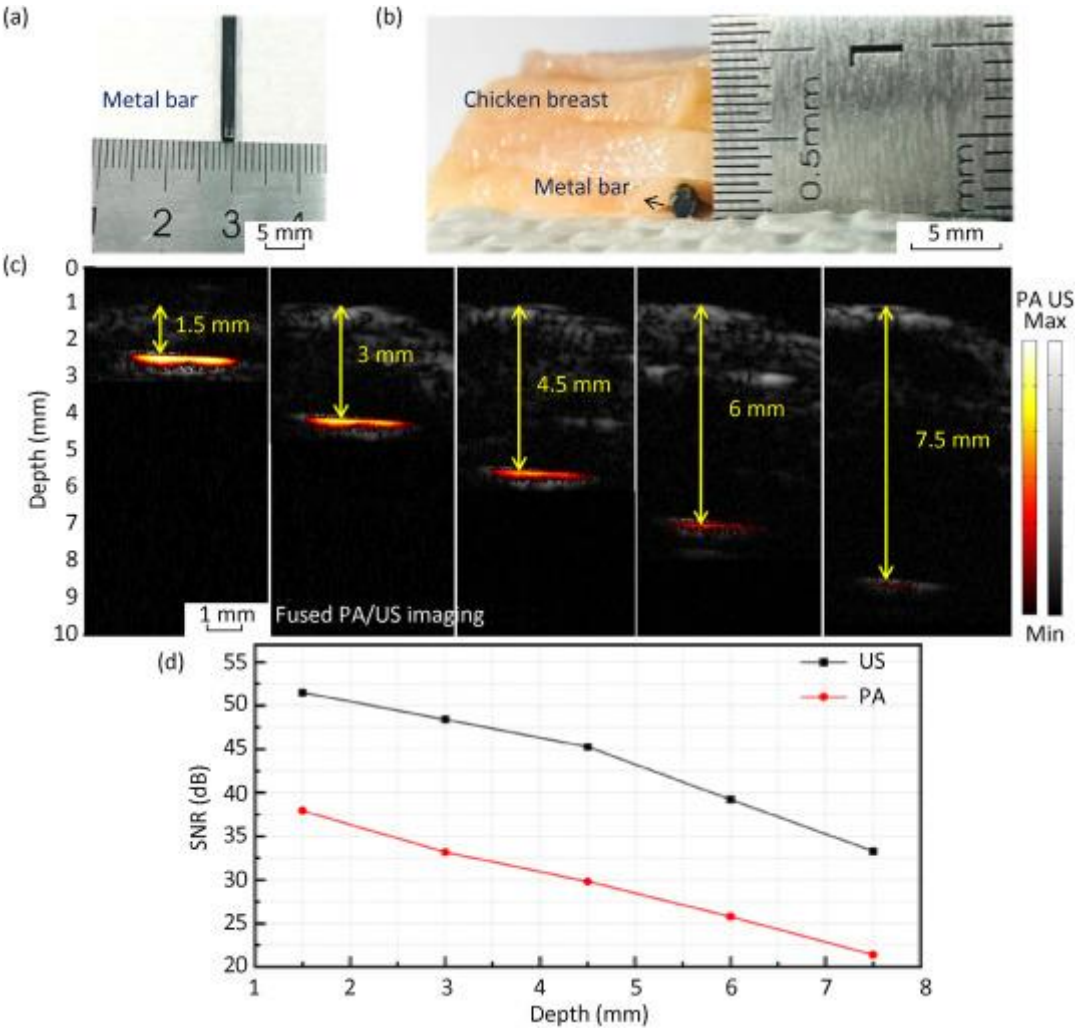

Figure 3.19 (a) Photograph of the metal rod as the detection target. **(b)** Photograph of the *ex vivo* sample

consisting of chicken breast meat and metal rod, **(c)** The fused ultrasound/photoacoustic images with different depths, and **(d)** SNRs of dual-modality imaging at different depths.

The SNRs at different depths were analyzed at the positions of the metal rod. The SNR of ultrasound and photoacoustic images decreased simultaneously with an increase in detection depth. For the image that detected at superior position (1.5 mm), the SNR of ultrasound imaging could achieve 53 dB, while the SNR of PAI is calculated as 38 dB. Even at the depth of 7.5 mm, the SNR could be as high as 33 dB and 21 dB for ultrasound and PAI respectively. Comparisons with other TUTs are shown in Table 3.4. Although the f_c and laser energy are different, the high SNR of the Eu-PMN-PT ceramic-based TUT in deep tissues is commendable.

Table 3.4. Comparison of PA imaging depth and SNR with other ultrasonic transducers.

Ultrasonic transducers		f_c (MHz)	Wavelength (nm)	Light energy (μJ)	Imaging depth (mm)	SNR (dB)	Ref
Opaque	Commercial UT	50	559 – 576	NA	4.6	2.5	[82]
					7.6	1.4	
Transparent	PVDF film	36	532	35	1	36.5	[53]
					3	22	
	LiNbO3 crystal	13	532	19	NA	38	[27]
	PMN-PT crystal	8	650	NA	0	33	[41]
					3	27	
	Eu-PMN-PT ceramic	16	1064	45	1.5	38	**This work**
					7.5	21	

To validate the *in vivo* imaging capability of the proposed TUT, the sub-cutaneous microvasculature of a mouse ear was imaged. To obtain high-resolution PAI, a high-frequency TUT was developed without acoustic lens. The f_c was measured to be 28 MHz, and *BW* was measured to be ~30% as shown in Fig 3.20(a), and the impedance

was measured as Fig. 3.20(b). The 532 nm wavelength laser is employed here, which is suitable for vascular PAI.

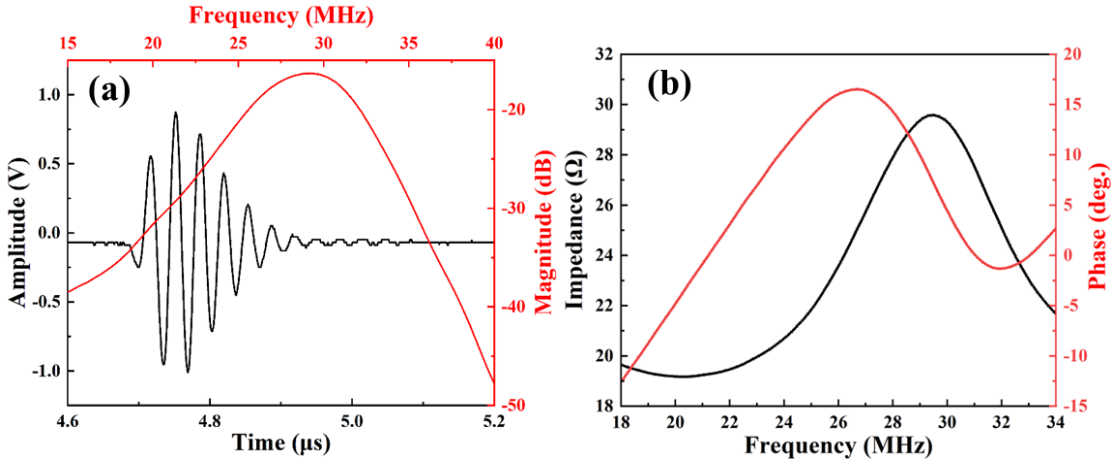

Figure 3.20 (a) Measured pulse-echo response of the high-frequency Eu doped PMN-PT ceramic. **(b)** The measured impedance spectra.

A 9 μm-diameter optical fiber was used for achieving high lateral resolution of PAI. The *in vivo* PAI of the microvascular network of the mouse ear is shown in Figure 3.21(a), and the corresponding scanning area is labeled. Except for the three thick vessels, some capillaries can also be detected (Fig. 3.21(b)).

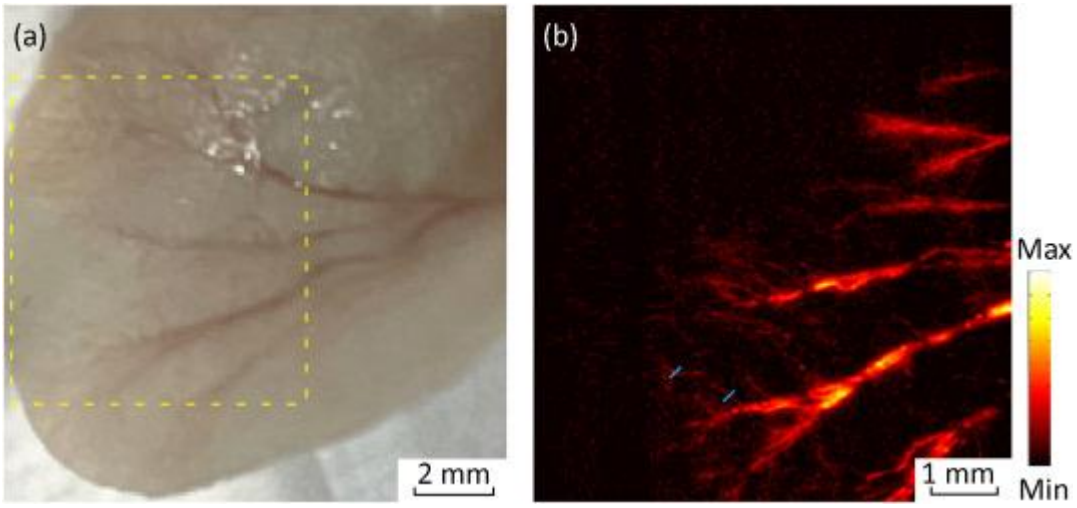

Figure 3.21 (a) Photograph of the imaging area. **(b)** In vivo PAI of the microvascular network of the mouse ear.

In this part, transparent Eu-doped PMN-PT ceramic was used for TUT fabrication.

The advanced piezoelectric ceramic possesses high d_{33} as 1500 pC/N, and high k_t as 0.62. Attributing to the high ε_s of the ceramic, the proposed TUT can have a much smaller aperture size (3×3 mm^2) than LN-based TUTs with similar f_c, The TUT has an improved *IL* value of -25 dB. With single parylene matching layer, the *ex vivo* ultrasound/photoacoustic dual-modality imaging was successfully demonstrated. The superior SNR can reach more than 40 dB. In addition, a high-frequency TUT was developed for *in vivo* imaging of the mouse ear, where vessels can be clearly seen. Overall, this study investigates the capability of transparent piezoelectric ceramics for TUT applications.

3.4 Sm-PMN-PT Ceramic based TUT

TUT is regarded as a potential instrument for PAI in endoscopy applications, however, the catheter's dimensions impose constraints on the feasibility of implementing a co-axial design. The employment of TUT facilitates the streamlining of light components. Fig 3.22 shows PAI endoscopy design based on TUT.

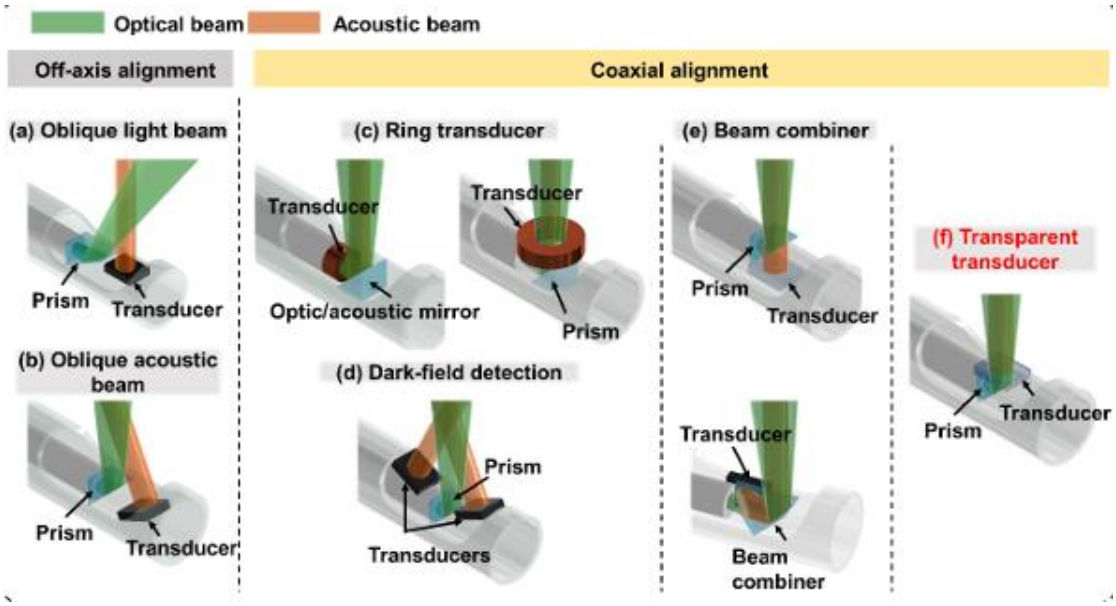

Figure 3.22. Schematic diagram of different photoacoustic endoscopy design **(a)(b)** Off-axis alignment of laser beam and ultrasound detection. **(c)** Ring shaped ultrasound transducer based co-axial design. **(d)** Dark-field detection based co-axial design. **(e)** Beam combiner based co-axial design. **(f)** TUT based coaxial design [43].

Presently, the development of TUTs is mainly based on LN single crystal, PVDF based polymer, relaxor-ferroelectric single crystals, and the Eu doped PMN-PT ceramic. However, limited by the relatively small ε_s (<1000), the aperture sizes of reported transducers are not small enough for endoscopy application.

In recent years, the samarium (Sm)-doped PMN-PT (Sm-PMN-PT) ceramic was reported that possessing d_{33} of 1100 pC/N and free dielectric constant (ε_r) up to 13000 [83]. Further, co-doping technology was investigated by Sm and praseodymium (Pr) elements, improving d_{33} to over 1500 pC/N or ε_r to over 19000 [84]. This kind of advanced piezoelectric ceramic is considered suitable for miniature ultrasound transducer application. A needle transducer with only 0.4×0.4 mm^2 aperture size was developed. With successful electrical matching, the needle transducer achieved high sensitivity, and high-quality *in vivo* ultrasound imaging [85]. Also, with a small aperture size of the transducer measuring 0.5×0.5 mm^2, this kind of piezoelectric ceramic was demonstrated for *in vivo* intravascular ultrasound imaging [86]. Piezoelectric composite transducers based on Sm-PMN-PT also show the advantage of minimization, where the miniature transducer worked with optimized electrical impedance to show improved image qualities [87]. Further, the ceramic with high ε_s was investigated for ultrasound therapy application with a two-dimensional array [88].

Recently, rare-earth element doped PMN-PT ceramics can be made transparent by hot-pressing sintering, and it is believed that Sm-PMN-PT can achieve similar

properties. In this work, the 2.5 % Sm-doped 0.72PMN-0.28PT transparent ceramic was studied for the miniature TUT for the PAI endoscopy application. The Sm-PMN-PT owns high optical transmittance as 69%. The piezoelectric properties are also great with d_{33} of 1460 pC/N, k_t of 0.63 and ε_r over 12000; with this ceramic, a 18.5 MHz TUT was designed and fabricated, where transparent epoxy was employed as the backing layer and single Parylene C was deposited as the acoustic matching layer to ensure sensitivity. Ultrasound/PAI dual-modality imaging was performed to validate the capability of the TUT for practical biomedical engineering applications.

3.4.1 Characteristics of Ceramic Material

Sm-doped 0.72PMN-0.28PT ceramics were prepared by a two-step sintering method. The raw materials were high purity MgO (Aladdin, Shanghai, China, 99.9 %), Nb_2O_5 (Aladdin, Shanghai, China, 99.99 %), PbO (Aladdin, Shanghai, China, 99.9 %), TiO_2 (Aladdin, Shanghai, China, 99.99 %), and Sm_2O_3 (Aladdin, Shanghai, China, 99.99 %). Detailed synthesis may refer to previous material-related work.

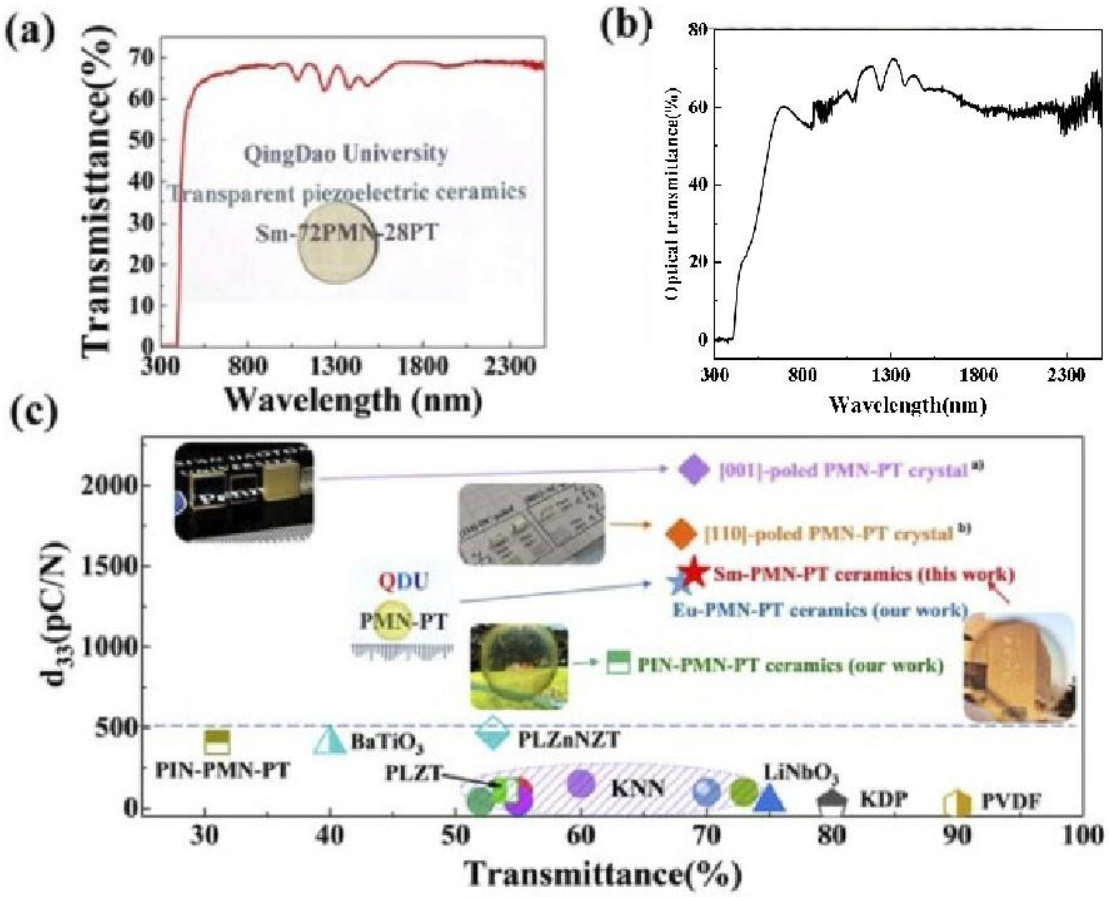

Figure 3.23 (a) Transparency of Sm-doped 0.72PMN-0.28PT ceramics. **(b)** Distant landscape through 0.72PMN-0.28PT transparent ceramics. **(c)** Comparison of optical properties and piezoelectric properties of different transparent piezoelectric materials,

Piezoelectric properties for transducer fabrication were measured. The d_{33} was measured by the d_{33} meter (ZJ-4AN, Institute of Acoustic, Chinese Academic Society, China). The optical transmittance of a Sm-PMN-PT ceramic with a thickness of 300 μm is shown in Fig 3.23(a). It is found that the transmittance is over 60% for all wavelength, indicating high transparency. The optical transmittance of an ITO-coated transparent ceramic was also measured as shown in Fig 3.23(b). There is no transparency loss at 1064 nm wavelength, indicating the great optical property of the sputtered ITO electrode. It should be noted that this kind of ceramic is almost opaque below 400 nm, which is limited by the micro-structure of the material.

The comparison of the Sm-PMN-PT ceramic with other transparent piezoelectric

materials is shown in Fig 3.23(c). One can see that, among all kinds of ceramics, the Sm-PMN-PT ceramic owns the highest d_{33} value over 1400 pC/N. In aspect of transparency, although the Sm-PMN-PT ceramic is lower than many materials, the light transmittance is sufficient for TUT applications. Considering the balance between these two properties, the Sm-PMN-PT ceramic has great potential for PAI as the active layer of the TUT.

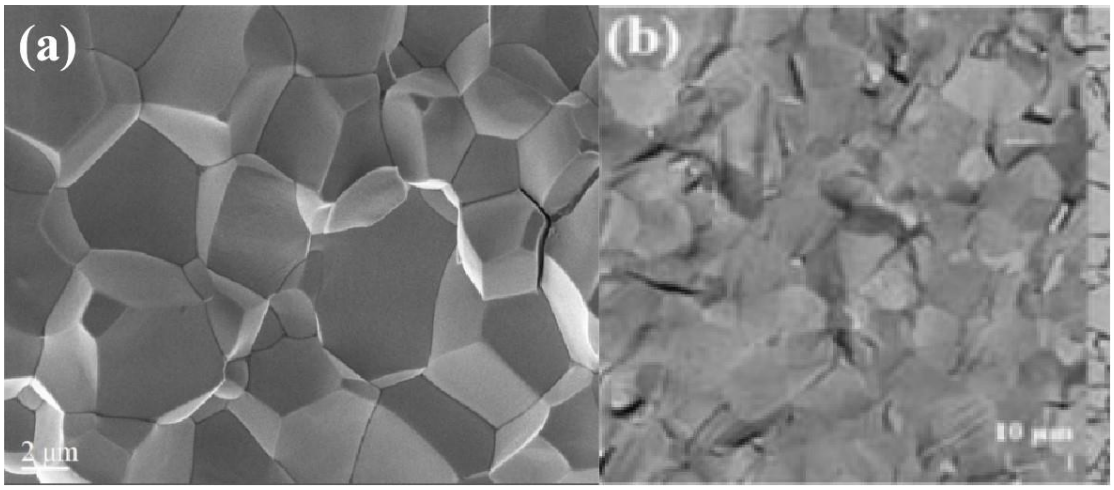

Figure 3.24. SEM images of **(a)** conventionally synthesized Sm-PMN-PT ceramic [89], and **(b)** the hot pressed transparent Sm-PMN-PT ceramic in this study.

The microstructure of the transparent Sm-PMN-PT ceramic was studied by scanning electron microscopy (SEM) (JSM-6390LV, JEOL, Tokyo, Japan). Figs. 3.24(a) and (b) show the fracture surfaces of Sm-PMN-PT ceramics prepared with different sintering methods. The grain boundaries of the transparent ceramic are small and tightly bound, resulting in stronger vibrations and higher optical transmittance than those prepared by conventional methods.

P-E loop of the ceramic was measured by a ferroelectric test system with 1 Hz frequency. The k_t and ε_r were also measured by the same methods using an impedance analyzer. Optical transmittance at different wavelengths was measured by a

spectrophotometer (PE Lambda 750, PerkinElmer, America).

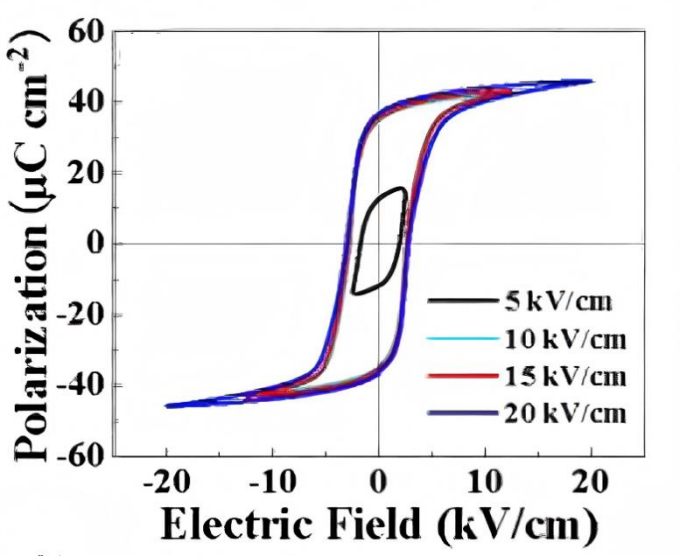

Figure 3.25 P-E loop of the transparent Sm-PMN-PT ceramic

The ferroelectric property of the Sm-PMN-PT ceramic can be demonstrated by its P-E loops, where the regular rectangular shape and the smooth curve suggest the great ferroelectricity of the ceramic. The E_c is 3.0 V/μm, suggesting that the poling electrical field should be larger than 9 V/μm at room temperature (Fig. 3.25).

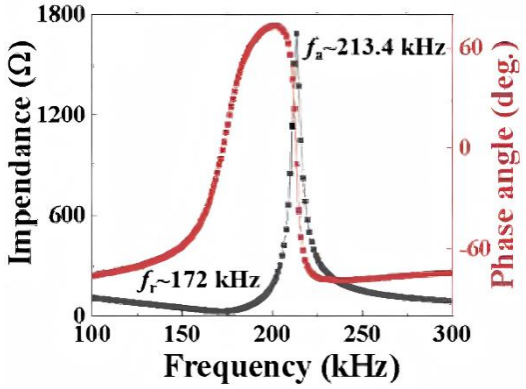

Figure 3.26 Measured impedance spectra and phase angles of the thick transparent Sm-PMN-PT ceramic.

Fig. 3.26 shows the impedance spectra of a thick transparent Sm-PMN-PT ceramic plate, where f_r and f_a are 172.0 kHz and 213.4 kHz, respectively. Correspondingly, the k_t is calculated to be 0.63. The high energy conversion coefficient is desired for PAI,

indicating the great potential of the TUT under receiving-only mode.

As ITO electrode introduces additional electrical impedance, it is challenging to achieve electrical matching for miniature TUTs. The ε_s of the Sm-0.72PMN-0.28PT transparent ceramics are measured as 4704. Among all piezoelectric materials as shown in Table 3.5, the transparent Sm-PMN-PT possesses the highest ε_s, while maintaining great d_{33} and k_t values. Therefore, this ceramic material should be suitable for high-frequency TUTs for endoscopy applications.

Table 3.5. Properties of the reported piezoelectric materials for miniature ultrasound transducers

Piezoelectric Materials	d_{33} (pC/N)	ε_s	k_t	Reference
Transparent Sm-PMN-PT ceramics	1407	4704	0.63	this work
0.6%Fe-0.55PNN-0.45PZT ceramics	760	3409	0.60	[90]
KNLNT ceramics	245	890	0.42	[91]
PZT-5H ceramics	593	1470	0.51	[92]
0.50BZT-0.50BCT ceramics	597	2817	0.41	[93]
0.27PIN-0.40PMN-0.33PT single crystal	2742	629	0.59	[7]
LiNbO3 single crystal	49	39	0.49	[94]
0.67PMN-0.33PT single crystal	1430	797	0.58	[95]

3.4.2 Performance of Sm-PMN-PT based TUT

In the field of PAI endoscopy for gastrointestinal track, transducers are usually operated in the frequency range between 5 to 20 MHz. Thus, the f_c of the proposed TUT was

designed as ~ 20 MHz. The detailed fabrication process is as follows.

1. A Sm-PMN-PT transparent ceramic plate with 10 mm diameter was lapped to the desired thickness of 135 μm, and both sides were well polished.
2. Transparent ITO electrodes were sputtered on both sides. Subsequently, the ceramic plate was diced into desired aperture size of 1.5 ×1.5 mm^2, and mounted on a glass substrate by the double-side tape.
3. A brass housing with 3 mm diameter was placed around the Sm-PMN-PT piezoelectric ceramic. The positive and negative wires of a co-axial cable were connected to the back surfaces of the ceramic and the brass housing with conductive silver epoxy (E-Solder 3022, Von Roll Isola Inc., USA).
4. A 105-μm fiber was placed above the Sm-PMN-PT. It was carefully aligned with the center of the ceramic plate. The distance between ceramic and distal end of fiber is around 200 μm.
5. Transparent Epoxy 301 was degassed and filled into the brass housing for backing layer. After curing at room temperature overnight, the TUT was removed from the glass substrate.
6. Parylene C was vapor deposited on the surface of the TUT with 31 μm thickness.
7. The TUT was polled by a DC electric field. The voltage amplitude was determined by the measured E_c of the transparent Sm-PMN-PT ceramic.
8. Finally, the TUT was mounted on a probe together with the co-axial cable and optical fiber. The size of the probe is 3 mm in diameter.

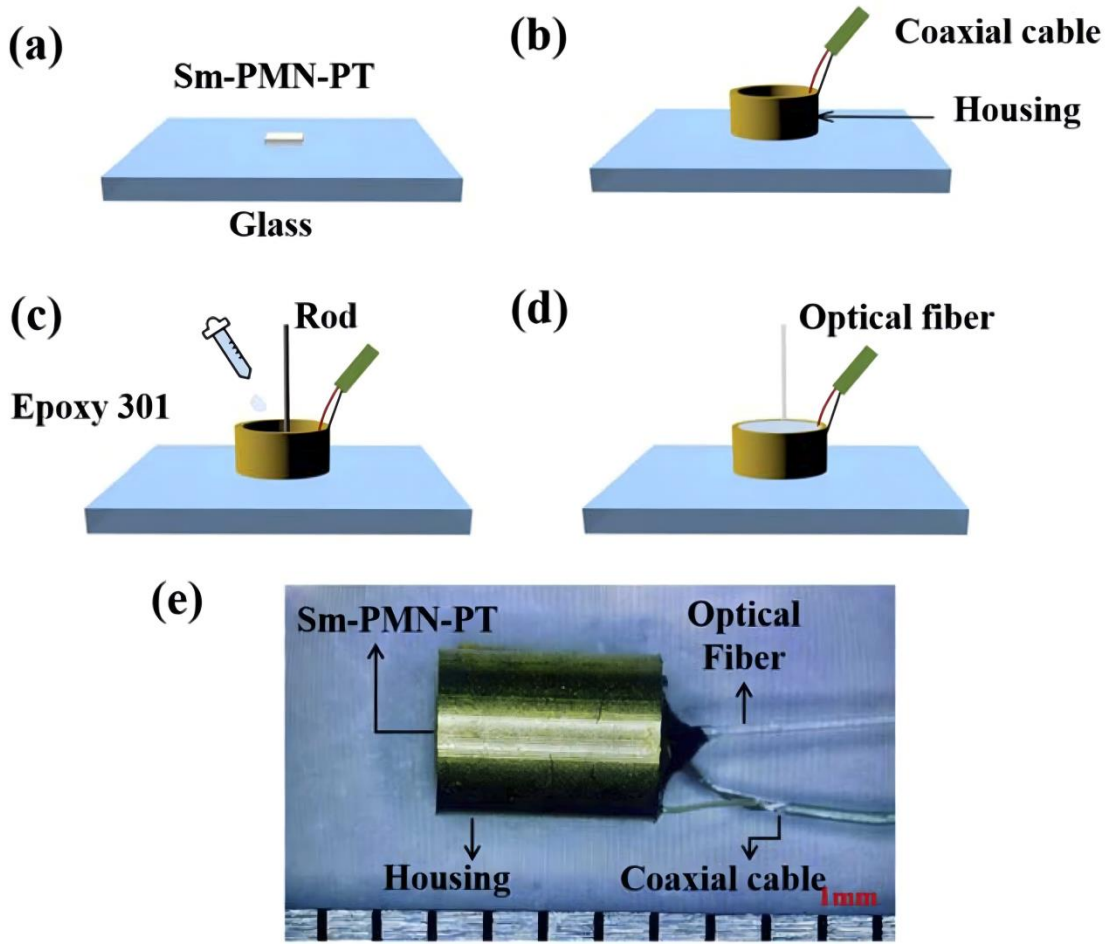

Figure 3.27 Fabrication process of Sm-PMN-PT based transparent transducer.

Fig. 3.27 shows the fabrication process of the Sm-PMN-PT transparent ceramic based TUT. The pulse-echo response of the TUT, as measured, is displayed in Fig. 3.28(a). The TUT was found to have a f_c of 18.5 MHz and a BW of 24%. As illustrated in Fig. 3.28(b), the electrical impedance of the TUT approaches the optimized value at f_c. The high k_t value of the ceramic results in a high k_{eff} of 0.62. This value is comparable to that of PMN-PT single crystal-based TUTs. The IL value was measured at approximately 28 dB. Due to the constraints imposed by the limitations of endoscopy applications, the TUT's very small aperture size is a desired feature.

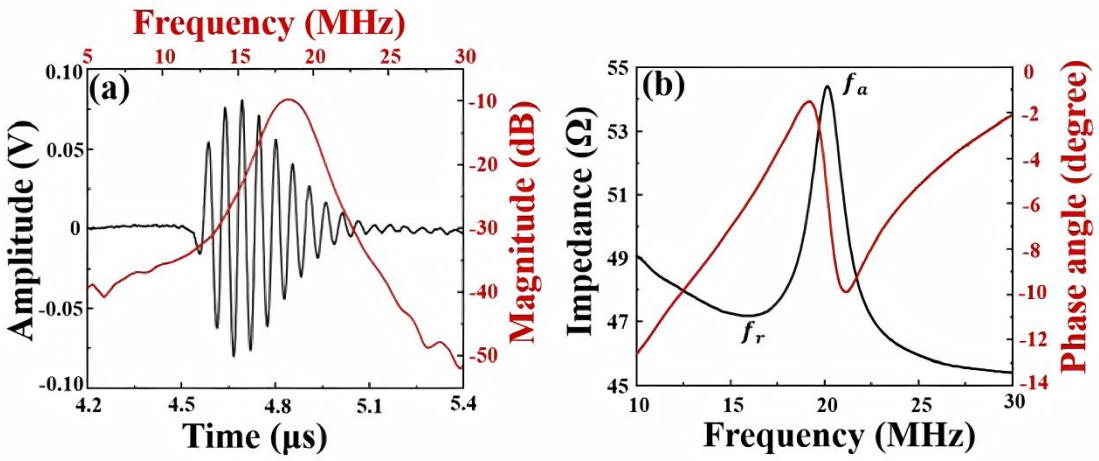

Figure 3.28 (a) Measured pulse-echo response, and **(b)** measured impedance spectra of the TUT.

The relatively low value can be attributed primarily to the small aperture size. The effective aperture size for ultrasound signal transmission is constrained, leading to a reduced signal intensity. Consequently, the reflected signal intensity of the echo signal is reasonably low. However, it is noteworthy that the sensitivity attained is sufficient for imaging applications, particularly when bench marked against existing works in this field. Furthermore, the sensitivity of PAI was considered through NEP. The theoretically estimated NEP of the Sm-PMN-PT ceramic-based TUT is 2.3 mPa/Hz at 18.5 MHz, which is significantly lower than that of the LN-TUT (11.9 mPa/$Hz^{1/2}$) and PMN-PT single crystal-TUT (9.6 mPa/$Hz^{1/2}$).

3.4.3 Imaging Performance

Fig. 3.29 shows the TUT based system for PAI, where a pulsed laser with 20 μJ laser energy was used as the laser beam. After being focused by a lens (LA1134-A, Thorlabs, USA), the laser was coupled into a fiber coupler and entering the optical fiber of the TUT. For ultrasound imaging, the TUT was connected to a pulse/receiver

operating under P/R mode. Both PA and US signals were received by the ultrasound pulser/receiver with 39 dB gain during the imaging process and digitized by a data acquisition (DAQ) board (ATS9371, AlazarTech, Canada) with a 1 GHz sampling rate in a personal computer. Data acquisition and translation of the X-Y stage were synchronized by laser source trigger, and finally, photoacoustic and ultrasound images were post-processed by MATLAB.

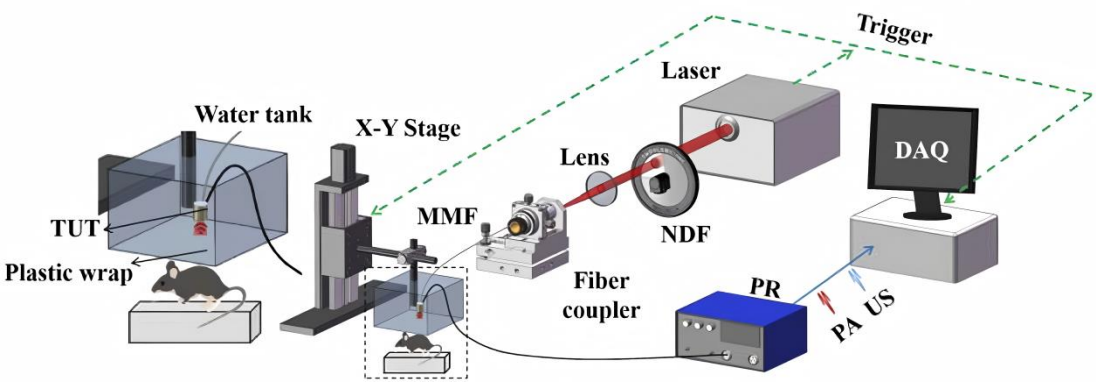

Figure 3.29 The experimental setup of the PAI system based on the proposed TUT. MMF: multi-mode fiber; NDF: neutral density filter; PR: Pulser/receiver.

The phantom and *ex vivo* samples were prepared to evaluate the TUT capability for ultrasound imaging and PAI. For *in vivo* imaging, biomolecular probe IR-1061 was injected into a healthy mouse. The mouse was immobilized on a linear stage that placed under a water tank. A plastic wrap was placed between the mouse and the water tank, where ultrasound gel was used to fill gaps.

For endoscopy applications, it is difficult to align the transducer with the samples horizontally, because this is always a small detection angle. Therefore, it is essential to study image performance at different detection angles.

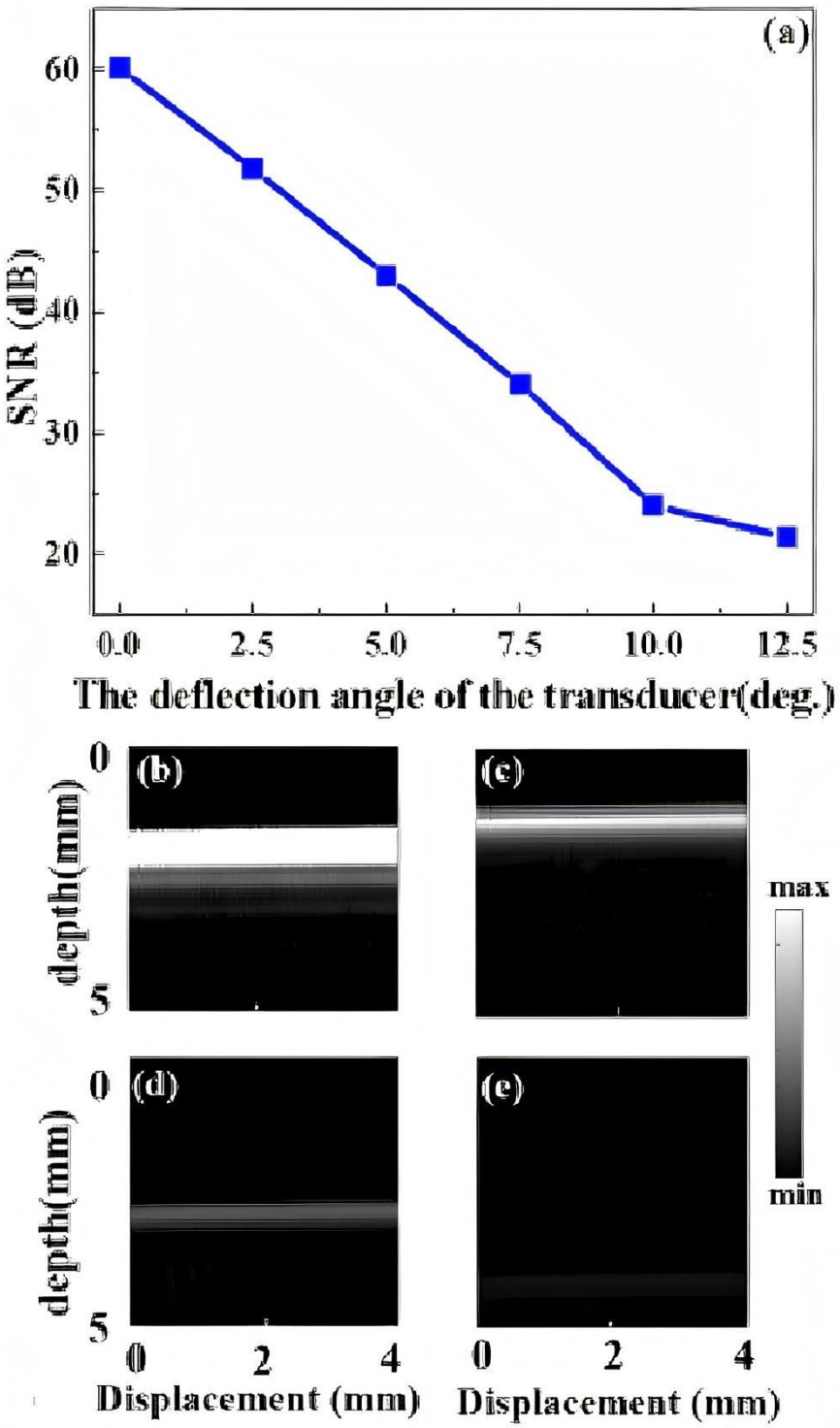

Figure 3.30 (a) The ultrasound SNR with the increase of deflecting angle when imaging a glass plate and the B-scan images while the deflecting angle is **(b)** 0°, **(c)** 2.5°, **(d)**5°, **(e)** 7.5°.

A glass plate was placed under the TUT as the reflector, and the TUT was scanned at different angles (range from 0° to 12.5°). When the TUT is horizontal to the reflector, the detection SNR is detected as 60.2 dB, and the SNR decreases as the detection angle

increases. Different B-scan ultrasound images are shown in Figs. 3.30(b)-(e). One can see that, when the angle of detection reaches 12.5°, the SNR decreases to 21.4 dB. For endoscopy applications, the detection angle is generally less than 10°. According to Fig. 3.30(a), the corresponding SNR is considered enough for practical imaging applications.

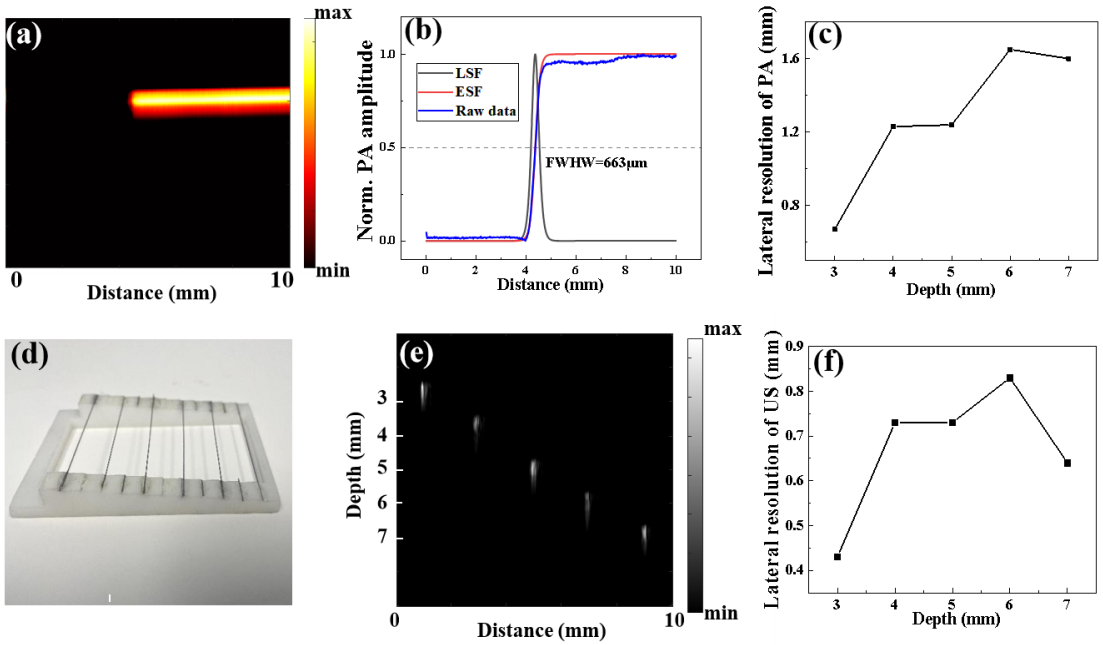

Figure 3.31 (a) The scanned PAI of a sharp edge, **(b)** Lateral resolution of the coaxial system with TUT. Blue line: raw data; red line: fitted ESF; gray line: derived LSF, **(c)** Lateral resolution of PAI at different depths. **(d)** The photograph of the pencil leads, **(e)** the maximum amplitude projection (MAP) US image of pencil leads, and **(f)** The lateral resolution of ultrasound imaging at different depths.

Lateral resolutions of the TUT based PAI system were evaluated with a sharp knife edge method by measuring the size of focused laser spot. The detailed measurement method is similar to that shown in the previous chapter. According to Figs. 3.31(a) and (b), the PAI later resolution at 3 mm depth is determined as 663 μm. The lateral resolutions at different depths were also measured as shown Fig. 3.31(c). It is found that the lateral resolution increases with the increased depths.

Tungsten wires with a diameter of 200 μm were placed at different depths for

spatial resolution of the ultrasound imaging (Fig. 3.31(d)). The TUT was scanned to obtain the B-mode image of these wires, as shown in Fig. 3.31(e). Fig. 3.31(f) shows the calculated lateral resolutions of the TUT at different depths; at 3 mm image depth, the later resolution is 432 μm.

Practical imaging of the Sm-PMN-PT ceramic based TUT was first evaluated by black tapes. As shown in Fig. 3.32(a), several characters were arranged by black tapes. The maximum amplitude projection (MAP) was scanned with an 18×7 mm^2 imaging area. The energy of the 1064 nm wavelength laser is measured to be 6 μJ, which satisfies the established safety requirement. As demonstrated in Fig. 3.32(b), the black tape-based characters were successfully imaged, thereby indicating the PAI ability of the TUT-based probe. Furthermore, the *ex vivo* samples were prepared with chicken breast meat and black tape. A black tape was placed on one piece of chicken breast meat, while the other piece of chicken breast is covered with a black tape. The thickness of the chicken breast meat used for covering varies from 1.5 mm to 4.0 mm, thereby demonstrating imaging depths that vary accordingly. There are large discrepancies between the laser energy absorption coefficient and acoustic impedances of the two samples, thus enabling clear imaging of both ultrasound and PAI. During the experiment, the laser energy always remains within the safety range. This approach enables the clear imaging of the internal structure and thickness of the chicken breast coverings. The SNR of the ultrasound image by the TUT is calculated to be 38 dB, and the SNRs of the PAIs at different depths were shown as 44, 24, and 20 dB respectively.

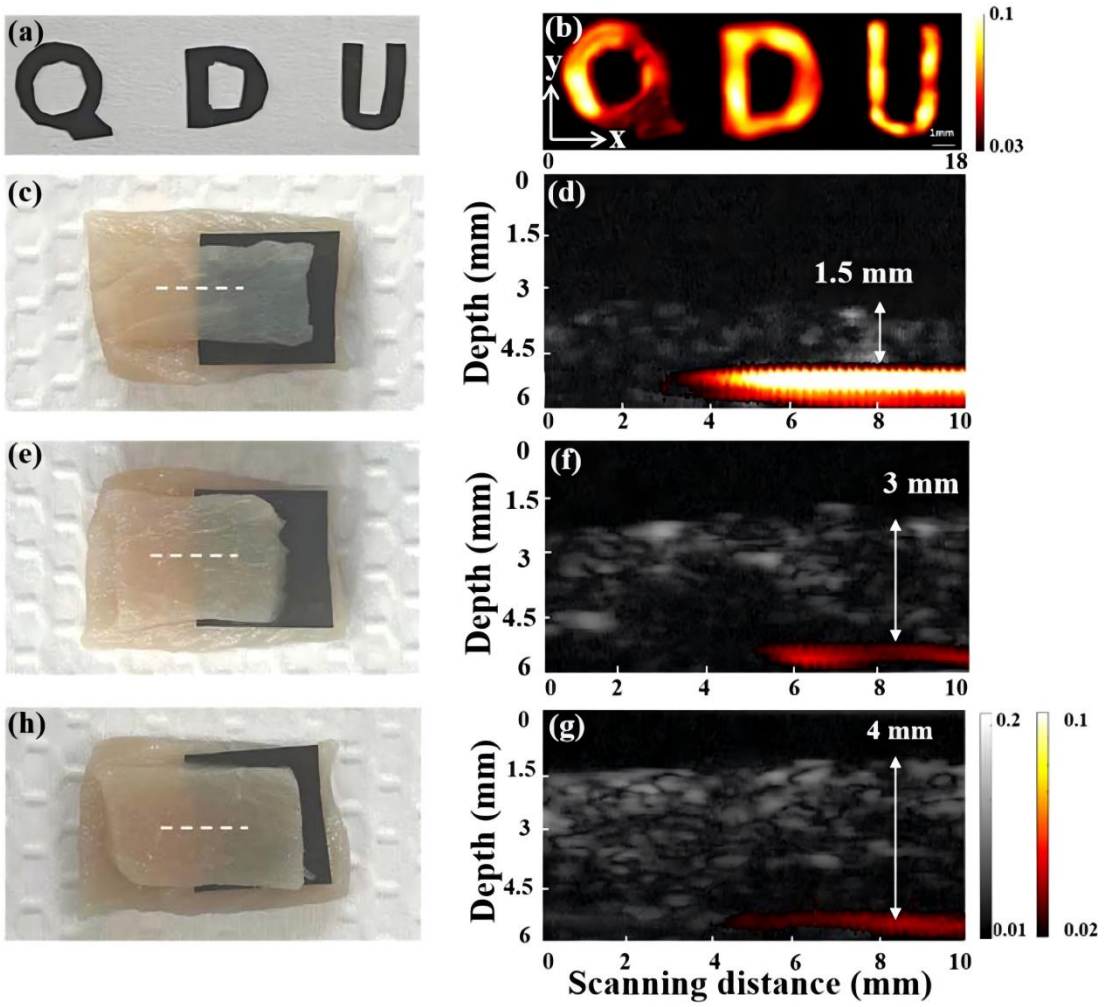

Figure 3.32 (a) The photo of black tape-based phantom, and (b) the MAP PAI by the proposed TUT. (c-g) The photographs of black tape covered by the chicken breast of increasing thickness (c) 1.5 mm, (e) 3.0 mm, (g) 4.0 mm, and (d), (f), (h) are the fusion images of PA and US along the white dotted lines of (c), (e) and (g) respectively.

In order to demonstrate the advantages of the Sm-PMN-PT ceramic in comparison to commonly used LN single crystal, a TUT fabricated from LN crystal was utilized for comparative analysis. The dual-modality images of the *ex vivo* samples are illustrated in Fig. 3.33. The SNRs of PAIs of the LN-based TUT are 32, 20, and 18 dB, respectively, and the SNR of ultrasound imaging of the chicken tissue is 36 dB. The Sm-PMN-PT ceramic-based TUT exhibits a notable advantage over the LN-based TUT in terms of its capability to penetrate deep tissues. The signal-to-noise ratio (SNR) also demonstrates the superior performance of the Sm-PMN-PT ceramic-based TUT. It is

important to note that the principle of PAI, in which the transducer's small aperture size can potentially compromise detection sensitivity, is an important consideration. However, the miniature TUT demonstrated in this study exhibits sufficient image quality. In comparison to a TUT based on PVDF, the Sm-PMN-PT ceramic-based TUT demonstrates the capability to achieve equivalent image quality with reduced laser energy, underscoring its significant potential.

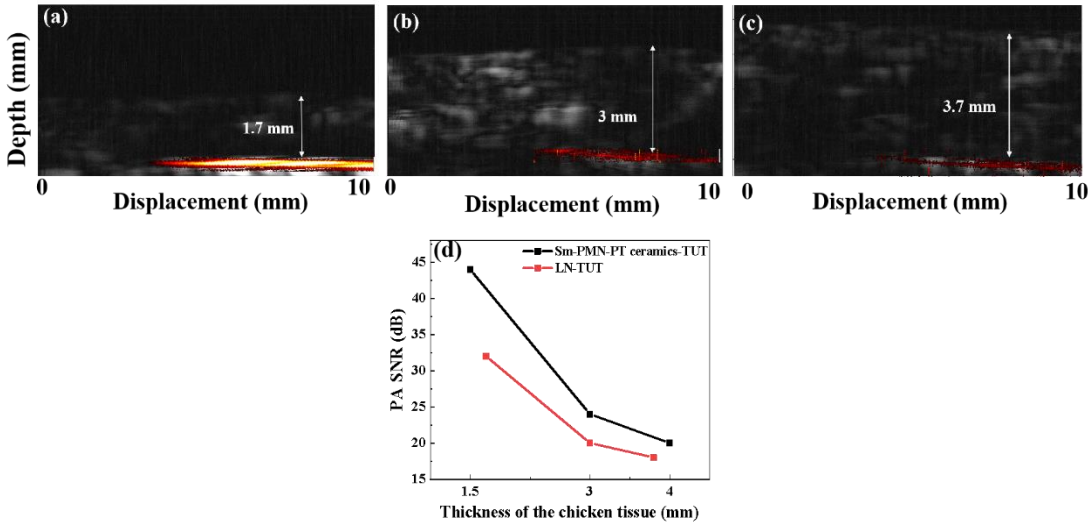

Figure 3.33. Dual-modality image of the *ex vivo* samples by LN-based TUT. The thickness of each covered chicken breast is **(a)** 1.7 mm, **(b)** 3.0 mm, and **(c)** 3.7 mm, respectively. **(d)** Comparison of PAI SNR of the Sm-PMN-PT based TUT to the LN based TUT..

The dual-modality *in vivo* imaging was conducted based on the proposed TUT. As illustrated in Fig. 3.34(a), the imaging area is delineated, while Fig. 3.34(b) details the injection of the IR-1061 solution. The laser energy density was measured to be 0.5 mJ/cm^2 for the *in vivo* imaging procedure. The fused dual-modality image is shown in Fig. 3.34(c), where the ultrasound images reveal the structure of the imaging target; this allows for clear distinction between the plastic wrap and biological tissues of the mouse. The functional information was labeled through the PAI, where the biomarker by the IR-1061 solution can be detected at 1.2 mm under the mouse skin. For comparison, the

PMN-PT single crystal-based TUT detected the functional information in biological tissues with laser energy of 15 mJ/cm^2 at a wavelength of 532 nm. The *in vivo* ultrasound/PAI capability for small animals, based on the Sm-PMN-PT TUT, has been successfully demonstrated.

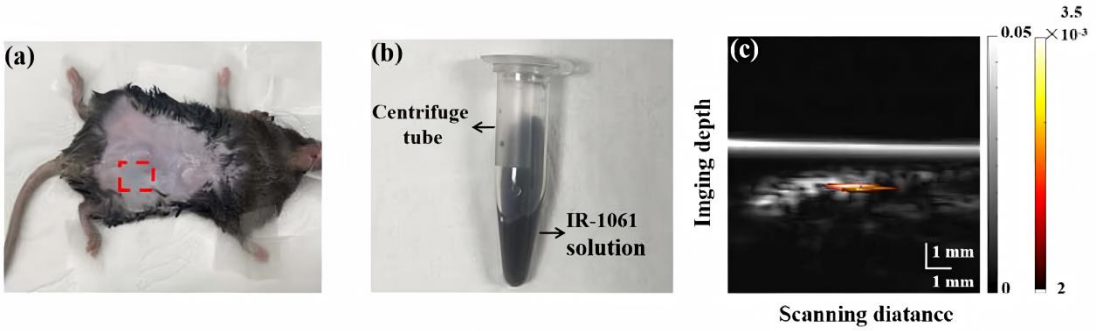

Figure 3.34 (a) Photograph of the healthy mouse was injected with biomolecular probe IR-1061. **(b)** The IR-1061 solution**. (c)** The fusion PA and US B-scan image of the injected area of the mouse's abdomen.

For the above experiments, there are no additional optical or acoustic components to focus the laser beam and the ultrasound wave in the probe, making it simpler in structure, smaller in size, and easier in fabrication, but still efficient in PA imaging. Therefore, the Sm-PMN-PT transducer would be beneficial for the design of endoscopic catheter which has requirements of high sensitivity and a small size of the probe.

In summary, the 2.5Sm-0.72PMN-0.28PT transparent ceramic was synthesized with transparency achieving 69 % for various wavelengths of thick ceramic plate. The piezoelectric property of the ceramic is excellent with d_{33} reaching to 1460 pC/N and ε_s reaching 4704. A miniature TUT was fabricated based on the Sm-PMN-PT transparent ceramics with only 1.5×1.5mm^2 aperture size, which is smaller than other reported TUTs. The miniature TUT is suitable for practical endoscopy imaging application.

Electrical impedance of the TUT was measured near the optimal value, and the k_{eff} is measured as 0.62 due to high k_t of the material. Phantom imaging was conducted to evaluate imaging capability of the proposed TUT, and the results present great advantages compared to the LN-based TUT. The high SNR indicates great potential for dual-modality ultrasound/PAI applications. The *in vivo* imaging of the dual-modality ultrasound/PAI imaging was successfully demonstrated, where the PAI was labeled by injected biomolecular probe.

There is one consideration of transparent piezoelectric materials we used in this chapter is their relatively low curie temperature. The TUT itself will absorb laser energy to generate a photoacoustic signal. However, the light absorption is considered to be of negligible significance in elevating the temperature at the TUT. For instance, the Curie temperature of the PZN-PT single crystal is approximately 60 ℃. Following the execution of numerous PAI experiments, the sensitivity of the TUT remained constant. This finding indicates that the temperature at the TUT surface is less than 60°C. Furthermore, it has been demonstrated that the epoxy will undergo deformation when exposed to temperatures in the vicinity of 60 °C. The integrity of all TUTs' structures remained intact, thereby substantiating the hypothesis that the temperature did not exceed a critical threshold.

Chapter 4. Development of TUT Array

In aspect of PAI system, due to large field of view (FOV) and high imaging speed, ultrasound arrays are more desired compared to single element transducers. Table 4.1 summarizes the performance of reported TUT arrays.

Table 4.1 Performance of reported TUT arrays

	f_c (MHz)	BW	Thickness of Piezoelectric Layer (μm)	Theoretical f_c (MHz) (λ/2 mode)
LN based TUT array	5.94/7.69	6.2%/7.6%	500	7.3
PVDF based TUT array	4.3	N/A	28	25

Recently, a dual-frequency TUT linear array based on lithium niobate (LN) single crystal for phantom imaging was reported [40]. However, pulse-echo waveform of elements showed dual-frequency phenomenon with relatively long pulse duration, which could be led by the sub-dicing fabrication process. In addition, ITO-coated glass was bonded as backing layer, which resulted in the mass-load effect to decrease the f_c, therefore, imaging quality was affected due to the irregular waveform. In addition, a 16-element array transducer based on transparent polyvinylidene fluoride (PVDF) was developed. In their transducer, all elements were aligned manually instead of using conventional dice-and fill method. Due to this fabrication process, the pitch was larger than 1.5 times wavelength, which limited the image quality [96]. Additionally, fibers were bonded directly on the backside of each element. The bonded fiber may prevent the original vibration mode of the piezoelectric element, and the 28 μm-thick PVDF only achieved f_c as 4.3 MHz, which is far from theoretical value.

There is no study of high-frequency TUT arrays with proper geometries, and no reported array can be operated at theoretical frequencies of the piezoelectric elements. In my study, a novel fabrication process was investigated to fabricate a high-frequency TUT array with 64 elements, where kerfs were diced after bonding flexible circuits. The acoustic and photoacoustic performance of the transducer were characterized, and the photoacoustic A-line of each element was successfully detected.

4.1 Design of the TUT Array

To design high-frequency TUT array, the pitch (p) of elements should be in the range of:

$$0.5\lambda \leq p \leq 1.5\lambda \tag{17}$$

where λ is the wavelength in acoustic transmission media. To avoid shear waves during piezoelectric material vibration, the element width (w) and kerf width (d) should follow the following relations:

$$w \leq 0.6t \tag{18}$$

$$d \leq \frac{V_s}{4f_c} \tag{19}$$

where t is the thickness of piezoelectric elements, V_s is the shear wave velocity of kerf filler, and f_c is the center frequency of the transducer [97]. Based on design principles, the f_c is set as 17 MHz with 190 μm-thick LN single crystal possessing high transparency, high electromechanical coefficient and high receiving sensitivity. Subsequently, pitch and kerf widths are determined as 120 and 15 μm, respectively. For elevation size of the TUT array, it is designed as 5 mm following mostly reported arrays

[98].

Table 4.2 Design parameters of the 64-element high-frequency TUT array

Center Frequency	17 MHz
Element Width	0.105 mm
Elevation Size	5 mm
Element Thickness	0.19 mm
Matching layer Thickness (Parylene C)	0.035 mm
Backing layer Thickness (Epoxy)	5 mm

To ensure sensitivity of the TUT, pure epoxy (ERO-TEK 301) was employed for backing layer due to its relatively low acoustic impedance. Also, Parylene C was designed for transparent acoustic matching layer to further enhance acoustic wave transmission efficiency. For array development, the key consideration is to guarantee its sensitivity. Considering the small aperture size, low dielectric permittivity of the lithium niobate, and the high sheet resistance of ITO electrode, the electrical impedance of each element is theoretically high. Although a custom-made electrical matching circuit was employed, the sensitivity of each element is still a key consideration in this study. We select the matching layer to enhance the sensitivity mainly. According to previous studies, although the PMMA matching layer can improve the bandwidth, the sensitivity was not enhanced. In this condition, the transparent Parylene C was selected as the matching layer. Design parameters of the TUT array are shown in Table 4.2.

4.2 Fabrication of the TUT array

The TUT array was fabricated following the procedures:

1. The LN wafer with 7.68 × 5 mm^2 aperture size was first lapped down and polished to a desired thickness of 190 μm, and transparent electrode indium tin oxide (ITO) was sputter deposited on the top surface of the LN. To ensure both high transparency and low sheet resistance (~40 Ohm/sq), the ITO sputter deposition process was performed under 1.8 mTorr pressure with 45 Watt DC power at room temperature.

2. A custom-made flexible circuit with 64 metal wire traces was then adhered along the side of LN. It was carefully aligned with the elevation side of LN under optical microscopy and bonded by M-Bond 610 epoxy. After curing at room temperature for 3 days, the exceeded bonding agent was removed carefully by acetone.

3. Degassed transparent low viscosity epoxy was backfilled for both stabilization and backing layer. Cured at room temperature for overnight, the backside was then lapped flat for further processing.

4. The entire structure was placed into the dicing saw with the other surface of LN up. Due to the transparent nature of the device, the bonded metal wires can be obtained under optical microscopy of dicing saw. Thus, the dicing path can be aligned based on the metal wires. The dicing depth was set as slightly over the thickness of LN to make sure each element can be successfully separated.

5. The diced sample was placed into a drying box for overnight to dry the distilled water in kerfs which was introduced during the dicing process. The sample was then fixed on a glass substrate by double sided tape with the backing layer facing up. Degassed epoxy

was dropped at the sides for kerf filling based on capillarity.

6. After curing, brass housing was placed around the sample, where a co-axial cable was connected to the housing by silver loaded epoxy. Degassed epoxy was filled again for insulation and stabilization.

7. Finally transparent and conductive ITO electrode layer was sputter deposited as ground electrode.

8. The Parylene layer was deposited (quarter-wavelength thick) on the front surface of the TUT array for acoustic matching.

Fig. 4.1 shows the photograph of fabricated 64-element TUT array. One can see that, along the elevation, the flexible circuit covers around 2 mm length, while the other part was fully transparent for light path. Based on our proposed novel fabrication method, bonding area and piezoelectric elements are clearly separated.

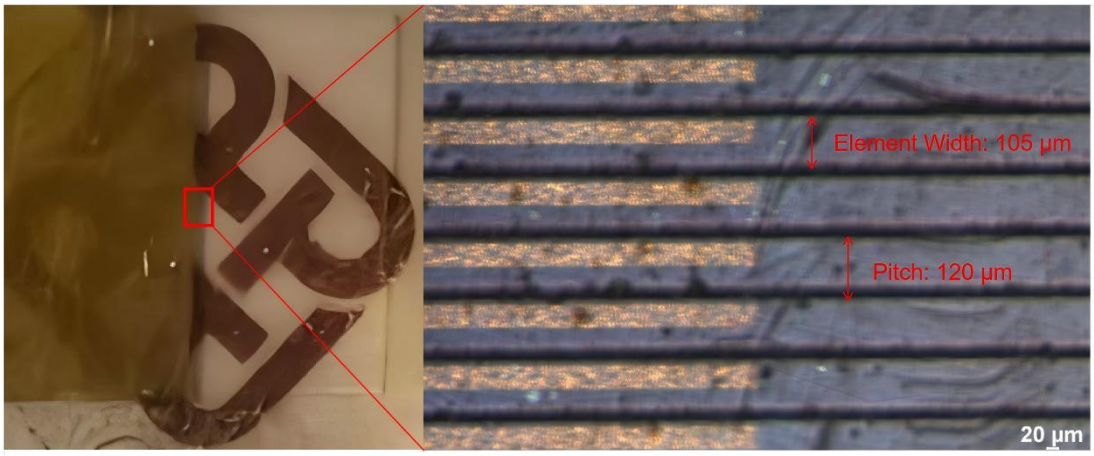

Figure 4.1 Photograph of developed TUT array.

4.3 Characteristics of the array

Performance of the TUT array transducer including acoustic and electrical

properties was characterized. The flexible circuit was connected to a custom-made electrical matching adaptor, and electrical impedance of each element at f_c was measured with impedance analyzer. The electrical matching circuit was connected with a flexible circuit to obtain the electrical properties. The characteristic impedance, conductance and attenuation were measured through a network analyzer. The series resistance, series inductance, and capacitance were recorded by an impedance analyzer. Then each element was connected to pulse/receiver for measuring pulse-echo response with 4 μJ energy and 40 dB gain, and a digital oscilloscope was employed for single acquisition with 50 Ω damping. Acquired pulse-echo signal was analyzed by fast Fourier Transformer (FFT) to obtain frequency spectra.

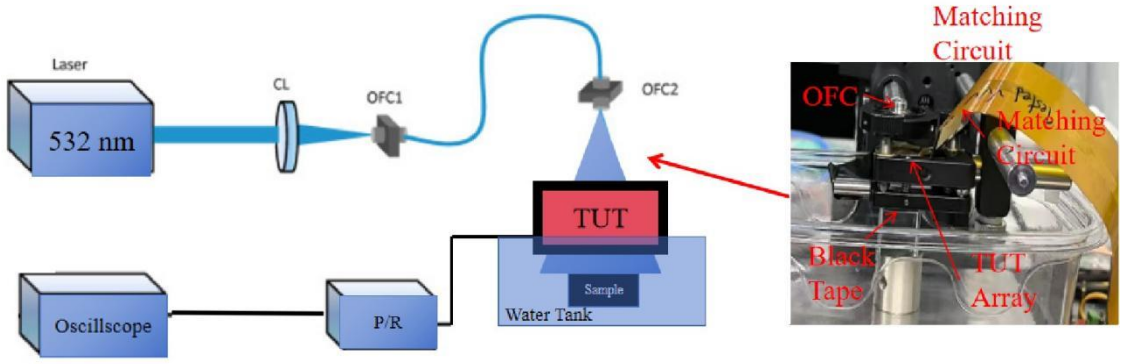

Figure 4.2 Schematic of photoacoustic system based on TUT array. CL: coupled lens; OFC: Optical fiber connector; P/R: pulser/receiver.

To evaluate PAI capability, photoacoustic A-line of each element was measured with system setup shown in Fig. 4.2. During the measurement, a laser beam was emitted from the Nd:YAG 532 nm pulsed laser and coupled to an optical fiber with 105 μm core diameter. A fiber was placed above the TUT array which was mounted on a self-designed holder, and the laser beam was expanded naturally after transmitting from the

fiber distal end. A black tape was placed under the TUT array to generate photoacoustic A-line which can be acquired by elements of TUT array. The acquired signal was amplified by a pulse/receiver and displayed on a digital oscilloscope with 128 times averaging. Light transmission efficiency was measured by calculating the laser energy before and after transmitting the TUT array.

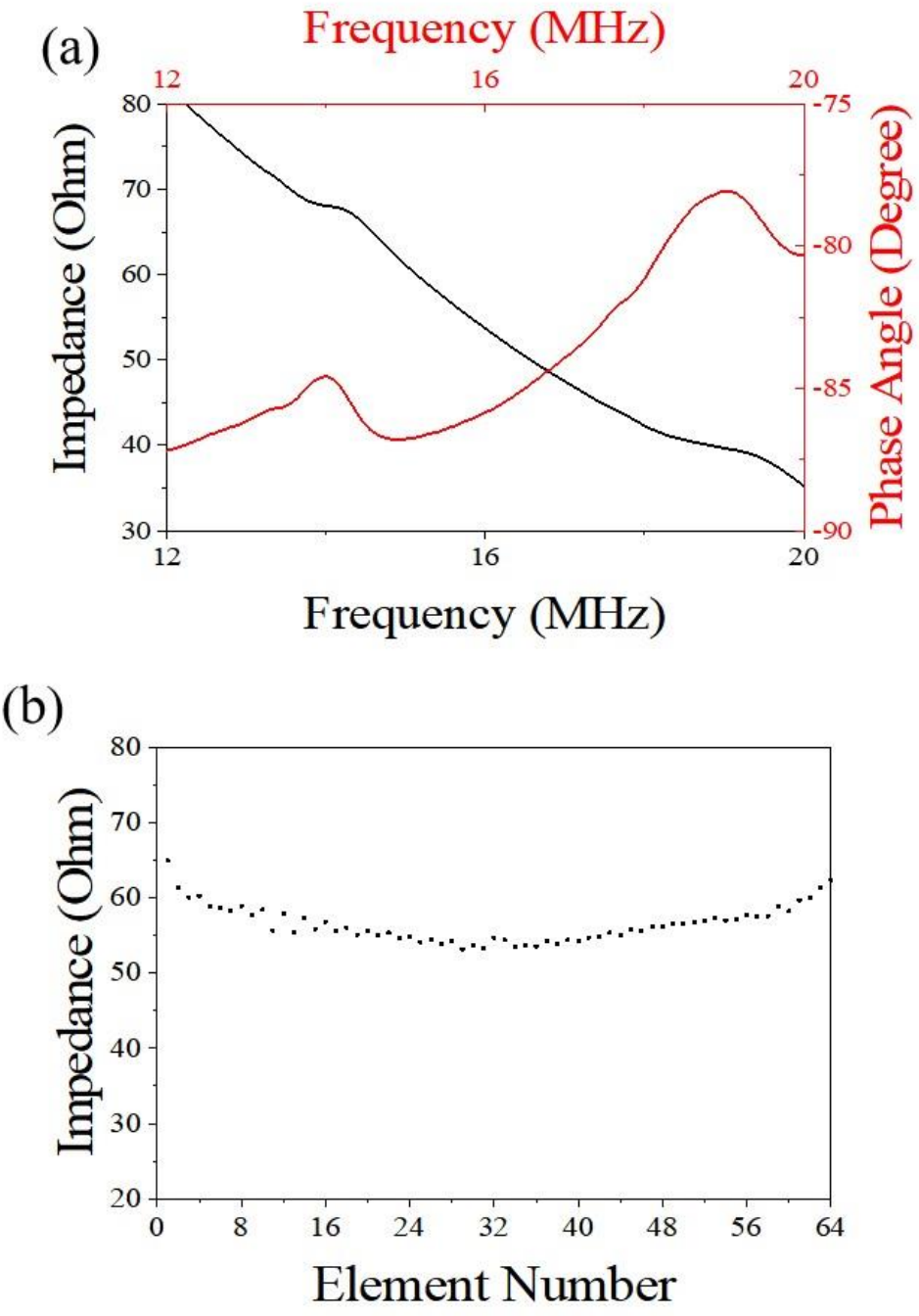

Figure 4.3 (a) Measured impedance spectra of element #32, and **(b)** uniformity of electrical impedance for all elements.

As illustrated in Table 4.3, the electrical matching circuit and the flexible circuit have been measured. Given the low dielectric value of LN single crystal and the high sheet resistance of ITO electrode, the characteristic impedance was designed to be reasonably high. Impedance spectra and phase angle of one selected element are shown in Fig. 4.3(a). It is apparent that, since each LN element is operated with small aperture size, the resonance frequency and anti-resonance frequencies are relatively weak. The electrical impedance at f_c is 54.7 Ω, which was near optimal value (50 Ω) due to the custom-made circuit. Total 64 elements show similar electrical impedance at designed f_c, indicating satisfied uniformity of the developed TUT array.

Table 4.3. Measured properties for the additional circuits (Characterized at 17 MHz)

Characteristic impedance	294.6 + 227.7i Ω
Conductance	4.5 mS
Attenuation	1.1 dB
Inductance	8.2 μH
Capacitance	9.74 pF
Resistance	25.2 Ω

The simulated and measured pulse-echo response of one element are shown in Figs. 4.4 (a) and (b), where f_c is about 17 MHz and BW is 35%. It should be pointed out that the side wall boundary condition usually results in frequency loss in high-frequency array transducer. But in this study, the measured f_c matches well with theoretical value derived from the one-dimensional KLM model; this may be attributed to proper

stiffness of LN crystal along poling direction. It is apparent that due to the light backing with low acoustic impedance, ring-down of the signal is significant. Nevertheless, the sensitivity of the signal is considered high enough, where over 1 V peak-to-peak amplitude of the pulse-echo signal can be obtained. These results suggest that LN crystal is suitable for high-frequency TUT applications.

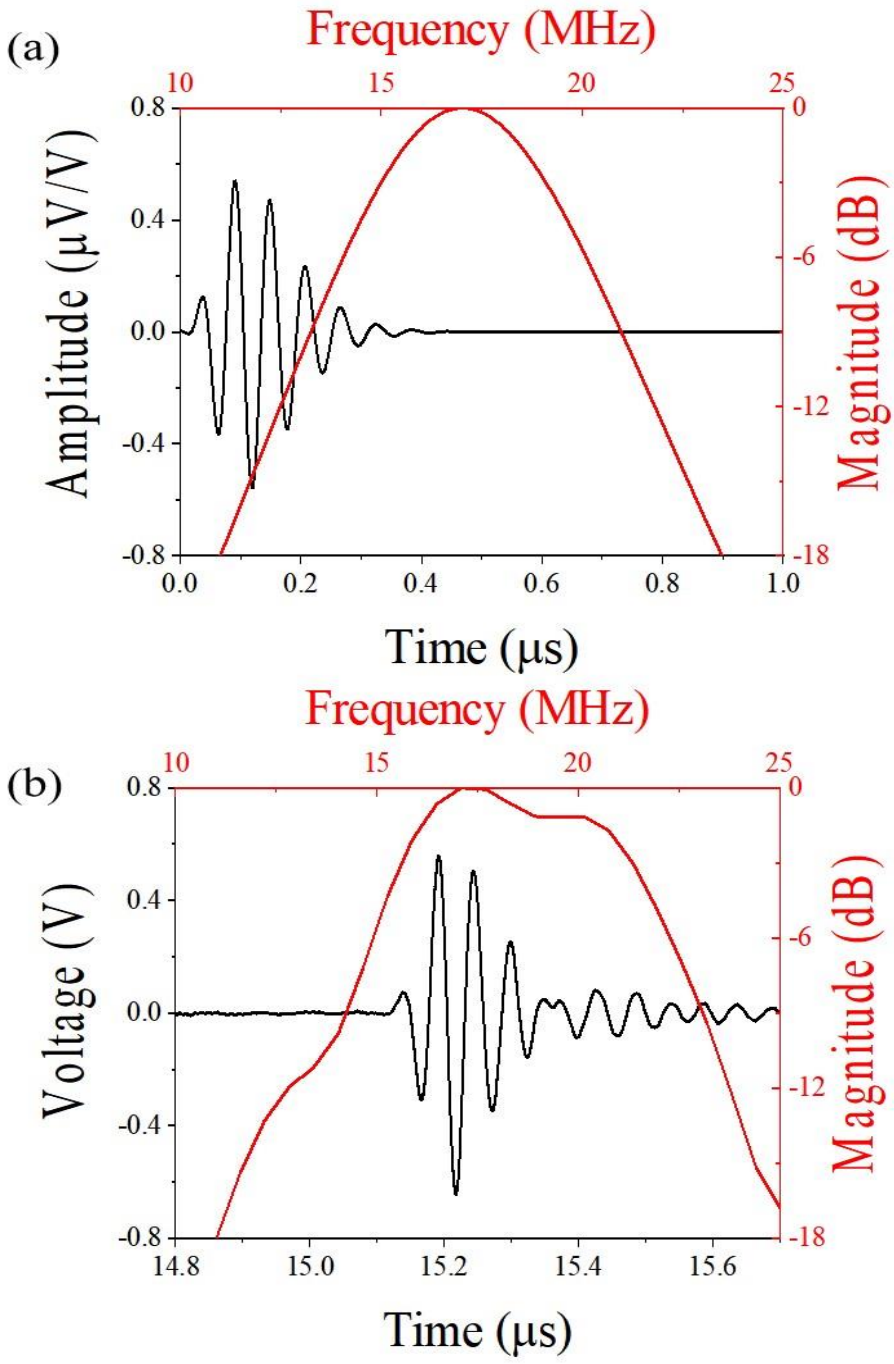

Figure 4.4 (a) Simulated and **(b)** measured pulse-echo response of one element of the TUT array.

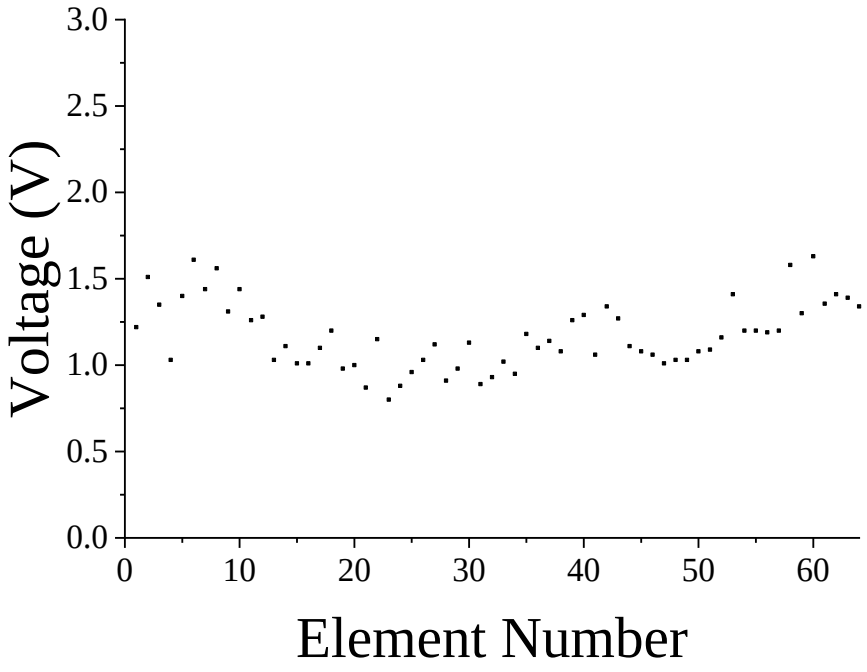

Figure 4.5 Peak-to-peak amplitude of measured pulse-echo response for all elements.

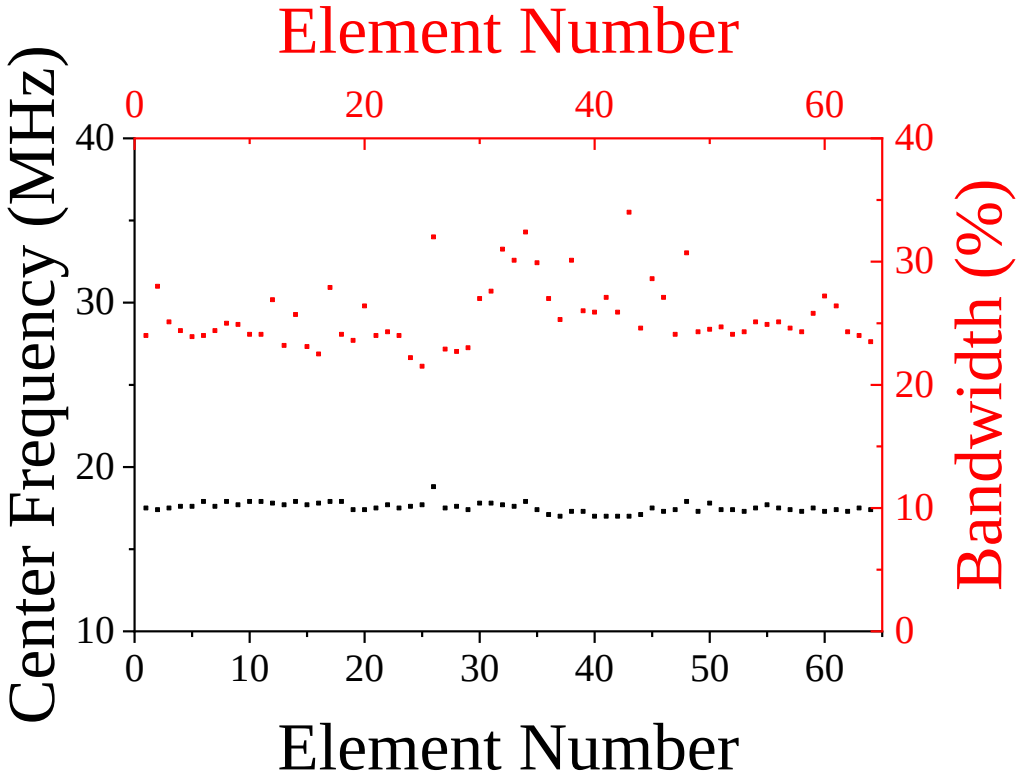

Figure 4.6 Uniformity of acoustic properties of all TUT array elements

Uniformity of acoustic properties was also characterized, and Fig. 4.5 shows peak-to-peak amplitude of all 64 elements; while Fig. 4.6 shows uniformity of f_c and BW. One can see that all elements possess almost the same f_c but with slightly different BW and amplitude. This may be attributed to the LN single crystal defects during the dicing process.

To evaluate PAI performance, light transmission efficiency was measured, and it shows ~60% transparency at 532 nm wavelength. During the measurement, the laser energy emitted from fiber was set to 6.5 mJ/cm^2 which is below the safety limit. Photoacoustic A-line generated by black tape and acquired by an element is shown in Fig. 4.7(a), where the A-line signal shows center frequency f_c as 17 MHz and BW as 33%. Noise equivalent pressure (NEP) of the array element is estimated to be 7.6 mPa/Hz$^{1/2}$ [99]. The properties of the TUT element possess comparable performance compared to a single element TUT [67].

The sensitivities of all elements were measured as shown in Fig. 4.7(b). It can be seen that the signal intensities of central elements are much stronger than the elements located at sides. This phenomenon may be due to non-uniform distribution of light intensity instead of different characteristics of elements. According to Figs. 4.3(b) and 4.6, elements at sides show similar performance compared to the central elements. The TUT array possesses composite-like structure, where light may be scattered differently when propagating through the TUT at different positions. Based on previously reported work, the signal intensity of elements at sides are considered enough for PAI [80].

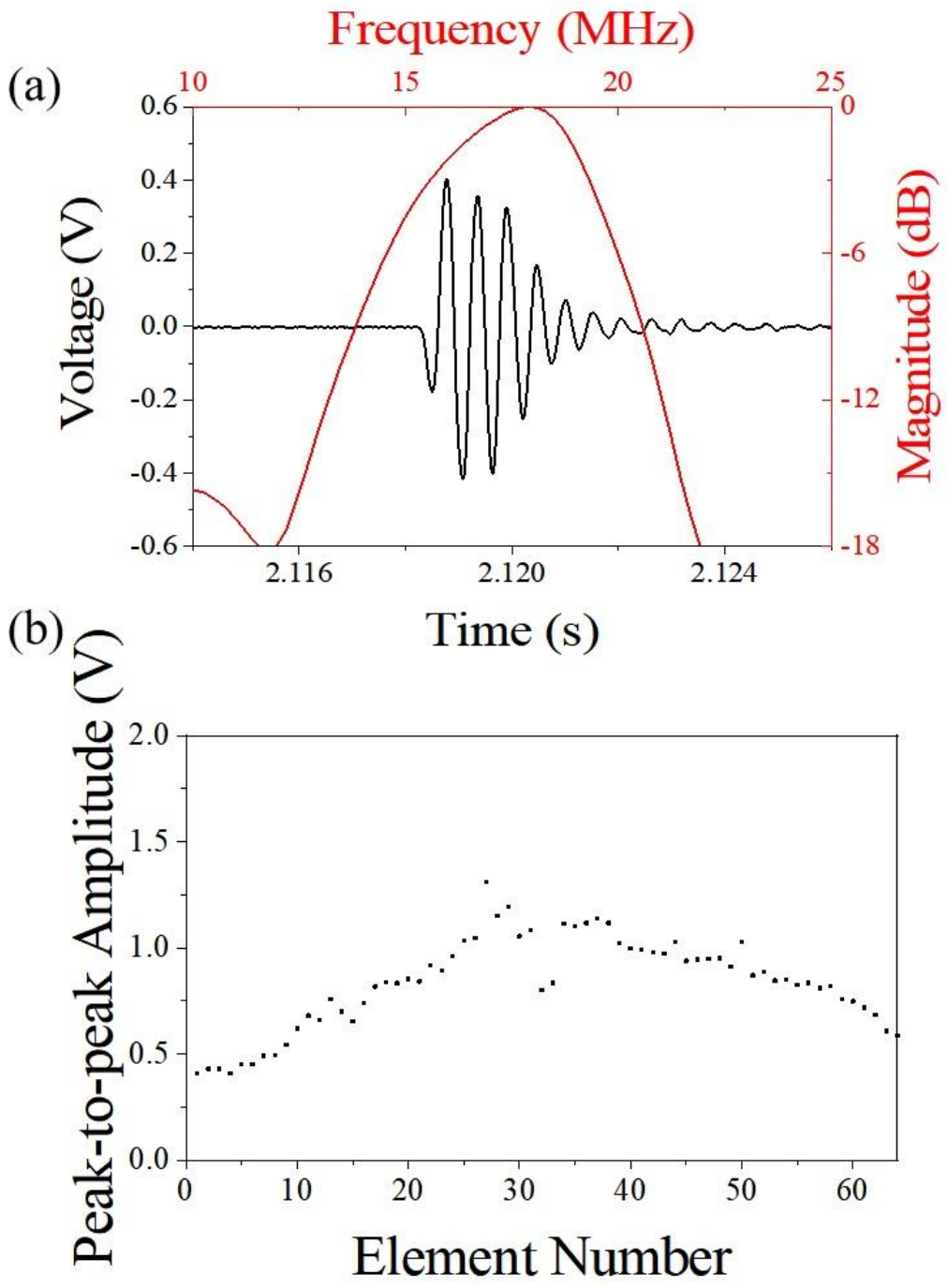

Figure 4.7 (a) Photoacoustic A-line of one selected element of TUT array, and **(b)** uniformity of photoacoustic A-line.

In summary, a 17 MHz 64-element TUT array was successfully developed, and all piezoelectric elements were characterized. The fabrication method provides a novel and universal scheme for further investigation on TUT arrays. All elements show a regular and uniform waveform at 17 MHz, which matches well with theoretical value. The *BW*

of pulse-echo response and photoacoustic A-line were measured as around 35%. The sensitivities of both ultrasound and photoacoustic signals were significantly high; the amplitudes of signals achieve over 1 V. These results indicate that the developed TUT array possesses great potential for PACT applications. There is still some room for further improvement in the TUT array. The matching and backing layers may be further improved with more proper acoustic impedance, leading to short pulse duration. Besides, to further improve receiving sensitivity of TUT arrays, alternating current poled relaxor-ferroelectric single crystal could be implemented for active layer of TUT array [100]. Unfortunately, due to the time limitation and equipment limitations, the PAI imaging based on TUT array transducer was not successful at this moment even though a lot of efforts have been made. The complexity of TUT array-based PAI makes it difficult to perform, that is the reason that there is no relevant report yet

Chapter 5. Conclusion and Future Plan

5.1 Conclusion

In PAI systems, the TUT has been demonstrated to be a powerful and effective tool for achieving co-axial laser delivery and acoustic detection. This thesis work focuses on the development of high-performance TUTs, in terms of both transparent passive and active materials. The *BW* of the TUT is enhanced to approximately 50% with the incorporation of a single PMMA matching layer; this universal scheme has great potential for the development of high-frequency TUTs. Besides, we demonstrated very good performance of TUT in PAI, including phantom and *in vivo* small animal imaging. Although the sensitivity is not enhanced due to the acoustic attenuation of bonding agent, the PAI is successfully demonstrated with the developed TUT. It is worth noting that the proposed PMMA matching layer scheme offers a new path to enhance the performance of TUTs without the limitation of center frequency.

Secondly, the investigation focuses on various transparent piezoelectric materials as potential candidates for the active layer of TUTs. The advanced AC-poled PMN-PT single crystals are studied for practical TUT applications. Different from material research only, the AC-poled PMN-PT single crystals suffer from high-voltage pulses when working for TUTs. The most optimized AC-poling conditions are studied through cycles and poling voltages. Subsequently, the investigation focuse on DC-poled PZN-PT single crystals, which are utilized as the active layer for 20 MHz TUTs. This approach leads to the successful demonstration of dual-modality ultrasound/PAI.

Additionally, rare-earth element-doped PMN-PT textured ceramics are investigated for TUT application. Miniature TUTs have been achieved due to the ultra-high ε_s of the ceramic.

Finally, a high-frequency TUT array is designed and fabricated using LN single crystals. A novel fabrication method is applied to form array elements with regular rectangle shapes, and all elements show f_c as 17 MHz and BW as ~35%. With the tailor-made electrical matching circuit, array elements show great sensitivity. The uniformity of array elements is evaluated, and the photoacoustic A-line of all elements are measured, validating the great potential for practical PACT application.

5.2 Future Work

5.2.1 Dual-element TUT Design

Polymer-based piezoelectric materials, such as PVDF, have demonstrated the capacity to achieve broadband detection with a bandwidth exceeding 100%. However, the transmitting capability imposes limitations on the dual-modality ultrasound/PAI. One potential solution to address this limitation involves the incorporation of an additional element, featuring a conventional opaque design, into the surroundings of a transparent PVDF TUT, thereby facilitating ultrasound transmission. The schematic diagram of the dual-element TUT is shown in Fig. 5.1. The transmitting element is designed as self-focused to enhance the ultrasound signal intensity at the focal point, which could lead to stronger echo signals. Additionally, if the LN crystal is used as the active layer, high exciting voltage can be applied to further enhance the transmitting

intensity. This design of TUT may facilitate high-quality dual-modality imaging.

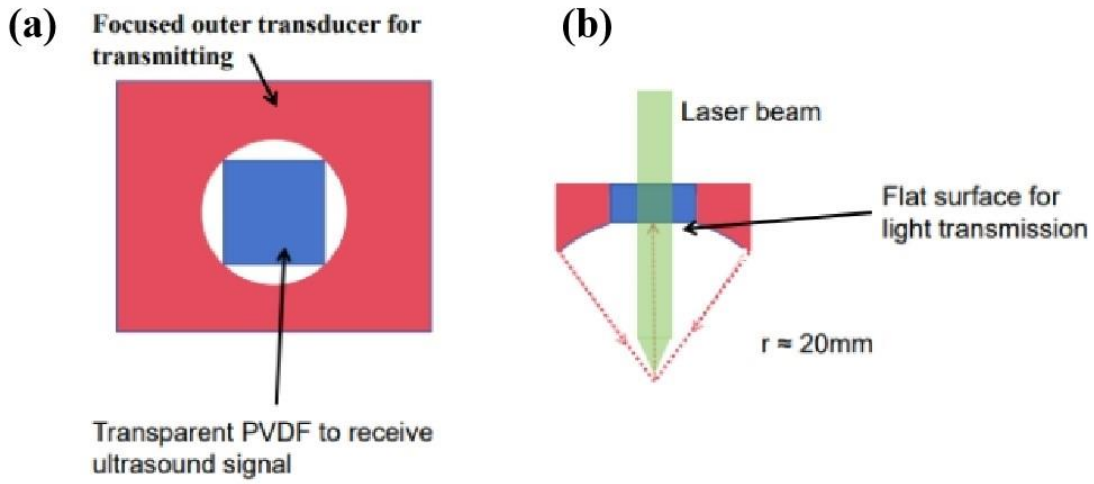

Figure 5.1 Schematic diagrams of the dual-element TUT. (a) Top view of the design and (b) side view of the design

5.2.2 Composite Material-based TUTs

While the transparent matching layers have been the subject of prior studies, achieving an ideal acoustic match remains challenging. In comparison to transparent piezoelectric ceramics and single crystals, 1-3 composites exhibit both significantly lower acoustic impedance and higher g_{33} value. Moreover, 1-3 composite-based transducers have the capacity to facilitate ultrasound imaging, i.e. a capability that surpasses polymer-based TUTs. Consequently, TUTs based on 1-3 composites are regarded as a promising solution for dual-modality ultrasound/PAI applications. The transparent epoxy component of the composites could be regarded as a conduit for light transmission. Consequently, TUT can be achieved without limitations from transparent piezoelectric materials.

5.2.3 Miniature TUT Array for free-moving Mouses

The utilization of brain imaging in free-moving animals is imperative for comprehending their neural activities in their natural states. PAI has emerged as a potent modality for brain imaging. However, the development of miniature head-mount PAI devices remains a significant challenge. One potential solution involves the utilization of a TUT as a protective barrier for the brain, facilitating the transmission of simplified light components. Consequently, the TUT array has the potential to be further optimized as a head-mounted imaging probe. Additionally, the brass housing, which is commonly used, could be removed to further reduce the device's mass.

Reference

1. Katz, O., Small, E., and Silberberg, Y., *Looking around corners and through thin turbid layers in real time with scattered incoherent light.* Nature photonics, 2012. **6**(8): p. 549-553.
2. Zackrisson, S., Van De Ven, S., and Gambhir, S., *Light in and sound out: emerging translational strategies for photoacoustic imaging.* Cancer research, 2014. **74**(4): p. 979-1004.
3. Niederhauser, J.J., Jaeger, M., Lemor, R., Weber, P., and Frenz, M., *Combined ultrasound and optoacoustic system for real-time high-contrast vascular imaging in vivo.* IEEE transactions on medical imaging, 2005. **24**(4): p. 436-440.
4. Mohammadi-Nejad, A.-R., Mahmoudzadeh, M., Hassanpour, M.S., Wallois, F., Muzik, O., Papadelis, C., Hansen, A., Soltanian-Zadeh, H., Gelovani, J., and Nasiriavanaki, M., *Neonatal brain resting-state functional connectivity imaging modalities.* Photoacoustics, 2018. **10**: p. 1-19.
5. Alchera, E., Monieri, M., Maturi, M., Locatelli, I., Locatelli, E., Tortorella, S., Sacchi, A., Corti, A., Nebuloni, M., and Lucianò, R., *Early diagnosis of bladder cancer by photoacoustic imaging of tumor-targeted gold nanorods.* Photoacoustics, 2022. **28**: p. 100400.
6. Ahn, J., Kim, J.Y., Choi, W., and Kim, C., *High-resolution functional photoacoustic monitoring of vascular dynamics in human fingers.* Photoacoustics, 2021. **23**: p. 100282.
7. Zhou, Q., Lam, K.H., Zheng, H., Qiu, W., and Shung, K.K., *Piezoelectric single crystal ultrasonic transducers for biomedical applications.* Progress in Materials Science, 2014. **66**: p. 87-111.
8. An, J., Song, K., Zhang, S., Yang, J., and Cao, P., *Design of a broadband electrical impedance matching network for piezoelectric ultrasound transducers based on a genetic algorithm.* Sensors, 2014. **14**(4): p. 6828-6843.
9. Zhang, Z., Li, F., Chen, R., Zhang, T., Cao, X., Zhang, S., Shrout, T.R., Zheng, H., Shung, K.K., and Humayun, M.S., *High-performance ultrasound needle transducer based on modified PMN-PT ceramic with ultrahigh clamped dielectric permittivity.* IEEE transactions on ultrasonics, ferroelectrics, and frequency control, 2017. **65**(2): p. 223-230.
10. Chabok, H.R., Zhou, Q., Alagha, S., Tian, J., Han, P., and Shung, K.K., *Thickness dependent characteristics of high permittivity PMN-0.32 PT single crystal for high frequency medical imaging applications.* Ferroelectrics, 2011. **422**(1): p. 70-76.
11. Krimholtz, R., Leedom, D.A., and Matthaei, G.L., *New equivalent circuits for elementary piezoelectric transducers.* Electronics Letters, 1970. **13**(6): p. 398-399.
12. Fink, M., *Time reversal of ultrasonic fields. I. Basic principles.* IEEE transactions on ultrasonics, ferroelectrics, and frequency control, 1992. **39**(5): p. 555-566.
13. Zhou, Y., Yao, J., and Wang, L.V., *Tutorial on photoacoustic tomography.* Journal of biomedical optics, 2016. **21**(6): p. 061007-061007.
14. Wang, Y., Yuan, C., Jiang, J., Peng, K., and Wang, B., *Photoacoustic/ultrasound endoscopic imaging reconstruction algorithm based on the Approximate Gaussian acoustic field.* Biosensors, 2022. **12**(7): p. 463.
15. Zhang, W., Ma, H., Cheng, Z., Wang, Z., Zhang, L., and Yang, S., *Miniaturized photoacoustic probe for in vivo imaging of subcutaneous microvessels within human skin.* Quantitative Imaging in Medicine and Surgery, 2019. **9**(5): p. 807.

16. Chen, Q., Qin, W., Qi, W., and Xi, L., *Progress of clinical translation of handheld and semi-handheld photoacoustic imaging.* Photoacoustics, 2021. **22**: p. 100264.
17. Fang, C., Hu, H., and Zou, J., *A focused optically transparent PVDF transducer for photoacoustic microscopy.* IEEE Sensors Journal, 2019. **20**(5): p. 2313-2319.
18. Kim, H.H., Cannata, J.M., Liu, R., Chang, J.H., Silverman, R.H., and Shung, K.K., *20 MHz/40 MHz dual element transducers for high frequency harmonic imaging.* IEEE transactions on ultrasonics, ferroelectrics, and frequency control, 2008. **55**(12): p. 2683-2691.
19. Jeong, M.K. and Kwon, S.J., *Side lobe free medical ultrasonic imaging with application to assessing side lobe suppression filter.* Biomedical Engineering Letters, 2018. **8**: p. 355-364.
20. Ren, D., Sun, Y., Shi, J., and Chen, R., *A Review of Transparent Sensors for Photoacoustic Imaging Applications.* Photonics, 2021. **8**(8): p. 324.
21. Ansari, R., Zhang, E.Z., Desjardins, A.E., David, A.L., and Beard, P.C., *Use of a flexible optical fibre bundle to interrogate a Fabry–Perot sensor for photoacoustic imaging.* Optics express, 2019. **27**(26): p. 37886-37899.
22. Peng, H., Cheng, Z., Zeng, L., and Ji, X., *Photoacoustic microscopy based on transparent piezoelectric ultrasound transducers.* Journal of Innovative Optical Health Sciences, 2023. **16**(05): p. 2330001.
23. Li, Z., Ilkhechi, A.K., and Zemp, R., *Transparent capacitive micromachined ultrasonic transducers (CMUTs) for photoacoustic applications.* Optics express, 2019. **27**(9): p. 13204-13218.
24. Pavageau, F., Dieppedale, C., Perreau, P., Liechti, R., Hamelin, A., Licitra, C., Casset, F., and Le Rhun, G., *Highly transparent piezoelectric PZT membranes for transducer applications.* Sensors and Actuators A: Physical, 2022. **346**: p. 113866.
25. Manwar, R. and Avanaki, K., *Manufacturing Process of Optically Transparent Ultrasound Transducer: A Review.* IEEE Sensors Journal, 2023. **23**(8): p. 8080-8093.
26. Dangi, A., Agrawal, S., and Kothapalli, S.-R., *Lithium niobate-based transparent ultrasound transducers for photoacoustic imaging.* Optics letters, 2019. **44**(21): p. 5326-5329.
27. Chen, H., Agrawal, S., Dangi, A., Wible, C., Osman, M., Abune, L., Jia, H., Rossi, R., Wang, Y., and Kothapalli, S.-R., *Optical-Resolution Photoacoustic Microscopy Using Transparent Ultrasound Transducer.* Sensors, 2019. **19**(24): p. 5470.
28. Lin, R., Zhang, J., Gao, W., Wang, X., Lv, S., Lam, K.-H., and Gong, X., *A Miniature Multi-Functional Photoacoustic Probe.* Micromachines, 2023. **14**(6): p. 1269.
29. Mirg, S., Chen, H., Turner, K.L., Gheres, K.W., Liu, J., Gluckman, B.J., Drew, P.J., and Kothapalli, S.-R., *Awake mouse brain photoacoustic and optical imaging through a transparent ultrasound cranial window.* Optics Letters, 2022. **47**(5): p. 1121-1124.
30. Chen, R., He, Y., Shi, J., Yung, C., Hwang, J., Wang, L.V., and Zhou, Q., *Transparent high-frequency ultrasonic transducer for photoacoustic microscopy application.* IEEE transactions on ultrasonics, ferroelectrics, and frequency control, 2020. **67**(9): p. 1848-1853.
31. Liao, T., Liu, Y., Wu, J., Deng, L., Deng, Y., Zeng, L., and Ji, X., *Centimeter-scale wide-field-of-view laser-scanning photoacoustic microscopy for subcutaneous microvasculature in vivo.* Biomed. Opt. Express, 2021. **12**(5): p. 2996-3007.
32. Park, S., Kang, S., and Chang, J.H., *Optically transparent focused transducers for combined photoacoustic and ultrasound microscopy.* Journal of Medical and Biological Engineering, 2020. **40**: p. 707-718.

33. Chen, H., Mirg, S., Osman, M., Agrawal, S., Cai, J., Biskowitz, R., Minotto, J., and Kothapalli, S.R., *A High Sensitivity Transparent Ultrasound Transducer Based on PMN-PT for Ultrasound and Photoacoustic Imaging.* IEEE Sensors Letters, 2021. **5**(11): p. 1-4.
34. Park, J., Park, B., Kim, T.Y., Jung, S., Choi, W.J., Ahn, J., Yoon, D.H., Kim, J., Jeon, S., Lee, D., et al., *Quadruple ultrasound, photoacoustic, optical coherence, and fluorescence fusion imaging with a transparent ultrasound transducer.* Proceedings of the National Academy of Sciences, 2021. **118**(11): p. e1920879118.
35. Chen, M., Jiang, L., Cook, C., Zeng, Y., Vu, T., Chen, R., Lu, G., Yang, W., Hoffmann, U., Zhou, Q., et al., *High-speed wide-field photoacoustic microscopy using a cylindrically focused transparent high-frequency ultrasound transducer.* Photoacoustics, 2022. **28**: p. 100417.
36. Park, J., Park, B., Yong, U., Ahn, J., Kim, J.Y., Kim, H.H., Jang, J., and Kim, C., *Bi-modal near-infrared fluorescence and ultrasound imaging via a transparent ultrasound transducer for sentinel lymph node localization.* Optics Letters, 2022. **47**(2): p. 393-396.
37. Park, J., Park, B., Ahn, J., Kim, D., Kim, J.Y., Kim, H.H., and Kim, C., *Opto-ultrasound biosensor for wearable and mobile devices: realization with a transparent ultrasound transducer.* Biomed. Opt. Express, 2022. **13**(9): p. 4684-4692.
38. Osman, M.S., Chen, H., Creamer, K., Minotto, J., Liu, J., Mirg, S., Christian, J., Bai, X., Agrawal, S., and Kothapalli, S.-R., *A novel matching layer design for improving the performance of transparent ultrasound transducers.* IEEE Transactions on Ultrasonics, Ferroelectrics, and Frequency Control, 2022. **69**(9): p. 2672-2680.
39. Cho, S., Kim, M., Ahn, J., Kim, Y., Lim, J., Park, J., Kim, H.H., Kim, W.J., and Kim, C., *An ultrasensitive and broadband transparent ultrasound transducer for ultrasound and photoacoustic imaging in-vivo.* Nature Communications, 2024. **15**(1): p. 1444.
40. Chen, H., Agrawal, S., Osman, M., Minotto, J., Mirg, S., Liu, J., Dangi, A., Tran, Q., Jackson, T., and Kothapalli, S.-R., *A transparent ultrasound array for real-time optical, ultrasound, and photoacoustic imaging.* BME frontiers, 2022.
41. Park, B., Han, M., Park, J., Kim, T., Ryu, H., Seo, Y., Kim, W.J., Kim, H.H., and Kim, C., *A photoacoustic finder fully integrated with a solid-state dye laser and transparent ultrasound transducer.* Photoacoustics, 2021. **23**: p. 100290.
42. Kim, J., Heo, D., Park, J., Cho, S., Ahn, J., Kim, J., Ha, M., Kim, H.H., and Kim, C. *High-resolution photoacoustic and ultrasound endoscope based on the transparent ultrasound transducer*. in *SPIE BiOS*. 2023. SPIE.
43. Kim, J., Heo, D., Cho, S., Ha, M., Park, J., Ahn, J., Kim, M., Kim, D., Jung, D.H., Kim, H.H., et al., *Enhanced dual-mode imaging: Superior photoacoustic and ultrasound endoscopy in live pigs using a transparent ultrasound transducer.* Science Advances, 2024. **10**(47): p. eadq9960.
44. Qiu, C., Wang, B., Zhang, N., Zhang, S., Liu, J., Walker, D., Wang, Y., Tian, H., Shrout, T.R., Xu, Z., et al., *Transparent ferroelectric crystals with ultrahigh piezoelectricity.* Nature, 2020. **577**(7790): p. 350-354.
45. Qiu, C., Zhang, Z., Xu, Z., Qiao, L., Ning, L., Zhang, S., Su, M., Wu, W., Song, K., Xu, Z., et al., *Transparent ultrasonic transducers based on relaxor ferroelectric crystals for advanced photoacoustic imaging.* Nature Communications, 2024. **15**(1): p. 10580.
46. Guo, Q., Li, F., Xia, F., Gao, X., Wang, P., Hao, H., Sun, H., Liu, H., and Zhang, S., *High-Performance Sm-Doped Pb(Mg1/3Nb2/3)O3-PbZrO3-PbTiO3-Based Piezoceramics.* ACS Applied Materials & Interfaces, 2019. **11**(46): p. 43359-43367.

47. Zheng, F., Tian, X., Fang, Z., Lin, J., Lu, Y., Gao, W., Xin, R., Fu, D., Qi, Y., and Ma, Z., *Sm-doped PIN-PMN-PT transparent ceramics with high curie temperature, good piezoelectricity, and excellent electro-optical properties.* ACS Applied Materials & Interfaces, 2023. **15**(5): p. 7053-7062.
48. Xiao, Z., Yu, S., Li, Y., Ruan, S., Kong, L.B., Huang, Q., Huang, Z., Zhou, K., Su, H., Yao, Z., et al., *Materials development and potential applications of transparent ceramics: A review.* Materials Science and Engineering: R: Reports, 2020. **139**: p. 100518.
49. Wang, S.F., Zhang, J., Luo, D.W., Gu, F., Tang, D.Y., Dong, Z.L., Tan, G.E.B., Que, W.X., Zhang, T.S., Li, S., et al., *Transparent ceramics: Processing, materials and applications.* Progress in Solid State Chemistry, 2013. **41**(1): p. 20-54.
50. Yan, P., Qin, Y., Xu, Z., Han, F., Wang, Y., Wen, Z., Zhang, Y., and Zhang, S., *Highly Transparent Eu-Doped 0.72PMN-0.28PT Ceramics with Excellent Piezoelectricity.* ACS Applied Materials & Interfaces, 2021. **13**(45): p. 54210-54216.
51. Yang, D., Yang, Z., Zhang, X., Wei, L., Chao, X., and Yang, Z., *High transmittance in lead-free lanthanum modified potassium-sodium niobate ceramics.* Journal of Alloys and Compounds, 2017. **716**: p. 21-29.
52. Chen, Y., Zhang, D., Luo, H., Peng, Z., Zeng, L., Yuan, M., and Ji, X., *3D printed Er3+ doped KNNLN piezoelectric ceramics for transparent ultrasonic transducer application.* Ceramics International, 2024. **50**(7): p. 9979-9984.
53. Fang, C. and Zou, J., *Acoustic-resolution photoacoustic microscopy based on an optically transparent focused transducer with a high numerical aperture.* Optics Letters, 2021. **46**(13): p. 3280-3283.
54. Kim, D., Park, E., Park, J., Perleberg, B., Jeon, S., Ahn, J., Ha, M., Kim, H.H., Kim, J.Y., and Jung, C.K., *An ultraviolet-transparent ultrasound transducer enables high-resolution label-free photoacoustic histopathology.* Laser & Photonics Reviews, 2024. **18**(2): p. 2300652.
55. Zhao, T., Zhang, M., Ourselin, S., and Xia, W., *Wavefront shaping-assisted forward-viewing photoacoustic endomicroscopy based on a transparent ultrasound sensor.* Applied Sciences, 2022. **12**(24): p. 12619.
56. Liu, Y.-H., Kurnikov, A., Li, W., Kazakov, V., Ni, R., Subochev, P., and Razansky, D., *Sensitive ultrawideband transparent PVDF-ITO ultrasound detector for optoacoustic microscopy.* Optics Letters, 2022. **47**(16): p. 4163-4166.
57. Zhao, T., Ourselin, S., Vercauteren, T., and Xia, W. *Miniaturized transparent ultrasound sensor for photoacoustic endoscopy*. in *Photons Plus Ultrasound: Imaging and Sensing 2022*. 2022. SPIE.
58. Liu, Y.-H., Chen, L.-X., Li, C.-Y., Lin, F.-S., Su, H.-Y., Tsai, C.-T., Wang, L.-W., Wang, Y.-H., and Huang, C.-H., *Transparent flexible piezoelectric ultrasound transducer for photoacoustic imaging system.* IEEE Sensors Journal, 2021. **22**(3): p. 2070-2077.
59. Fang, C., Zhao, Z., Fang, J., and Zou, J., *An Optically-Transparent Focused P (VDF-TrFE) Transducer for Photoacoustic Microscopy (PAM).* IEEE Sensors Journal, 2023.
60. Hu, H., Fang, C., and Zou, J. *An optically-transparent PVDF transducer array for photoacoustic tomography*. in *Photons Plus Ultrasound: Imaging and Sensing 2022*. 2022. SPIE.
61. Xia, W., Piras, D., van Hespen, J.C.G., Steenbergen, W., and Manohar, S., *A new acoustic lens material for large area detectors in photoacoustic breast tomography.* Photoacoustics, 2013. **1**(2): p. 9-18.

62. Destgeer, G., Jung, J.H., Park, J., Ahmed, H., Park, K., Ahmad, R., and Sung, H.J., *Acoustic impedance-based manipulation of elastic microspheres using travelling surface acoustic waves.* RSC advances, 2017. **7**(36): p. 22524-22530.
63. Thiagarajan, S., Martin, R.W., Proctor, A., Jayawadena, I., and Silverstein, F., *Dual layer matching (20 MHz) piezoelectric transducers with glass and parylene.* IEEE Transactions on Ultrasonics, Ferroelectrics, and Frequency Control, 1997. **44**(5): p. 1172-1174.
64. Wong, C.-M., Chan, S.-F., Wu, W.C., Suen, C.-H., Yau, H.-M., Wang, D.Y., Li, S., and Dai, J.Y., *Tunable high acoustic impedance alumina epoxy composite matching for high frequency ultrasound transducer.* Ultrasonics, 2021. **116**: p. 106506.
65. Yong, Z., Junjie, Y., and Lihong, V.W., *Tutorial on photoacoustic tomography.* Journal of Biomedical Optics, 2016. **21**(6): p. 061007.
66. *US-ANSI. ANSIZ136.1-2007 American National Standard for Safe use of lasers(Laser Institute of America, Orlando, 2007).*
67. Mirg, S., Chen, H., Khandare, S., Osman, M., and Kothapalli, S.-R., *Noise considerations in piezoelectric transparent ultrasound transducers for photoacoustic imaging applications*. SPIE BiOS. Vol. 11960. 2022: SPIE.
68. Ilkhechi, A.K., Ceroici, C., Li, Z., and Zemp, R., *Transparent capacitive micromachined ultrasonic transducer (CMUT) arrays for real-time photoacoustic applications.* Optics Express, 2020. **28**(9): p. 13750-13760.
69. Yu, Y., Feng, T., Qiu, H., Gu, Y., Chen, Q., Zuo, C., and Ma, H., *Simultaneous photoacoustic and ultrasound imaging: A review.* Ultrasonics, 2024: p. 107277.
70. Guan, Y., Hang, H., Lin, D., Wang, X.a., Tang, Y., and Luo, H., *Enhancement of 10 MHz single element ultrasonic transducers based on alternating current polarized PIN-PMN-PT single crystals.* Sensors and Actuators A: Physical, 2023. **354**: p. 114275.
71. Ma, Z., Jia, N., Li, C., Ning, L., Dang, Y., Du, H., Li, F., and Xu, Z., *Improved piezoelectric properties of 2–2 piezoelectric single crystal composites for acoustic transducer applications via alternating current polarization.* Materials Letters, 2023. **353**: p. 135284.
72. Zou, C., Li, Y., Hou, S., Liu, Z., Tang, H., Chen, S., and Peng, J., *Development of Cardiac Phased Array With Large-Size PZN-5.5%PT Single Crystals.* IEEE Transactions on Ultrasonics, Ferroelectrics, and Frequency Control, 2022. **69**(2): p. 744-750.
73. Quan, Y., Yang, X., Fei, C., Zhao, T., Zhang, J., Li, Z., Sun, X., Chen, Q., Chen, J., and Yang, Y., *PZN-PT single crystal based high-frequency intravascular ultrasound transducers.* Ceramics International, 2024.
74. Manikandan, C., Varadarajan, E., Vijayakumar, P., Ramesh, R., Roy, V., Sarguna, R.M., Amaladass, E.P., Ganesamoorthy, S., Vinodkumar, T.K., Unni, M.N., et al., *Realization of high performance PZN-PT single crystal based piezoelectric flexural mode hydrophone for underwater sensor applications.* Materials Research Express, 2023. **10**(6): p. 066303.
75. Li, F., Qiu, C., Zhang, Z., Xu, Z., Qiao, L., Zhang, S., Su, M., Wu, W., Song, K., and Xu, Z., *Transparent ultrasonic transducers based on relaxor ferroelectric crystals for advanced photoacoustic imaging*. 2023.
76. Xiang, Y., Zhang, R., and Cao, W., *Optimization of piezoelectric properties for [001]c poled 0.94Pb(Zn1/3Nb2/3)O3–0.06PbTiO3 single crystals.* Applied Physics Letters, 2010. **96**(9).

77. Deng, C., Ye, L., He, C., Xu, G., Zhai, Q., Luo, H., Liu, Y., and Bell, A.J., *Reporting Excellent Transverse Piezoelectric and Electro-Optic Effects in Transparent Rhombohedral PMN-PT Single Crystal by Engineered Domains.* Advanced Materials, 2021. **33**(43): p. 2103013.
78. Guo, P., Gao, W., Lin, R., Wang, X., Lan, J., Zhang, J., Wang, Y., Zhu, L., Zhang, Y., Li, F., et al., *Advancement in PMN-PT transparent piezoelectric ceramic for photoacoustic/ultrasound dual-mode imaging.* Journal of Materiomics, 2024: p. 100932.
79. Shi, M., Zhao, T., West, S.J., Desjardins, A.E., Vercauteren, T., and Xia, W., *Improving needle visibility in LED-based photoacoustic imaging using deep learning with semi-synthetic datasets.* Photoacoustics, 2022. **26**: p. 100351.
80. Zhang, J., Long, X., Zhang, G., Ma, Z., Li, W., Wang, Y., Yang, F., Lin, R., Li, C., and Lam, K.-H., *Broadband transparent ultrasound transducer with polymethyl methacrylate as matching layer for in vivo photoacoustic microscopy.* Photoacoustics, 2023. **33**: p. 100548.
81. Lam, K.H., Chen, Y., Cheung, K.F., and Dai, J.Y., *PMN–PT single crystal focusing transducer fabricated using a mechanical dimpling technique.* Ultrasonics, 2012. **52**(1): p. 20-24.
82. Moothanchery, M. and Pramanik, M., *Performance Characterization of a Switchable Acoustic Resolution and Optical Resolution Photoacoustic Microscopy System.* Sensors, 2017. **17**(2): p. 357.
83. Li, F., Lin, D., Chen, Z., Cheng, Z., Wang, J., Li, C., Xu, Z., Huang, Q., Liao, X., Chen, L.-Q., et al., *Ultrahigh piezoelectricity in ferroelectric ceramics by design.* Nature Materials, 2018. **17**(4): p. 349-354.
84. Gao, W., Wang, Y., Tian, X., Fu, D., Qi, Y., Guo, P., Qin, Y., Liu, J., and Zhang, Y., *Significantly enhanced piezoelectric properties in PMN-PT transparent ceramics by Sm/Pr co-doping.* Journal of Alloys and Compounds, 2025. **1010**: p. 177640.
85. Zhang, Z., Li, F., Chen, R., Zhang, T., Cao, X., Zhang, S., Shrout, T.R., Zheng, H., Shung, K.K., Humayun, M.S., et al., *High-Performance Ultrasound Needle Transducer Based on Modified PMN-PT Ceramic With Ultrahigh Clamped Dielectric Permittivity.* IEEE Transactions on Ultrasonics, Ferroelectrics, and Frequency Control, 2018. **65**(2): p. 223-230.
86. Weiyan, D., Chen, X., Zhang, Y., Li, X., Sun, F., Yang, Z., Tang, X., Zhou, C., Wang, F., and Zhao, X., *High Frequency Ultrasound Transducer Based on Sm-Doped Pb(Mg1/3Nb2/3)O3-0.28PbTiO3 Ceramic for Intravascular Ultrasound Imaging.* Ultrasonic Imaging, 2024. **46**(6): p. 312-319.
87. Zhang, J.-M., Bao, G.-C., Gao, W., Lin, R.-Q., Yang, F., and Lam, K.-H., *Miniature Ultrasound Transducer Incorporating Sm-PMN-PT 1-3 Composite.* Journal of Composites Science, 2024. **8**(3): p. 80.
88. Zhang, Z., Su, M., Li, F., Liu, R., Cai, R., Li, G., Jiang, Q., Zhong, H., Shrout, T.R., Zhang, S., et al., *New Sm-PMN-PT Ceramic-Based 2-D Array for Low-Intensity Ultrasound Therapy Application.* IEEE Transactions on Ultrasonics, Ferroelectrics, and Frequency Control, 2020. **67**(10): p. 2085-2094.
89. Bao, G.-C., Shi, D.-L., Zhang, J.-M., Yang, F., Yang, G., Li, K., Fang, B.-J., and Lam, K.-H., *Samarium-Doped Lead Magnesium Niobate-Lead Titanate Ceramics Fabricated by Sintering the Mixture of Two Different Crystalline Phases.* Materials, 2023. **16**(20): p. 6781.
90. Zhang, Q., Pang, X., Zhang, Z., Su, M., Hong, J., Zheng, H., Qiu, W., and Lam, K.H., *Miniature Transducer Using PNN-PZT-Based Ceramic for Intravascular Ultrasound.* IEEE Transactions on Ultrasonics, Ferroelectrics, and Frequency Control, 2019. **66**(6): p. 1102-1109.

91. Wu, D.W., Chen, R.M., Zhou, Q.F., Shung, K.K., Lin, D.M., and Chan, H.L.W., *Lead-free KNLNT piezoelectric ceramics for high-frequency ultrasonic transducer application.* Ultrasonics, 2009. **49**(3): p. 395-398.
92. Shung, K.K., Cannata, J.M., and Zhou, Q.F., *Piezoelectric materials for high frequency medical imaging applications: A review.* Journal of Electroceramics, 2007. **19**(1): p. 141-147.
93. Yan, X., Lam, K.H., Li, X., Chen, R., Ren, W., Ren, X., Zhou, Q., and Shung, K.K., *Correspondence: Lead-free intravascular ultrasound transducer using BZT-50BCT ceramics.* IEEE Transactions on Ultrasonics, Ferroelectrics, and Frequency Control, 2013. **60**(6): p. 1272-1276.
94. Cannata, J.M., Ritter, T.A., Wo-Hsing, C., Silverman, R.H., and Shung, K.K., *Design of efficient, broadband single-element (20-80 MHz) ultrasonic transducers for medical imaging applications.* IEEE Transactions on Ultrasonics, Ferroelectrics, and Frequency Control, 2003. **50**(11): p. 1548-1557.
95. Zhou, Q., Xu, X., Gottlieb, E.J., Sun, L., Cannata, J.M., Ameri, H., Humayun, M.S., Han, P., and Shung, K.K., *PMN-PT single crystal, high-frequency ultrasonic needle transducers for pulsed-wave Doppler application.* IEEE Transactions on Ultrasonics, Ferroelectrics, and Frequency Control, 2007. **54**(3): p. 668-675.
96. Hu, H., Fang, C., and Zou, J., *An optically-transparent PVDF transducer array for photoacoustic tomography*. SPIE BiOS. Vol. 11960. 2022: SPIE.
97. Ritter, T.A., Shrout, T.R., Tutwiler, R., and Shung, K.K., *A 30-MHz piezo-composite ultrasound array for medical imaging applications.* IEEE Transactions on Ultrasonics, Ferroelectrics, and Frequency Control, 2002. **49**(2): p. 217-230.
98. Wong, C.M., Chan, S.F., Liu, R., Zhang, J., Wu, W.C., Liang, Z., Yau, H.M., Wang, D.Y., Li, S., Lam, K.H., et al., *20-MHz phased array ultrasound transducer for in vivo ultrasound imaging of small animals.* Ultrasonics, 2022. **126**: p. 106821.
99. Winkler, A., Maslov, K., and Wang, L., *Noise-equivalent sensitivity of photoacoustics.* Journal of Biomedical Optics, 2013. **18**(9): p. 097003.
100. Sun, Y., Karaki, T., and Yamashita, Y., *Recent progress on AC poling of relaxor-PbTiO3 ferroelectric single crystals: a review.* Japanese Journal of Applied Physics, 2022. **61**(SB): p. SB0802.